Photonic and Phononic Band Gap Engineering for Circuit Quantum Electrodynamics and Quantum Transduction

Thesis by

Jash Haren Banker

In Partial Fulfillment of the Requirements for the
Degree of
Doctor of Philosophy

CALIFORNIA INSTITUTE OF TECHNOLOGY
Pasadena, California

2022
Defended October 20, 2021

Jash Haren Banker
ORCID: 0000-0002-2130-0825

ACKNOWLEDGEMENTS

It has been a long and bumpy road through grad school since I first arrived in Pasadena in 2015. I would not have made it this far had it not been for the help I received from others along the way.

To my advisor Oskar Painter, thank you for accepting me into your group when I was a third year Ph.D student looking for a new home. Your approach to research, the level of rigour you demand of all your students and your deep scientific insights have all been instrumental in shaping my scientific abilities.

None of the work in this thesis would have been possible without the support and help of the members of the Painter group to whom I owe many thanks. To Alp Sipahigil, who was a second advisor to me: Alp, you were a rare combination of amazing scientific aptitude coupled with a genuine desire to mentor young graduate students. You provided guidance and encouragement when I needed it most for which I will always be grateful. To Vinicius Ferreira, I am glad we worked together on the metamaterial project. The first half of this thesis would not have been possible without you. Thank you for making my transition to the Painter group smooth and for providing a friendly ear when I needed to vent my frustrations. I hope I have been able to do the same for you. To Andrew Keller, for teaching me all my nanofabrication skills that have served me so well over the years. Your patience and calm demeanor made you a great teacher. To Mohammad Mirhosseini, for guiding me through my first project and publication. I am glad I got to work with you and learn from you. To my office mates—the Transducers, the second half of this thesis would not have been possible without you. It's a shame COVID-19 robbed us of the opportunity to work together for a longer period of time. To Srujan Meesala and David Lake, I learned a lot about performing experiments in a careful and organized way from both of you and am grateful for your advice on everything from experiments to presentations and job applications. To Steven Wood, as someone who worked extensively in the cleanroom you understood the challenges involved in fab heavy projects and provided great advice (though your advice about fruit is suspect). To Piero Chiappina, I enjoyed our time working together on fab and on the transducer manuscript. I see a bright grad school career (and potential surfing career) ahead of you. To Michael Fang, you were instrumental in helping me make my decision to join the Painter group. It has been a pleasure working alongside you to keep our cleanroom running. To Hengjiang (Jared) Ren and Jie (Roger)

Luo, I enjoyed all our chats ranging from science to PubG. To Eunjong Kim and Xueyue (Sherry) Zhang, I was always inspired by your work ethic, your scientific skill, and your excellent presentations that taught me a lot. To Mahmoud Kalaee, Greg MacCabe, Clai Owens, and Mo Chen, we did not work together much but you were all always super helpful and ready to share your experience. To Sameer Sonar, Utku Hatipoglu, Andreas Butler, and Gihwan Kim, as young grad students you guys injected energy into the group. Your enthusiasm was infectious and I have enjoyed watching you learn and succeed and accomplish so much so fast. To Barry Baker - the Fabulous One, thank you for keeping the labs running like clockwork. You may now make graduation jokes. To the QPG staff, Kamal Yadav, Harry Liu, and Matt McCoy, having you looking after our labs has made doing research so much easier. Thank you for doing such a great job.

To Guy DeRose, Bert Mendoza, Matt Hunt, Nathan Lee, Alex Wertheim, Tiffany Kimoto, Jennifer Palmer, and all the other KNI staff present and past, thank you for keeping KNI running so smoothly. It has been a blessing to have access to such an advanced and well maintained nanofabrication facility.

To Christy Jenstad and Jennifer Blankenship, thank you for being the ‘work moms’ for all of us in the department. You provided a safe space for us whether we needed to scream or sob. The bowl of candy always helped.

To all the friends I made along the way, thank you for the memories and experiences you have given me. You have enriched my life far beyond any science I learned in the lab. A special thank you to the Yangji crew. To Michelle Cua, for providing me with unwavering support and ice wine. To Pai Buabthong, for being one of the calmest people I know. Pai, hanging out with you was as relaxing as meditation. To Joeson Wong for everything from help on problem sets to driving me around in your Prius to my first In-n-Out burger (double-double animal style is undoubtedly the way to go). To Peishi Cheng for our discussions on politics and for reminding me that it’s ok to care about things outside of the lab. To Samuel Loke for gumbo, spaghetti bolognese, summer barbeques and game nights. To Claire Taijung Kuo for the pineapple cakes. To Kai Matsuka, I wish I had gotten to know you earlier. I blame Michelle. To Angeliki Laskari for being a kindred soul who shared my taste for 80s music and my obsession with the Boss. On days when I wanted to hide on the backstreets, the music we shared lifted my spirits and made me dance - even if I was just dancing in the dark.

To Jeannette, you may be right, I may be slightly crazy, but without you I would have gone completely insane. Thank you for always being there for me and dealing with my moods and my ups and downs. I look forward to our new beginning in Munich.

Last but not least, to my parents who have been with me on this journey not just for 6 years, but for the last 28 years. No amount of words can express my gratitude for all you have done, so I just have two: thank you.

ABSTRACT

The ability to pattern materials at the wavelength and sub-wavelength scale has led to the concept of photonic crystals and metamaterials - artificially engineered structures that exhibit electromagnetic properties not found in conventional materials. Such engineered structures offer the ability to slow down and even inhibit the propagation of electromagnetic waves giving rise to a photonic band gap and a sharply varying photonic density of states.

Quantum emitters in the presence of an electromagnetic reservoir with varying density of states can undergo a rich set of dynamical behavior. In particular, the reservoir can be tailored to have a memory of past interactions with emitters, in contrast to memory-less Markovian dynamics of typical open systems. In part 1 of this thesis, we investigate the non-Markovian dynamics of a superconducting qubit strongly coupled to a superconducting metamaterial waveguide engineered to have both a sharp spectral variation in its transmission properties and a slowing of light by a factor of 650. Tuning the qubit into the spectral vicinity of the passband of this slow-light waveguide reservoir, we observe a 400-fold change in the emission rate of the qubit, along with oscillatory energy relaxation of the qubit resulting from the beating of bound and radiative dressed qubit-photon states. Further, upon addition of a reflective boundary to one end of the waveguide, we observe revivals in the qubit population on a timescale 30 times longer than the inverse of the qubit's emission rate, corresponding to the round-trip travel time of an emitted photon. With this superconducting circuit platform, future studies of multi-qubit interactions via highly structured reservoirs and the generation of multi-photon highly entangled states are possible.

While microwave frequency superconducting circuits are near ideal testbeds for quantum electrodynamics experiments of the type discussed in part 1, microwave photons are not well suited for transmission of quantum information over long distances due to the presence of a large thermal background at room temperature. Optical photons are ideal for quantum communication applications due to their low propagation loss at room temperature. Coherent transduction of single photons from the microwave to the optical domain has the potential to play a key role in quantum networking and distributed quantum computing. In part 2 of this thesis, we extend the notion of band gap engineering to the optical and acoustic domain and present the design of a piezo-optomechanical quantum transducer where transduction is mediated by a strongly hybridized acoustic mode of a lithium niobate piezoacoustic cavity attached to a silicon optomechanical crystal patterned on a silicon-on-insulator substrate. We estimate an intrinsic transduction efficiency of 29% with <0.5 added noise quanta when our transducer is resonantly coupled to a superconducting transmon qubit and operated in pulsed mode. Our design involves on-chip integration of a superconducting qubit with the piezo-optomechanical transducer. Absorption of stray photons from the optical pump used in the transduction process is known to cause excess decoherence and noise in the superconducting circuit. The recovery time of the superconducting circuit after the optical pulse sets a limit on the transducer repetition rate. We fabricate niobium based superconducting circuits on a silicon substrate and test their response to illumination by a 1550 nm laser. We find a recovery time of $\sim 10\ \mu$s, indicating that a repetition rate of 10 kHz should be possible. Combined with the expected efficiency and noise metrics of our design, we expect that a transducer in this parameter regime would be suitable to realize probabilistic schemes for remote entanglement of superconducting quantum processors. We conclude by discussing some of the challenges associated with fabricating niobium superconducting qubits and lithium niobate piezoacoustic devices on silicon-on-insulator substrates and provide initial steps towards realizing our transducer design in the lab.

PUBLISHED CONTENT AND CONTRIBUTIONS

[1] V. S. Ferreira*, J. Banker*, A. Sipahigil, M. H. Matheny, A. J. Keller, E. Kim, M. Mirhosseini, and O. Painter. "Collapse and revival of an artificial atom coupled to a structured photonic reservoir". In: *Phys. Rev. X* 11.4 (2021), p. 041043. DOI: `10.1103/PhysRevX.11.041043`.
J.B. participated in the conception of the project, design and fabrication of the device, and performance of the measurements.

[2] E. Kim, X. Zhang, V. S. Ferreira, J. Banker, J. K. Iverson, A. Sipahigil, M. Bello, A. González-Tudela, M. Mirhosseini, and O. Painter. "Quantum electrodynamics in a topological waveguide". In: *Physical Review X* 11 (1 2021), p. 011015. DOI: `10.1103/PhysRevX.11.011015`.
J.B. contributed to the design of the metamaterial waveguide.

[3] M. Mirhosseini, A. Sipahigil, M. Kalaee, and O. Painter. "Superconducting qubit to optical photon transduction". In: *Nature* 588.7839 (2020), pp. 599–603. DOI: `10.1038/s41586-020-3038-6`.
Extended Data Figure 7 reprinted in this thesis, by permission from Springer Customer Service Centre GmbH, ©2020.

[4] P. Krantz, M. Kjaergaard, F. Yan, T. P. Orlando, S. Gustavsson, and W. D. Oliver. "A quantum engineer's guide to superconducting qubits". In: *Applied Physics Reviews* 6.2 (2019), p. 021318. DOI: `10.1063/1.5089550`.
Figure 1 reprinted and referenced in this thesis, with the permission of AIP publishing.

[5] A. J. Keller, P. B. Dieterle, M. Fang, B. Berger, J. M. Fink, and O. Painter. "Al transmon qubits on silicon-on-insulator for quantum device integration". In: *Applied Physics Letters* 111.4 (2017), p. 042603. DOI: `10.1063/1.4994661`.
Figure 1a. reprinted and referenced in this thesis, with the permission of AIP publishing.

[6] J. Chan, A. H. Safavi-Naeini, J. T. Hill, S. Meenehan, and O. Painter. "Optimized optomechanical crystal cavity with acoustic radiation shield". In: *Applied Physics Letters* 101.8 (2012), p. 081115. DOI: `10.1063/1.4747726`.
Figure 2 adapted and referenced in this thesis, with the permission of AIP publishing.

TABLE OF CONTENTS

LIST OF ILLUSTRATIONS

LIST OF TABLES

INTRODUCTION

The propagation of electromagnetic waves through a macroscopic medium is governed by Maxwell's equations which in the absence of free charges or currents can be written as:

$$\begin{aligned}
\nabla \cdot \epsilon \mathbf{E} &= 0 \\
\nabla \times \mathbf{E} &= -\frac{\partial}{\partial t}\mu \mathbf{H} \\
\nabla \cdot \mu \mathbf{H} &= 0 \\
\nabla \times \mathbf{H} &= \frac{\partial}{\partial t}\epsilon \mathbf{E}
\end{aligned} \tag{1}$$

where ϵ is the permittivity and μ is the permeability. If the wavelength of the electromagnetic wave is much larger than the atoms of the media, the microscopic details of the medium are averaged out and the medium is characterized by the two macroscopic parameters ϵ and μ. Periodically patterning the medium at the deep sub-wavelength scale can alter the effective ϵ and μ of the material allowing us to engineer 'meta-materials' which can have novel electromagnetic responses not found in 'conventional' materials such as a negative refractive index, chirality and the existence of photonic bandgaps.

A related concept is that of photonic crystals. In the theory of solid state physics, crystals are periodic arrangements of atoms in a lattice which give rise to a periodic potential experienced by the electrons. This periodic potential gives rise to an electronic band structure which in certain cases can have a band gap (such as in a semiconductor). In a similar manner, photonic crystals are periodic structures patterned at the wavelength scale giving rise to a periodically modulated permittivity $\epsilon(\mathbf{r}) = \epsilon(\mathbf{r} + \mathbf{R})$. By substituting this periodically modulated permittivity into Maxwell's equations, one can solve for a photonic band structure in analogy to the electronic band structure [1]. Crucially, it is possible to engineer the band structure to create a photonic band gap where photons of a certain frequency cannot propagate. This same idea can be extended to the acoustic domain where periodic patterning at the wavelength scale gives rise to a periodic modulation of the elastic modulus and the mass density leading to an acoustic band structure which can host acoustic band gaps.

In this thesis, we explore two applications of this idea of band structure engineering which represent two distinct projects I pursued during my time in the Painter group.

As such, the thesis is divided into two fairly independent parts united by the common theme of using wavelength and sub-wavelength scale periodically patterned structures to engineer photonic and phononic bandgaps.

In Part 1 of this thesis, we develop a superconducting, microwave frequency metamaterial platform for ‘non-Markovian’ circuit Quantum Electrodynamics (cQED) experiments. A canonical example of a ‘Markovian’ process is the spontaneous emission of an atom coupled to the fluctuating electromagnetic vacuum [2]. In this process, information in the form of energy flows from the atom into the electromagnetic reservoir. However, by carefully engineering the electromagnetic reservoir, it is possible to introduce ‘non-Markovian’ memory effects where there is information back-flow from the reservoir into the atom [3–6]. By utilizing a capacitively coupled array of identical superconducting LC resonators with a deep sub-wavelength lattice constant, we develop a one-dimensional (1D) finite bandwidth slow-light waveguide that exhibits sharp band edges and a flat, nearly ripple-free passband where the group velocity of microwave photons is reduced by a factor of ~ 650. This 1D slow-light waveguide forms a 1D electromagnetic reservoir to which we couple a superconducting qubit that acts as an ‘artificial’ atom. By performing spectroscopic field measurements as well as time dependent measurements of qubit dynamics, we demonstrate that our qubit-metamaterial waveguide platform is deep in the non-Markovian regime. Further, by utilizing the slow-light nature of our waveguide, we demonstrate time-delayed feedback of microwave photons emitted by the qubit. This time-delayed feedback can be used to generate two-dimensional photonic cluster states which have been proposed as a universal resource for measurement based quantum computing [7]. Our measurements allow us to estimate the attainable fidelity and scale of photonic cluster states that can be generated using this metamaterial platform.

All of the experiments described in Part 1 use a superconducting circuit platform. The high degree of control offered by superconducting circuits to engineer qubit-waveguide couplings, tune qubit frequencies in-situ and perform single qubit operations at timescales much faster than the coherence time of the qubit make this a powerful test bed for performing quantum optics experiments. More broadly, these same features make superconducting qubits very promising for quantum computing. Recent landmark demonstrations have established superconducting quantum circuits as a leading platform for quantum computing and simulation [8]. However, the superconducting circuit platform has some drawbacks too. Superconducting circuits encode quantum information in microwave-frequency photons (f ~5GHz). To keep these circuits in the quantum ground state, they must be cooled to millikelvin (mK) temperatures ($k_b T \ll hf$). Further, microwave photons suffer from propagation losses as high as 1dB/m [9]. The large thermal background at room temperature and high propagation loss of microwave photons makes transmitting quantum information between remote superconducting processors a challenging task. In contrast, optical photons (f~200THz) have a negligible thermal background at room temperature. Optical fibers exhibit propagation losses as low as 0.2dB/km [9]. As a result, optical photons are naturally suited for low loss, long distance transmission of quantum information. The complementary properties of these two systems have spurred interest in transducers that can coherently convert quantum information between microwave and optical frequencies. Such transducers would enable optically connected networks of remote superconducting quantum processors analogous to classical networks underlying the internet and large-scale supercomputers with optical interconnects.

In Part 2, we present the design of a wavelength scale piezo-optomechanical quantum transducer device optimized for high conversion efficiency and low added noise. In our scheme, transduction between the microwave and optical frequency photons is mediated by an intermediate mechanical mode which couples to microwave photons via the piezoelectric effect and to optical photons via a parametric optomechanical interaction. It is crucial that the optical and mechanical mode involved in the transduction process have high coherence. Here we utilize the idea of photonic and phononic (optomechanical) crystals to engineer optical and acoustic bandgaps. By introducing carefully engineered defects that interrupt the periodicity of our photonic/phononic crystals, we can create highly localized optical and acoustic modes that are well isolated from the environment due to the presence of bandgaps and also exhibit strong optomechanical and piezoelectric couplings. Our design is based on a lithium niobate on silicon-on-insulator platform. We theoretically analyze the expected efficiency and noise metrics of our transducer design. We also discuss limitations to the repetition rate of our transducer device arising from optically generated quasiparticles in the superconducting qubit during operation of the transducer. Previous work from our group using a similar piezo-optomechanical transducer with aluminum superconducting qubits was limited to a repetition rate of ~ 100 Hz due to the relatively long quasiparticle lifetime in aluminum (~ ms) [10]. A superconductor with shorter quasiparticle lifetime is niobium [11, 12]. We experimentally investigate the optical response of niobium based superconducting qubits and find a qubit recovery time on the order of $\sim 10\,\mu$s after optical illumination. Our results suggest that switching from aluminum to niobium based superconducting qubits could allow a 100-fold increase in the repetition rate over previous work [10]. In the last two chapters of Part 2, we discuss some practical fabrication related challenges associated with developing niobium qubits on silicon-on-insulator and also lithium niobate piezo-mechanical devices on silicon-on-insulator—both of which are necessary for realization of our quantum transducer design. We provide initial steps towards addressing these fabrication challenges that may hopefully benefit future generations of graduate students in bringing our transducer design to life in the lab.

PART 1: SUPERCONDUCTING METAMATERIALS FOR CIRCUIT QUANTUM ELECTRODYNAMICS IN THE NON-MARKOVIAN REGIME

In Part I of this thesis, we are interested in studying non-Markovian dynamics of an atom strongly coupled to a highly structured one-dimensional electromagnetic reservoir. Instead of working with actual atoms, we will use a superconducting circuit platform where superconducting qubits will behave as 'artificial atoms'. The basics of the superconducting qubit platform will be introduced in Chapter 1. Since superconducting circuits are designed and fabricated on chip, they can be engineered to a very high degree offering precise control over the circuit parameters. In particular, we can pattern these circuits at the deep sub-wavelength scale allowing us to realize microwave frequency metamaterials that can give rise to novel photonic bandstructures. In Chapter 2, we will develop a superconducting metamaterial platform that allows us to realize a one-dimensional finite bandwidth waveguide where the group velocity of propagating microwave fields is drastically reduced. This metamaterial waveguide will serve as our one dimensional electromagnetic reservoir. We will then show experimental results demonstrating non-Markovian dynamics of a superconducting qubit strongly coupled to this 'slow-light metamaterial waveguide'. A potential application of our metamaterial platform for generating two dimensional cluster states of microwave photons will be discussed in Chapter 3. Further details about the design, fabrication, and theoretical modelling of our system will be presented in the Appendix at the end of Part 1 (Chapter 4).

Chapter 1

BACKGROUND: SUPERCONDUCTING QUBITS

This chapter will be a brief introduction to superconducting qubits. It will cover the essential concepts needed to follow the rest of this thesis. For a more extensive review, please see [13–15].

1.1 Superconducting Qubit Basics

Just like a classical bit encodes information in the form of a 0 or 1, a quantum bit (qubit) encodes quantum information using two levels which we call the ground ($|g\rangle$ or $|0\rangle$) and excited ($|e\rangle$ or $|1\rangle$) states. A superconducting qubit can be thought of as a two level system formed using superconducting electrical circuits. Since these circuits are designed and fabricated on a chip, they offer a large degree of control over their circuit parameters. One of the simplest electrical circuits we can conceive of is an LC oscillator (Fig. 1.1a). The Hamiltonian describing this circuit is

$$H = \frac{Q^2}{2C} + \frac{\phi^2}{2L} \tag{1.1}$$

where Q is the charge, ϕ is the flux, C is the capacitance, and L is the inductance. Quantum mechanically, we can promote the charge and flux variables to quantum operators, and this Hamiltonian can be shown to reduce to that of a quantum harmonic oscillator (QHO),

$$\hat{H} = \hbar\omega(a^\dagger a + \frac{1}{2}) \tag{1.2}$$

This Hamiltonian has a number of equally spaced energy levels which are $\omega = \frac{1}{\sqrt{LC}}$ apart (Fig. 1.1b). In order to have an effective two level system to serve as our qubit, we need to isolate two of the energy levels. This can be achieved by replacing the linear inductor of the LC oscillator by a non-linear element like a Josephson junction (Fig. 1.1c). A Josephson junction is a pair of superconductors separated by a thin insulating layer. The voltage and current are determined by the Josephson relations:

$$\begin{aligned} V &= \frac{\hbar}{2e}\frac{d\phi}{dt} \\ I &= I_c \sin(\phi) \end{aligned} \tag{1.3}$$

The energy stored in the Josephson junction can then be written as

$$\begin{aligned} E_L &= \int V I dt \\ &= -\frac{\hbar I_c}{2e}\cos(\phi) \\ &= -E_J \cos(\phi) \end{aligned} \tag{1.4}$$

We can now write the Hamiltonian of this non-linear LC oscillator as

$$\begin{aligned} H &= \frac{\hat{Q}^2}{2C} - E_J \cos(\hat{\phi}) \\ &= \frac{\hat{Q}^2}{2C} - E_J \left(1 - \frac{\hat{\phi}^2}{2} + \frac{\hat{\phi}^4}{24} + \ldots\right) \end{aligned} \tag{1.5}$$

As can be seen from the Taylor expansion in the second line of Eq.1.5, our non-linear oscillator now has higher order terms in addition to the quadratic term—this introduces anharmonicity into our system, and we get multiple energy levels *which are no longer equally spaced* as can be seen in Fig. 1.1d. Now if we operate this circuit at frequencies close to the $|0\rangle \rightarrow |1\rangle$ transition frequency then all the higher transitions are detuned and can be ignored. Thus by replacing the linear inductor with a non-linear Josephson junction, we have reduced our LC circuit to an effective two-level system that acts as our quantum bit. For the bulk of this thesis, we will ignore the higher energy levels and treat our superconducting qubit as having only two states. However it is important to remember that these higher levels exist, and we will on occasion make use of them (particularly in Chapter 2 when we discuss a protocol for generating cluster states).

The particular type of superconducting qubit used in this thesis is the transmon qubit [16]. The transmon qubit is characterized by a large $\frac{E_J}{E_C}$ ratio (~ 100), where $E_C = \frac{e^2}{2C}$ is the charging energy and E_J is the Josephson energy defined in Eq. 1.4. The large $\frac{E_J}{E_C}$ ratio makes the transmon less susceptible to charge noise. For a transmon qubit, the $|g\rangle \rightarrow |e\rangle$ transition frequency is given by $\omega_q = (\sqrt{8E_J E_C} - E_C)/\hbar$ while the anharmonicity is given by $\alpha = -E_C/\hbar$. The sensitivity of the qubit to charge noise drops exponentially as a function of $\frac{E_J}{E_C}$ while the anharmonicity drops linearly in E_C. As a result, by operating at large $\frac{E_J}{E_C}$ the transmon qubit can be made insensitive to charge noise without compromising too much on the anharmonicity.

1.2 Qubit Frequency Tuning

To make our qubit frequency tunable, we replace the single junction shown in the circuit of Fig. 1.1c. with a pair of junctions that form a superconducting loop

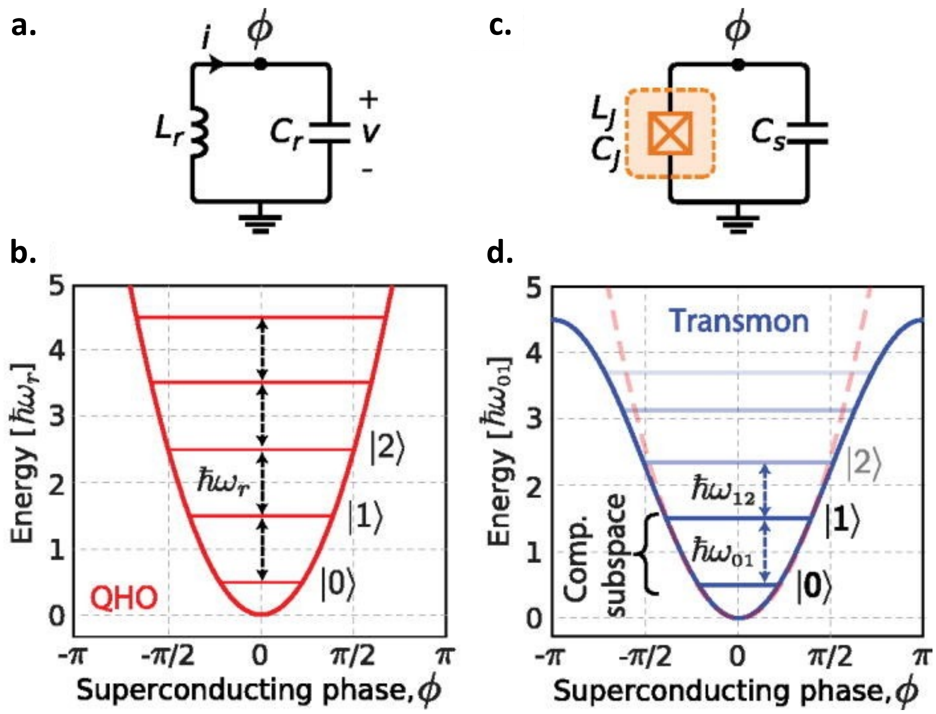

Figure 1.1: **Circuit model and energy diagram of a quantum harmonic and anharmonic oscillator. a.** Circuit for a parallel LC-oscillator (quantum harmonic oscillator, QHO), with inductance L_r in parallel with capacitance, C_r. **b.** Energy potential for the QHO, where energy levels are equidistantly spaced $\hbar\omega_r$ apart. **c.** Circuit for a superconducting qubit, with the non-linear Josephson junction (L_J, C_J) in parallel with capacitance C_s. **d.** Energy potential for the qubit, where energy levels are no longer equidistantly spaced allowing us to isolate the two lowest levels $|0\rangle$ and $|1\rangle$ that form the computation subspace. Figure reproduced from Ref. [15]

called a SQUID loop (Superconducting Quantum Interference Device). The pair of junctions acts as a single junction with an effective critical current that depends on the external flux threading the squid loop as $I_{c,eff} = 2I_c \cos\left(\pi\frac{\phi_{ext}}{\phi_0}\right)$ where $\phi_0 = \frac{h}{2e}$ is the magnetic flux quantum. Since the Josephson energy and hence the qubit frequency depends on the critical current, we can tune the frequency of our qubit by changing the flux threading the SQUID loop. This can be done using an on-chip 'Z-line' (also called 'flux-bias line') or an off chip superconducting coil. In the Z-line approach, an on-chip coplanar waveguide is shorted to ground in close vicinity to the SQUID loop as shown in Fig. 1.2b. The inductive coupling between this bias line and the SQUID loop allows us to change the flux threading the SQUID loop (and hence the qubit frequency) by applying DC currents on the Z-line. Since this line is a microwave line, it is also possible to rapidly change/modulate the qubit frequency by applying time varying currents to this line.

1.3 Qubit State Preparation

To excite the qubit and prepare it in various superposition states, we use an on-chip 'XY line' that takes the form a microwave coplanar waveguide which is routed close to the qubit capacitor and is terminated in an open circuit near the qubit capacitor as shown in Fig. 1.2b. The capacitive coupling between the open end of the XY line and the qubit capacitor allows us to drive the qubit using microwave pulses that are resonant with the qubit frequency. By adjusting the length, amplitude, and phase of the microwave pulse, one can prepare the qubit in any superposition of the $|g\rangle$ and $|e\rangle$ states. Typical pulse times are on the $\sim$10 ns timescale.

1.4 Qubit Readout

To readout the state of the qubit, we use a standard technique called dispersive readout. In this technique, the qubit is coupled to a microwave frequency readout resonator. The joint qubit-resonator system can be described by the Jaynes-Cummings Hamiltonian,

$$\hat{H} = \hbar\omega_r \hat{a}^\dagger \hat{a} - \hbar\omega_q \frac{\hat{\sigma_z}}{2} + \hbar g \left(\hat{a}\hat{\sigma_+} + \hat{a}^\dagger \hat{\sigma_-} \right) \tag{1.6}$$

The first term in Eq. 1.6 represents the readout resonator (RR) with frequency ω_r, the second term represents the qubit as a two-level system with frequency ω_q, and the last term represents a qubit-RR interaction with a coupling strength 'g'. We design the readout resonator to be detuned from the qubit at a detuning $\omega_q - \omega_c = \Delta$. In the dispersive limit given by $|g| < |\Delta|$, we can approximate the Hamiltonian of Eq. 1.6 as

$$\begin{aligned} \hat{H} &= \hbar\omega_r \hat{a}^\dagger \hat{a} - \hbar\omega_q \frac{\hat{\sigma_z}}{2} - \hbar \frac{g^2}{\Delta} \hat{\sigma_z} \hat{a}^\dagger \hat{a} \\ &= \hbar \left(\omega_r - \frac{g^2}{\Delta} \hat{\sigma_z} \right) \hat{a}^\dagger \hat{a} - \hbar\omega_q \frac{\hat{\sigma_z}}{2} \end{aligned} \tag{1.7}$$

It is clear from the second line of Eq. 1.7 that the readout resonator acquires a qubit state dependent frequency shift. We define the dispersive shift $\chi = \frac{2g^2}{\Delta}$ as the difference in the two readout resonator frequencies (corresponding to the two qubit states $\sigma_z = \pm 1$). In practice, since the qubit has higher levels which contribute to the dispersive shift, this formula is modified as

$$\chi = \frac{2g^2}{\Delta \left(1 + \frac{\Delta}{\alpha} \right)} \tag{1.8}$$

where α is the anharmonicity of the qubit. To perform qubit readout, we simply interrogate the readout resonator and its frequency allows us to infer the state of the qubit.

Physically, we implement our readout resonator as either a transmission line resonator as shown in Fig. 1.2a. or a lumped element resonator. The readout resonator is capacitively coupled to the qubit with some coupling capacitance C_g. A circuit model for a readout resonator capcitively coupled to a qubit is shown in Fig. 1.3. In this model, we can treat the qubit as simple LC oscillator. For a given set of designed circuit parameters, the coupling strength 'g' (and hence the dispersive shift) can be calculated as

$$g = \frac{1}{2}\frac{C_g}{(C_q + C_g)(C_r + C_g)}\sqrt{\omega_r \omega_q} \tag{1.9}$$

The readout resonator is also capacitively coupled to an on-chip coplanar waveguide that allows us to interrogate the frequency of the readout resonator and infer the state of the qubit. We call this coplanar waveguide the 'readout line' and it is shown in Fig. 1.2a.

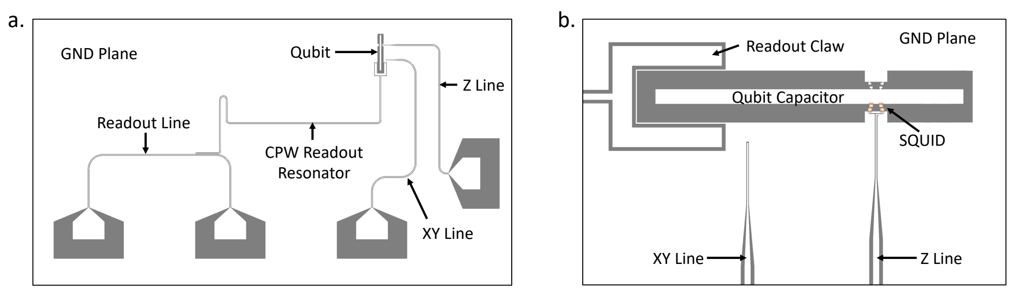

Figure 1.2: **Example layout of a superconducting qubit chip. a.** Sample qubit chip layout indicating the qubit, CPW readout resonator, qubit control lines, and readout line. **b.** Zoom into qubit region showing the qubit capacitor, SQUID loop, XY line, Z line, and the readout claw for coupling the qubit to the readout resonator.

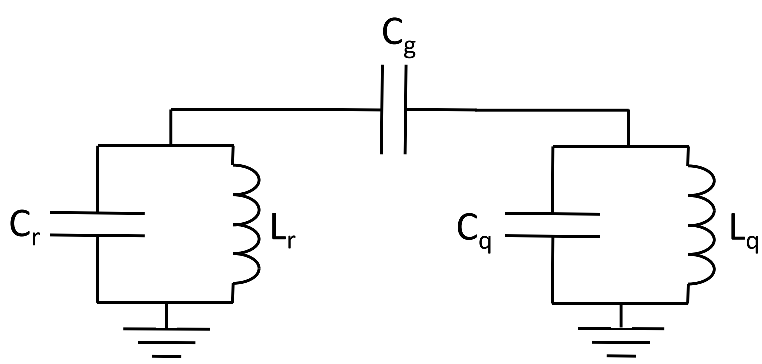

Figure 1.3: **Capacitively coupled LC oscillator model of qubit coupled to readout resonator.**

1.5 Qubit Characterization

Now that we have covered the basic concepts related to the design and control of superconducting qubits, we will briefly review some basic single qubit measurements that will be used frequently throughout this thesis. Since superconducting qubits operate in the $f_q \sim$ GHz frequency range, they need to be cooled down to cryogenic temperatures $T << hf_q$. All the measurements in this thesis were carried out at the base temperature ($\sim$ 10 mK) of a dilution refrigerator. Typical qubit characterization proceeds as follows:

Continuous Wave (CW) Measurements

We begin our measurements by applying continuous wave (CW) signals to the readout and XY lines. The goal of these initial measurements is to quickly determine the frequencies of the readout resonator and superconducting qubit.

<u>Locate the Readout Resonator</u>

The first step is locating the readout resonator. We use a Vector Network Analyzer (VNA) to measure the readout resonator in transmission (S_{21}) or reflection (S_{11}). We show an example of a reflection measurement (S_{11}) of a lumped element readout resonator in Fig. 1.4a. The dip in the reflection spectrum gives us the frequency of the readout resonator.

<u>Locate the Qubit</u>

Next we apply a continuous wave (CW) microwave signal on the XY line at frequencies near the expected qubit frequency. As we sweep the frequency of the XY tone, we continue using the VNA to monitor the readout resonator frequency. When the XY tone is resonant with the qubit frequency, it drives the qubit which causes a dispersive shift in the readout resonator frequency and shows up as a change in the VNA spectrum as shown in Fig. 1.4b. We can repeat this measurement as we apply a DC current on the flux line until we have our qubit tuned to the desired frequency.

Pulsed Measurements

In the continuous wave measurements described above, we are constantly driving the qubit into a mixed state. To get greater control over the qubit state, we employ pulsed XY drive signals that allow us to prepare the qubit in any superposition of $|g\rangle$ and $|e\rangle$. An arbitrary waveform generator (AWG) is used to synthesize finite

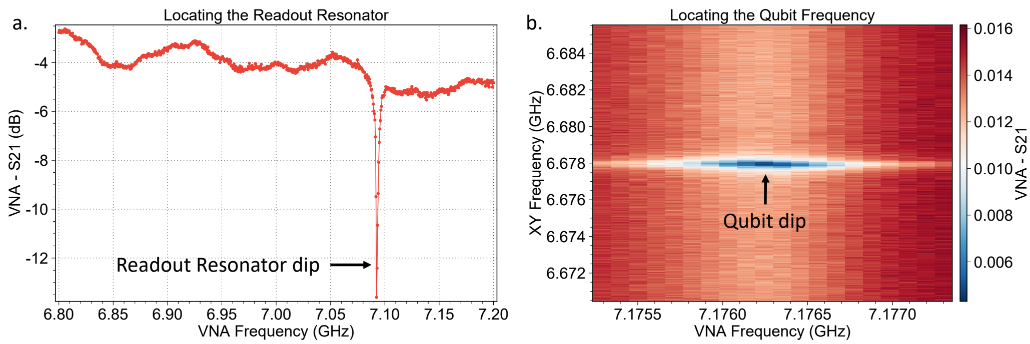

Figure 1.4: **Example CW spectroscopy data. a.** Example dataset from a broad VNA sweep to loacate the readout resonator. The resonator shows up as a dip in the VNA measurement **b.** Example dataset from a two-tone spectroscopy measurement to locate the qubit frequency.

length pulses at an intermediate frequency (IF) of $\sim$ 100 MHz. This IF signal is then upconverted to RF frequencies using an IQ mixer. The upconverted RF signal is used to excite the qubit via the XY line. To perform readout, a similarly upconverted RF signal is used to interrogate the readout resonator and the reflected or transmitted signal from the readout resonator is downconverted to IF frequencies and then demodulated to DC using a digitizer. This technique allows us to measure both the phase and the amplitude of the readout signal.

Rabi Measurement

We now proceed to calibrate the pulse lengths needed to prepare the qubit in various states. The pulse sequence and a sample dataset for this measurement is shown in Fig. 1.5a. where we apply a XY pulse of a variable duration to the qubit followed by readout. As we sweep the duration of the XY pulse for a fixed pulse amplitude, we see Rabi oscillations of the qubit. The maxima of the Rabi curve gives us the duration (t_π) of the XY pulse required to put the qubit in the $|e\rangle$ state. A pulse of half the duration ($t_{\pi/2}$) can be used to create an equal superposition of $|g\rangle$ and $|e\rangle$.

T_1 Measurement

Once we have identified the π-pulse duration for a given pulse amplitude, we proceed to characterize the lifetime (T_1) of the qubit. This is the rate at which a qubit in state $|e\rangle$ relaxes back to state $|g\rangle$. A T_1 measurement involves applying a π pulse to prepare the qubit in state $|e\rangle$, and then waiting for some variable time delay τ before reading out the state of the qubit. We repeat this measurement multiple times as we sweep the time delay τ and measure the probability of finding the qubit in the state

$|e\rangle$ as a function of τ. The T_1 pulse sequence and an example T_1 dataset is shown in Fig. 1.5b. We can fit the data to an exponential decay of the form $P_e = e^{-\tau/T_1}$ to extract the qubit lifetime T_1.

T_2^* Measurement

Apart from the lifetime, another important metric for a qubit is its decoherence time (T_2^*). This is the time for which a qubit is able to stay phase-coherent. A T_2^* measurement begins by applying a $\frac{\pi}{2}$ pulse to the qubit. After a variable time delay τ, we apply another $\frac{\pi}{2}$ pulse and readout the state of the qubit. In the absence of decoherence, the two $\frac{\pi}{2}$ pulses separated by a time τ should behave as π pulse and put the qubit in state $|e\rangle$. However, if the qubit experiences decoherence in the time delay τ between the two $\frac{\pi}{2}$ pulses, then the final qubit state may be rotated away from $|e\rangle$. Sweeping the time delay τ allows us to extract the decoherence rate of the qubit. The pulse sequence employed for this measurement is called a Ramsey pulse sequence and is shown in the inset of Fig. 1.5c. along with a sample dataset. To allow for greater fitting accuracy, in practice this measurement is performed at a small detuning (δ) from the qubit frequency giving rise to the Ramsey fringes seen in the data. We fit the data to $P_e = e^{-\tau/T_2^*} \cos{(\delta\tau + \phi)}$ and extract the qubit decoherence time T_2^*.

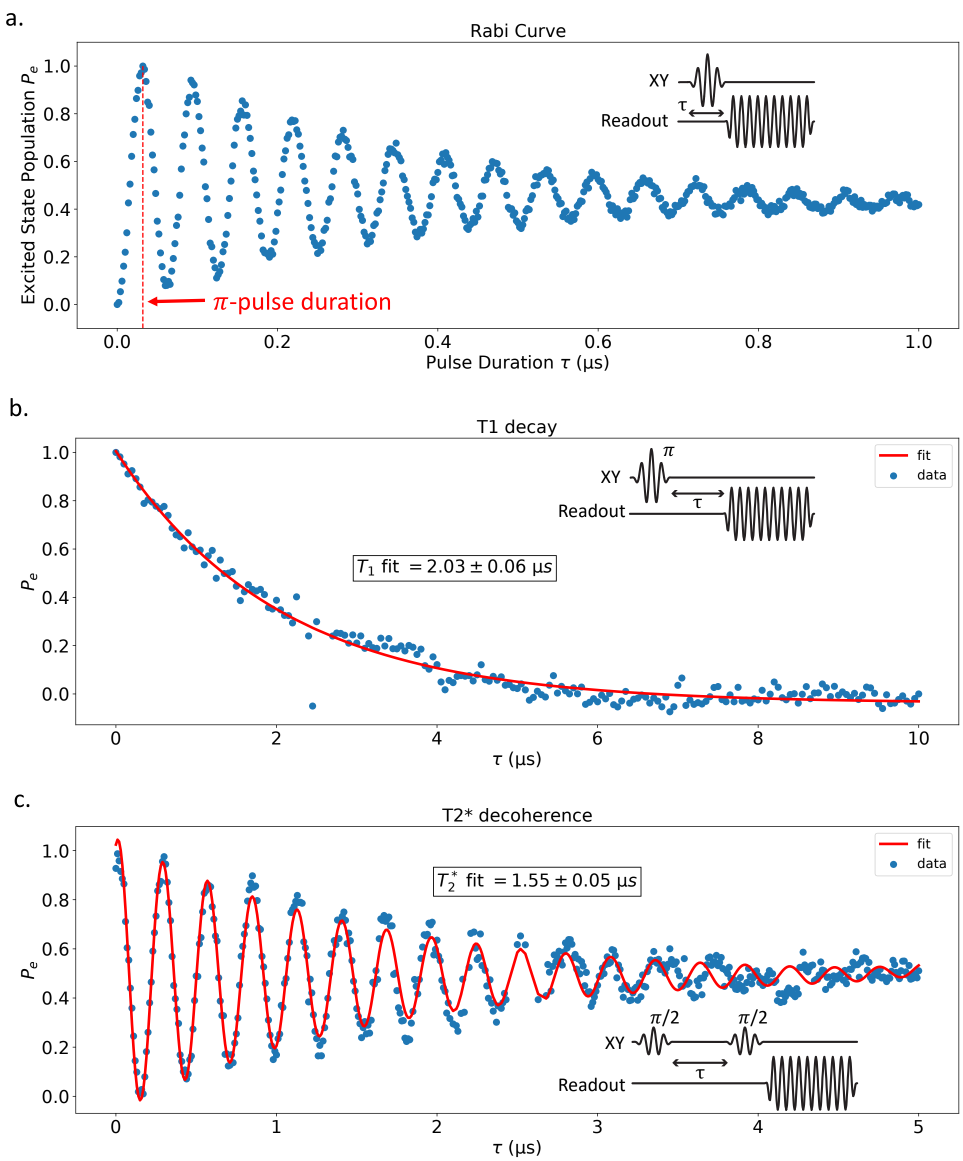

Figure 1.5: **Standard pulsed measurements of superconducting qubits. a.** Rabi pulse sequence (inset) and example Rabi dataset indicating the π-pulse duration **b.** T_1 pulse sequence (inset) and example T_1 dataset **c.** T_2^* pulse sequence (inset) and example T_2^* dataset.

Chapter 2

COLLAPSE AND REVIVAL OF AN ARTIFICIAL ATOM COUPLED TO A STRUCTURED PHOTONIC RESERVOIR

[1] V. S. Ferreira*, J. Banker*, A. Sipahigil, M. H. Matheny, A. J. Keller, E. Kim, M. Mirhosseini, and O. Painter. "Collapse and revival of an artificial atom coupled to a structured photonic reservoir". In: *Phys. Rev. X* 11.4 (2021), p. 041043. DOI: 10.1103/PhysRevX.11.041043.

2.1 Introduction

Spontaneous emission by a quantum emitter into the fluctuating electromagnetic vacuum, and the corresponding exponential decay of the emitter excited state, is an emblematic example of Markovian dynamics of an open quantum system [2]. However, modification of the electromagnetic reservoir can drastically alter this dynamic, introducing "non-Markovian" memory effects to the emission process, a consequence of information back-flow from the reservoir to the emitter [3–6]. A canonical example of this, considered in early theoretical work [17–19], is the behavior of a quantum emitter whose natural emission frequency lies close to the gap edge of a photonic bandgap material [20, 21] where a sharp transition of the photonic density of states (DOS) occurs. Inside the bandgap the emitter sees a reservoir devoid of electromagnetic states, while just outside of the bandgap lies a continuum of states. This structure of the photonic bandgap reservoir leads to a strong dressing of the emitter, and a resulting emission dynamics modified by the interplay between bound and radiative emitter-photon resonant states [22–26].

More recently, theoretical studies have explored how a structured reservoir with non-Markovian memory alters the entanglement within a quantum system coupled to such a reservoir [27–29]. This has led to the paradigm of reservoir engineering, where non-Markovianity is a quantifiable resource for quantum information processing and communication. Theory work from this quantum information perspective has shown that long-lived reservoir correlations can be used for the generation and preservation of entanglement [30, 31] and quantum control [32] of a quantum system, enhancement of the capacity of quantum channels [33], and the synthesis of exotic many-body quantum states of light from single emitters [7].

In practice, observation of non-Markovian emission phenomena can be achieved by strongly coupling an emitter to a single-mode waveguide—a one-dimensional (1D) reservoir with a continuum of states. Waveguides which break continuous translational symmetry, or which host resonant elements within the waveguide, are of particular interest in this regard owing to the structure in their spectrum [34–36]. For example, an array of coupled resonant elements leads to a constriction of the 1D continuum of guided modes to a transmission band of finite bandwidth, with sharp transitions in the photonic DOS occurring at the bandedges as in a photonic bandgap material.

Spectral constriction of the waveguide continuum, and the concomitant frequency dispersion, can also result in the slowing of light propagation which enables observation of additional non-Markovian phenomena. For instance, by placing a reflective boundary (mirror) on one end of a slow-light waveguide, a fraction of the emitter's radiation can be fed back from the waveguide reservoir to the emitter at significantly delayed timescales [37–39]. The non-Markovian regime is reached when $\tau_{\mathrm{d}}\Gamma_{\mathrm{1D}} > 1$, where Γ_{1D} is the emitter's emission rate into the waveguide and τ_{d} is the round-trip travel time of an emitted photon. Theoretical studies have shown that such non-Markovian delayed feedback in a 1D waveguide reservoir can lead to revivals in excited state population of an emitter as it undergoes spontaneous emission decay [37, 40–45], realization of stable bound states in a continuum (BIC) [46, 47], and enhanced collective effects including multipartite entanglement and superradiant emission from emitters interacting via a common waveguide channel [29, 48–52]. This deceptively simple mechanism of time-delayed feedback can also be used for the generation of multi-dimensional photonic cluster states by a single emitter, and has been proposed as a means for generating the universal resource states necessary for measurement-based quantum computation [7].

Superconducting microwave circuits incorporating Josephson-junction-based qubits [53, 54] represent a near-ideal test bed for studying the quantum dynamics of emitters interacting with a 1D continuum [55, 56]. In comparison to solid-state and atomic optical systems [57–60], superconducting microwave circuits can be created at a deep-sub-wavelength scale, giving rise to strong qubit-waveguide coupling far exceeding other qubit dissipative channels. This has enabled a variety of pioneering experiments probing qubit-waveguide radiative dynamics, employing waveguide spectroscopy [39, 61–63], time-dependent qubit measurements [64–67], and analysis of higher-order field correlations [68, 69]. Recent experiments have also explored the coupling of superconducting qubits to acoustic wave devices, demonstrating the capability of these systems to produce significant time-delayed feedback and remote entanglement of qubits [63, 67].

In this work, we present the design and characterization of an all-electrical slow-light waveguide consisting of a chain of coupled lumped-element superconducting resonators patterned on a Silicon microchip. We demonstrate that this compact, low-loss microwave waveguide has sharp bandedges, and a passband with group delay of 55 ns per centimeter over an 80 MHz bandwidth. Through the addition of strongly coupled Xmon-style superconducting qubits [16, 70] to the slow-light waveguide, we are able to realize a quantum emitter-reservoir system operating deep within the non-Markovian limit. Spectroscopic measurement of the coupled system shows the emergence of dressed qubit-photon resonant states near the bandedges of the constricted passband of the waveguide [18, 19, 62]. Using non-adiabatic tuning of the qubit emission frequency, we also measure the time-dependent dynamics of the qubit excited state population when it is resonant at different points across the bandgap and passband of the waveguide. We directly observe non-exponential, oscillatory radiative decay of the qubit, which modeling indicates is a result of the interference of the pair of bound and radiative dressed qubit-photon states that exist on either side of the bandedge of the slow-light waveguide [22]. Further, by terminating one-end of the slow-light waveguide with a reflective boundary, we explore the effects of time-delayed feedback on the qubit emission as it emits into the passband of the slow-light waveguide. In this regime, we observe multiple, well-resolved revivals in the qubit excited state population, and explore the cross-over between Markovian and non-Markovian emission dynamics through in situ tuning of the qubit coupling to the waveguide. From this series of measurements, we estimate the achievable fidelity of entangling a number of photon pulses emitted at different round-trip times of the waveguide, and find that the demonstrated qubit-waveguide system is a promising platform for the sequential generation of multi-dimensional photonic cluster states as described in the theoretical proposals of Refs. [7, 71–73].

2.2 Slow-Light Metamaterial Waveguide

In prior work studying superconducting qubit emission into a photonic bandgap waveguide [64], we employed a metamaterial consisting of a coplanar waveguide (CPW) periodically loaded by lumped-element resonators. In that geometry, whose circuit model simplifies to a transmission line with resonator loading in parallel to the line, one obtains high efficiency transmission with a characteristic impedance approximately that of the standard CPW away from the resonance frequency of the loading resonators, and a transmission stopband near resonance of the resonators. The spectral characteristics of the metamaterial in Ref. [64] were studied via spontaneous emission lifetime and lamb-shift measurements of a weakly coupled superconducting qubit, which revealed information about the local DOS at the qubit frequency that were consistent with the metamaterial's engineered dispersion. In contrast, here we seek a waveguide with high transmission efficiency, slow-light propagation within a transmission passband, and considerably stronger qubit coupling to the waveguide's guided modes. The stronger coupling renders the Born approximation inapplicable in such a system, where the effect of the qubit's interaction with the photonic reservoir takes on significantly more complexity than simply a decay rate dependent solely on the DOS at the qubit's frequency. Furthermore, the increased propagation delay gives rise to non-Markovian memory effects in the waveguide-mediated interactions between qubits, for which the waveguide degrees of freedom can no longer be be traced out, as in Ref. [65] for instance.

Large delay per unit area can be obtained by employing a network of sub-wavelength resonators, with light propagation corresponding to hopping from resonator-to-resonator at a rate set by near-field inter-resonator coupling. This area-efficient approach to achieving large delays is well-suited to applications where only limited bandwidths are necessary. However, realizing such a waveguide system in a compact chip-scale form factor requires a modular implementation that can be reliably replicated at the unit cell level without introducing spurious cell-to-cell couplings. In optical photonics applications, this sort of scheme has been realized in what are called coupled-resonator optical waveguides, or CROW waveguides [74, 75]. Here we employ a periodic array of capacitively coupled, lumped-element microwave resonators to form the waveguide. Such a resonator-based waveguide supports a photonic channel through which light can propagate, henceforth referred to as the passband, with bandwidth approximately equal to four times the coupling between the resonators, J. The limited bandwidth directly translates into large propagation delays; as can be shown (see Appendix 4.2), the delay in the resonator array is roughly ω_0/J longer than that of a conventional CPW of similar area, where ω_0 is the resonance frequency of the resonators.

An optical and scanning electron microscope (SEM) image of the unit cell of the metamaterial slow-light waveguide used in this work are shown in Fig. 2.1a. The cell consists of a tightly meandered wire inductor section (L_0; false color blue) and a top shunting capacitor (C_0; false color green), forming the lumped-element

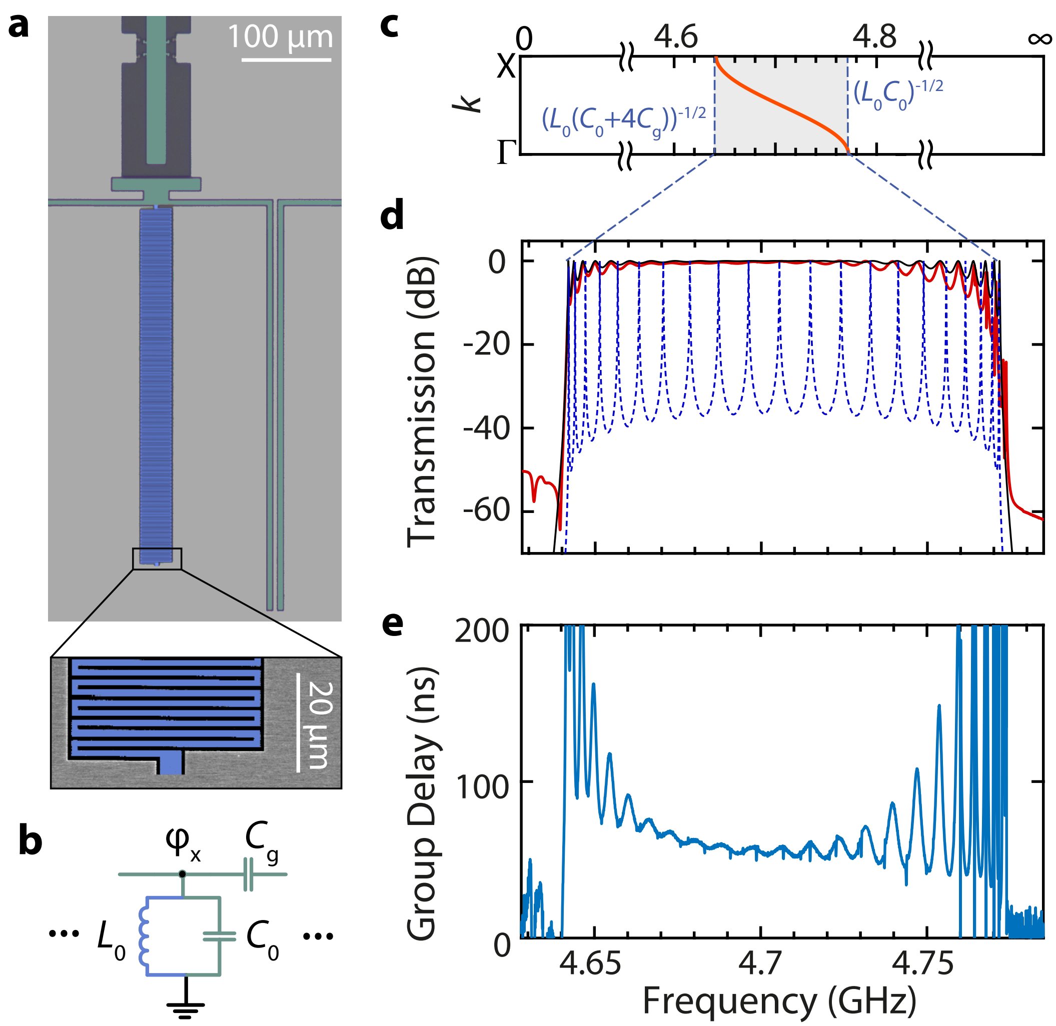

Figure 2.1: **Microwave coupled resonator array slow-light waveguide. a.** Optical image of a fabricated microwave resonator unit cell. The capacitive elements of the resonator are false colored in green, while the inductive meander is false colored in blue. The inset shows a false colored SEM image of the bottom of the meander inductor, where it is shorted to ground. **b.** Circuit diagram of the unit cell of the periodic resonator array waveguide. **c.** Theoretical dispersion relation of the periodic resonator array. See Appendix 4.2 for derivation. **d.** Transmission through a metamaterial slow-light waveguide spanning 26 resonators and connected to 50-Ω input-output ports. Dashed blue line: theoretical transmission of finite array without matching to 50-Ω boundaries. Black line: theoretical transmission of finite array matched to 50-Ω boundaries through two modified resonators at each boundary. Red line: measured transmission for a fabricated finite resonator array with boundary matching to input-output 50-Ω coplanar waveguides. The measured ripple in transmission is less than 0.5 dB in the middle of the passband. **e.** Measured group delay, τ_g. Ripples in τ_g are less than $\delta\tau_g = 5$ ns in the middle of the passband.

microwave resonator. Note that these delineations between inductor and capacitor are not strict, and that the meandered wire inductor (top shunting capacitor) has a small parasitic capacitance (parasitic inductance). The resonator is surrounded by a large ground plane (gray) which shields the meander wire section. Laterally extended 'wings' of the top shunting capacitor also provide coupling between the cells (C_g; false color green). Note that at the top of the optical image, above each shunting capacitor, we have included a long superconducting island (C_q; false color green); this is used in the next section as the shunting capacitance for Xmon qubits. Similar lumped-element resonators have been realized with internal quality factors of $Q_i \sim 10^5$ and small resonator frequency disorder [64], enabling propagation of light with low extinction from losses or disorder-induced scattering [76]. The waveguide resonators shown in Fig. 2.1a have a bare resonance frequency of $\omega_0/2\pi \approx 4.8$ GHz, unit cell length $d = 290$ μm, and transverse unit cell width $w = 540$ μm, achieving a compact planar form factor of $\bar{d}/\lambda = (\sqrt{dw})/(2\pi v/\omega_0) \approx 1/60$, where v is the speed of light in a CPW on a infinitely thick silicon substrate.

The unit cell is to a good approximation given by the electrical circuit shown in Fig. 2.1b, in which the photon hopping rate is $J \propto C_g/C_0$ [13]. We chose a ratio of $C_g/C_0 \approx 1/70$, which yields a delay per resonator of roughly 2 ns. Note that we have achieved this compact form factor and large delay per resonator while separating different lumped-element components by large amounts of ground plane, which minimizes spurious crosstalk between different unit cells. Analysis of the periodic circuit's Hamiltonian and dispersion can be found in Appendix 4.2, where the dispersion is shown to be $\omega_k = \omega_0/\sqrt{1 + 4\frac{C_g}{C_0}\sin^2(kd/2)}$. Figure 2.1c shows a plot of the theoretical waveguide dispersion for an infinitely periodic waveguide, where the frequency of the bandedges of the passband are denoted with the circuit parameters of the unit cell.

For finite resonator arrays, care must be taken to avoid reflections at the boundaries that would result in spurious resonances (see Fig. 2.1d, dashed blue curve, for example). To avoid these reflections, we taper the impedance of the waveguide by slowly shifting the capacitance of the resonators at the boundaries. In particular, we modify the first two unit cells at each boundary, but in principle, more resonators could have been modified for a more gradual taper. Increasing C_g to increase the coupling between resonators, and decreasing C_0 to compensate for resonance frequency changes, effectively impedance matches the Bloch impedance of the periodic structure in the passband to the characteristic impedance of the input-output waveguides [77]. In essence, this tapering achieves strong coupling of all normal modes of the finite structure to the input-output waveguides by adiabatically transforming guided resonator array modes into guided input-output waveguide modes. This loading of the normal modes lowers their Q such that they spectrally

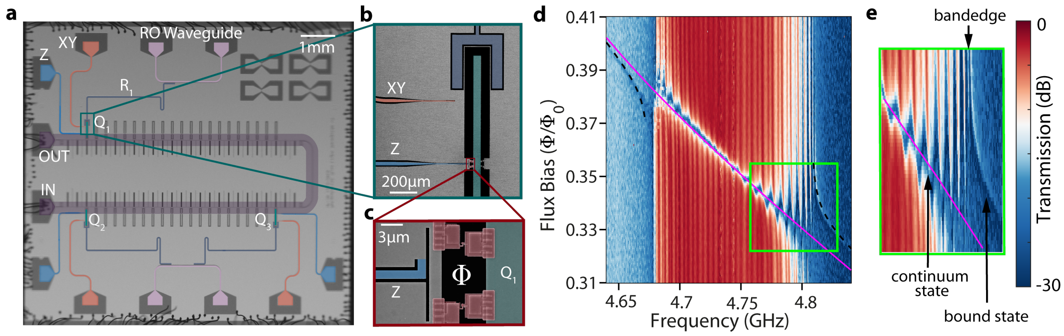

Figure 2.2: **Artificial atom coupled to a structured photonic reservoir. a.** False-colored optical image of a fabricated sample consisting of three transmon qubits (Q_1,Q_2,Q_3) coupled to a slow-light metamaterial waveguide composed of a coupled microwave resonator array. Each qubit is capacitively coupled to a readout resonator (false color dark blue) and a XY control-line (false color red), and inductively coupled to a Z flux-line for frequency tuning (false color light blue). The readout resonators are probed through feed-lines (false color lilac). The metamaterial waveguide path is highlighted in false color dark purple. **b.** SEM image of the Q_1 qubit, showing the long, thin shunt capacitor (false color green), XY control-line, the Z flux-line, and coupling capacitor to the readout resonator (false color dark blue). **c.** SEM zoom-in image of the Z flux-line and superconducting quantum interference device (SQUID) loop of Q_1 qubit, with Josephson Junctions and its pads false colored in crimson. **d.** Transmission through the metamaterial waveguide as a function of flux. The solid magenta line indicates the expected bare qubit frequency in the absence of coupling to the metamaterial waveguide, calculated based on the measured qubit minimum/maximum frequencies and the extracted anharmonicity. The dashed black lines are numerically calculated bound state energies from a model Hamiltonian of the system; see section 4.5 for further details. **e.** Zoom-in of transmission near the upper bandedge, showing the hybridization of the qubit with the bandedge, and its decomposition into a bound state in the upper bandgap and a radiative state in the continuum of the passband.

overlap and become indistinguishable, changing the DOS of a finite array from that of a multi-mode resonator to that of finite-bandwidth continuum with singular bandedges. Further details of the design of the unit cell and boundary resonators can be found in Appendix 4.3.

Using the above design principles, we fabricated a capacitively coupled 26-resonator array metamaterial waveguide. The waveguide was fabricated using electron-beam deposited aluminum (Al) on a silicon substrate and was measured in a dilution refrigerator; transmission measurements are shown in Fig. 2.1d,e, and further details of our fabrication methods and measurement set-up can be found in Appendix 4.1. We find less than 0.5 dB ripple in transmitted power and less than 10% variation in the group delay ($\tau_g \equiv -\frac{d\phi}{d\omega}$, $\phi = \arg(t(\omega))$, where t is transmission) across 80 MHz of bandwidth in the center of the passband, ensuring low distortion of propagating signals. Qualitatively, this small ripple demonstrates that we have realized a resonator array with small disorder and precise modification of the boundary resonators. More quantitatively, from the transmitted power measurements we extract a standard deviation in the resonance frequencies of $3 \times 10^{-4} \times \omega_0$ (see Appendix 4.4). Furthermore, we achieve $\tau_{\mathrm{d}} \approx 55$ ns of delay across the 1 cm metamaterial waveguide, corresponding to a slow-down factor given by the group index of $n_g \approx 650$. We stress that this group delay is obtained across the center of the passband, rather than near the bandedges where large (and undesirable) higher-order dispersion occurs concomitantly with large delays.

2.3 Non-Markovian Radiative Dynamics

In order to study the non-Markovian radiative dynamics of a quantum emitter, a second sample was fabricated with a metamaterial waveguide similar to that in the previous section, this time including three flux-tunable Xmon qubits [70] coupled at different points along the waveguide (see Fig. 2.2a-c). Each of the qubits is coupled to its own XY control line for excitation of the qubit, a Z control line for flux tuning of the qubit transition frequency, and a readout resonator (R) with separate readout waveguide (RO) for dispersive read-out of the qubit state. The qubits are designed to be in the transmon-limit [16] with large tunneling to charging energy ratio (see Refs. [64, 78] for further qubit design and fabrication details). As in the test waveguide of Fig. 2.1, the qubit-loaded metamaterial waveguide is impedance-matched to input-output 50-Ω CPWs. In order to extend the waveguide delay further, however, this new waveguide is realized by concatenating two of the test metamaterial waveguides together using a CPW bend and internal impedance matching sections. The Xmon qubit capacitors were designed to have capacitive coupling to a single unit cell of the metamaterial waveguide, yielding a qubit-unit cell coupling of $g_{\mathrm{uc}} \approx 0.8J$.

In this work, only one of the qubits, Q_1, is used to probe the non-Markovian emission dynamics of the qubit-waveguide system. The other two qubits are to be used in a separate experiment, and were detuned from Q_1 by approximately 1 GHz for all of the measurements that follow. At zero flux bias (i.e., maximum qubit frequency), the measured parameters of Q_1 are: $\omega_{ge}/2\pi = 5.411$ GHz, $\eta/2\pi = (\omega_{ef} - \omega_{ge})/2\pi = -235$ MHz, $\omega_r/2\pi = 5.871$ GHz, and $g_r/2\pi = 88$ MHz. Here, $|g\rangle$, $|e\rangle$, and $|f\rangle$ are the vacuum, first excited, and second excited states of the Xmon qubit, with ω_{ge} the fundamental qubit transition frequency, ω_{ef} the first excited state transition frequency, and η the anharmonicity. ω_r is the readout resonator frequency, and g_r is the bare coupling rate between the qubit and the readout resonator.

As an initial probe of qubit radiative dynamics, we spectroscopically probed the interaction of Q_1 with the structured 1D continuum of the metamaterial waveguide. These measurements are performed by tuning ω_{ge} into the vicinity of the passband and measuring the waveguide transmission spectrum at low power (such that the effects of qubit saturation can be neglected). A color intensity plot of the measured transmission spectrum versus flux bias used to tune the qubit frequency is displayed in Fig. 2.2d. These spectra show a clear anti-crossing as the qubit is tuned towards either bandedge of the passband (a zoom-in near the upper bandedge of the passband is shown in Fig. 2.2e). As has been shown theoretically [22, 23], in the single excitation manifold the interaction of the qubit with the waveguide results in a pair of qubit-photon dressed states of the hybridized system, with one state in the passband (a delocalized 'continuum' state) and one state in the bandgap (a localized 'bound' state). This arises due to the large peak in the photonic DOS at the bandedge (in the lossless case, a van Hove singularity), the modes of which strongly couple to the qubit with a coherent interaction rate of $\Omega_{\mathrm{WG}} \approx (g_{\mathrm{uc}}^4/4J)^{1/3}$, resulting in a dressed-state splitting of $2\Omega_{\mathrm{WG}}$. This splitting has been experimentally shown to be a spectroscopic signature of a non-Markovian interaction between an emitter and a photonic crystal reservoir [61, 62]. Further details and discussion can be found in Appendix 4.2 and section 4.5.

The dressed state with frequency in the passband is a radiative state which is responsible for decay of the qubit into the continuum [19]. On the other hand, the state with frequency in the gap is a qubit-photon bound state, where the qubit is self-dressed by virtual photons that are emitted and re-absorbed due to the lack of propagating modes in the waveguide for the radiation to escape. This bound state assumes an exponentially shaped photonic wavefunction of the form $\sum_x e^{-|x|/\lambda}\hat{a}_x^\dagger |\mathrm{vac}\rangle$, where $|\mathrm{vac}\rangle$ is the state with no photons in the waveguide, $\hat{a}_x^\dagger$ is the creation operator of a photon in unit cell at position x (with the qubit located at $x = 0$), and $\lambda \approx \sqrt{J/(E_b - \omega_0)}$ is the state's localization length. In the theoretical limit of an infinite array, and in absence of intrinsic resonator and qubit losses, the qubit component of the bound state does not decay even though it is hybridized with the waveguide continuum; a behavior distinct from conventional open quantum systems. Practically, however, intrinsic losses and the overlap between the bound state's photonic wavefunction and the input-output waveguides will result in decay of the qubit-photon bound state.

In complement to spectroscopic probing of the qubit-reservoir system, and in order to directly study the population dynamics of the qubit-photon dressed states, we also performed time-domain measurements as shown in Fig. 2.3. In this protocol

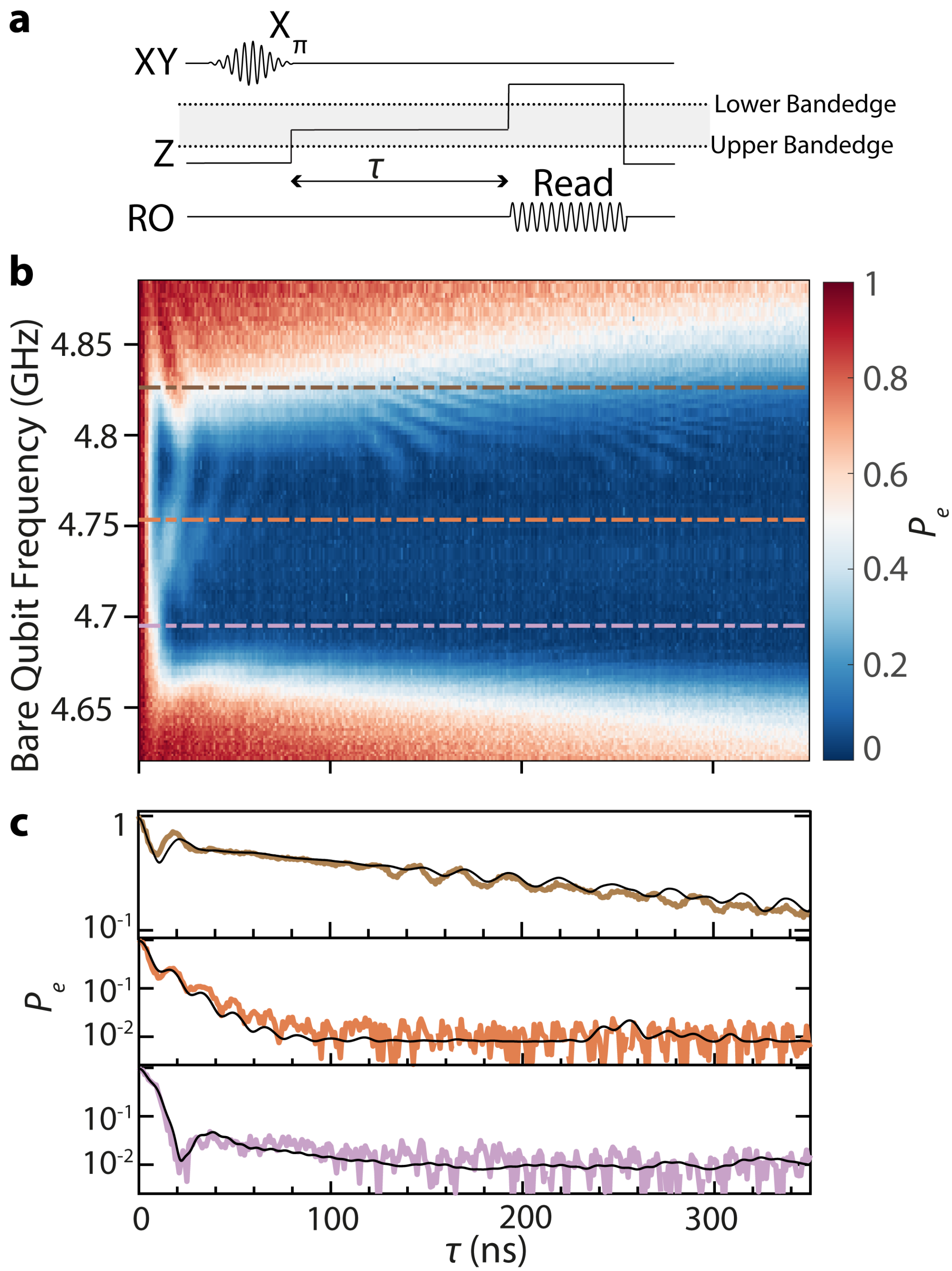

Figure 2.3: **Non-Markovian radiative dynamics in a structured photonic reservoir. a.** Pulse sequence for the time-resolved measurement protocol. The qubit is excited while its frequency is 250 MHz above the upper bandedge, and then it is quickly tuned to the desired frequency (ω'_{ge}) for a interaction time τ with the reservoir. After interaction, the qubit is quickly tuned below the lower bandedge for dispersive readout. **b.** Intensity plot showing the excited state population of the qubit versus interaction time with the metamaterial waveguide reservoir as a function of the bare qubit frequency. **c.** Line cuts of the intensity plot shown in (**b**), where the color of the plotted curve matches the corresponding horizontal dot-dashed curve in the intensity plot. Solid black lines are numerical predictions of a model with experimentally fitted device parameters and an assumed 0.8% thermal qubit population (see Appendix 4.5 for further details).

(illustrated in Fig. 2.3a), we excite the qubit to state $|e\rangle$ with a resonant π-pulse on the XY control line, and then rapidly tune the qubit transition frequency using a fast current pulse on the Z control line to a frequency (ω'_{ge}) within, or in the vicinity of, the slow-light waveguide passband. After an interaction time τ, the qubit is then rapidly tuned away from the passband, and the remaining qubit population in $|e\rangle$ is measured using a microwave probe pulse (RO) of the read-out resonator which is dispersively coupled to the qubit. The excitation of the qubit is performed far from the passband, permitting initialization of the transmon qubit whilst it is negligibly hybridized with the guided modes of the waveguide. Dispersive readout of the qubit population is performed outside of the passband in order to minimize the loss of population during readout. Note that, as illustrated in Fig. 2.3a, the qubit is excited and measured at different frequencies on opposite sides of the passband; this is necessary to avoid Landau-Zener interference [79].

Results of measurements of the time-domain dynamics of the qubit population as a function of ω'_{ge} (the estimated bare qubit frequency during interaction with the waveguide) are shown as a color intensity plot in Fig. 2.3b. In this plot, we observe a 400-fold decrease in the $1/e$ excited state lifetime of the qubit as it is tuned from well outside the passband to the middle of the slow-light waveguide passband, reaching a lifetime as short as 7.5 ns. Beyond the large change in qubit lifetime within the passband, several other more subtle features can be seen in the qubit population dynamics near the bandedges and within the passband. These more subtle features in the measured dynamics show non-exponential decay, with significant oscillations in the excited state population that is a hallmark of strong non-Markovianity in quantum systems coupled to amplitude damping channels [80, 81].

The observed qubit emission dynamics in this non-Markovian limit are best understood in terms of the qubit-waveguide dressed states. Fast (i.e., non-adiabatic) tuning of the qubit in state $|e\rangle$ into the proximity of the passband effectively initializes it into a superposition of the bound and continuum dressed states. The observed early-time interaction dynamics of the qubit with the waveguide then originate from interference of the dressed states, which leads to oscillatory behavior in the qubit population analogous to vacuum-Rabi oscillations [82]. The frequency of these oscillations is thus set by the difference in energy between the dressed states. The amplitude of the oscillations, on the otherhand, quickly decay away as the energy in the radiative continuum dressed state is lost into the waveguide.

All of these features can be seen in Fig. 2.3c, which shows plots of the measured time-domain curves of the qubit excited state population for bare qubit frequencies near the top, middle, and bottom of the passband. Near the upper bandedge frequency, we observe an initial oscillation period as expected due to dressed state interference. Once the continuum dressed state has decayed away, a slower decay region free of oscillations can be observed (this is due to the much slower decay of the remaining qubit-photon bound state). Finally, around $\tau \approx 115$ ns, there is an onset of further small amplitude oscillations in the qubit population. These late-time oscillations can be attributed to interference of the remaining bound state at the site of the qubit with weak reflections occurring within the slow-light waveguide of the initially emitted continuum dressed state. The 115 ns timescale corresponds to the round trip time between the qubit and the CPW bend that connects the two slow-light waveguide sections.

In the middle of the passband, we see an extended region of initial oscillation and rapid decay, albeit of smaller oscillation amplitude. This is a result of the much smaller initial qubit-photon bound state population when tuned to the middle of the passband. Near the bottom of the passband we see rapid decay and a single period of a much slower oscillation. This is curious, as the dispersion near the upper and lower bandedge frequencies of the slow-light waveguide is nominally equivalent. Further modelling has shown this is a result of weak non-local coupling of the Xmon qubit to a few of the nearest-neighbour unit cells of the waveguide. Referring to Fig. 2.1c, the modes near the lower bandedge occur at the X-point of the Brillouin zone edge where the modes have alternating phases across each unit cell, thus extended coupling of the Xmon qubit causes cancellation-effects which reduces the qubit-waveguide coupling at the lower frequency bandedge. Further detailed numerical model simulations of our qubit-waveguide system via a tight-binding model and a circuit model, as well as the correspondence between the observed dynamics and the theory of spontaneous emission by a two level system near a photonic bandedge [22], are given in Appendix 4.5.

2.4 Time-Delayed Feedback

In order to further study the late-time, non-Markovian memory effects of the qubit-waveguide dynamics, we also perform measurements in which the end of the waveguide furthest from qubit Q_1 is terminated with an open circuit, effectively creating a 'mirror' for photon pulses stored in the slow-light waveguide reservoir. As illustrated in Fig. 2.4a, we achieve this *in situ* by connecting the input microwave cables of the dilution refrigerator to the waveguide via a microwave switch. The position of the switch, electrically closed or open, allows us to study a truly open environment for the qubit or one in which delayed-feedback is present, respectively (see Appendix 4.1 for further details).

Performing time-domain measurements with the mirror in place and with the qubit frequency in the passband, we observe recurrences in the qubit population at one and two times the round-trip time of the slow-light waveguide that did not appear in the absence of the mirror (see Fig. 2.4b). The separation of timescales between full population decay of the qubit and its time-delayed re-excitation demonstrates an exceptionally long memory of the reservoir due to its slow-light nature, and places this experiment in the deep non-Markovian regime [37]. The small recurrence levels as they appear in Fig. 2.4b are not due to inefficient mirror reflection, but rather can be explained as follows. Because the qubit emits towards both ends of the waveguide, half of the emission is lost to the unterminated end, while the other half is reflected by the mirror and returns to the qubit. In addition, the exponentially decaying temporal profile of the emission leads to inefficient re-absorption by the qubit and further limits the recurrence (see, for instance, Ref. [83, 84] for details). These two effects can be observed in simulations of a qubit coupled to a dispersion-less and loss-less waveguide (pink dotted line; for more details, see Ref. [41] and Appendix 4.6). The remaining differences between the simulation and the measured population recurrence (blue solid line) can be explained by the effects of propagation loss and pulse distortion due to the slow-light waveguide's dispersion.

We also further probed the dependence of this phenomenon on the strength of coupling to the waveguide continuum by parametric flux modulation of the qubit transition frequency [85] when it is far detuned from the passband. This modulation creates sidebands of the qubit excited state, which are detuned from ω_{ge} by the frequency of the flux tone ω_{mod}. By choosing the modulation frequency such that a first-order sideband overlaps with the passband, the effective coupling rate of the qubit with the waveguide at the sideband frequency was reduced approximately by a factor of $\mathcal{J}_1^2[\epsilon/\omega_{\text{mod}}]$, where ϵ is the modulation amplitude and $\mathcal{J}_1$ is a Bessel function of the first kind ($\epsilon/\omega_{\text{mod}}$ is the modulation index). Keeping a fixed ω_{mod}, we observe purely exponential decay at small modulation amplitudes. However, above a modulation amplitude threshold we again observe recurrences in the qubit population at the round-trip time of the metamaterial waveguide, demonstrating a continuous transition from Markovian to non-Markovian dynamics (see Appendix 4.6 for further comparisons between this data and the theoretical model of Ref. [41])

.

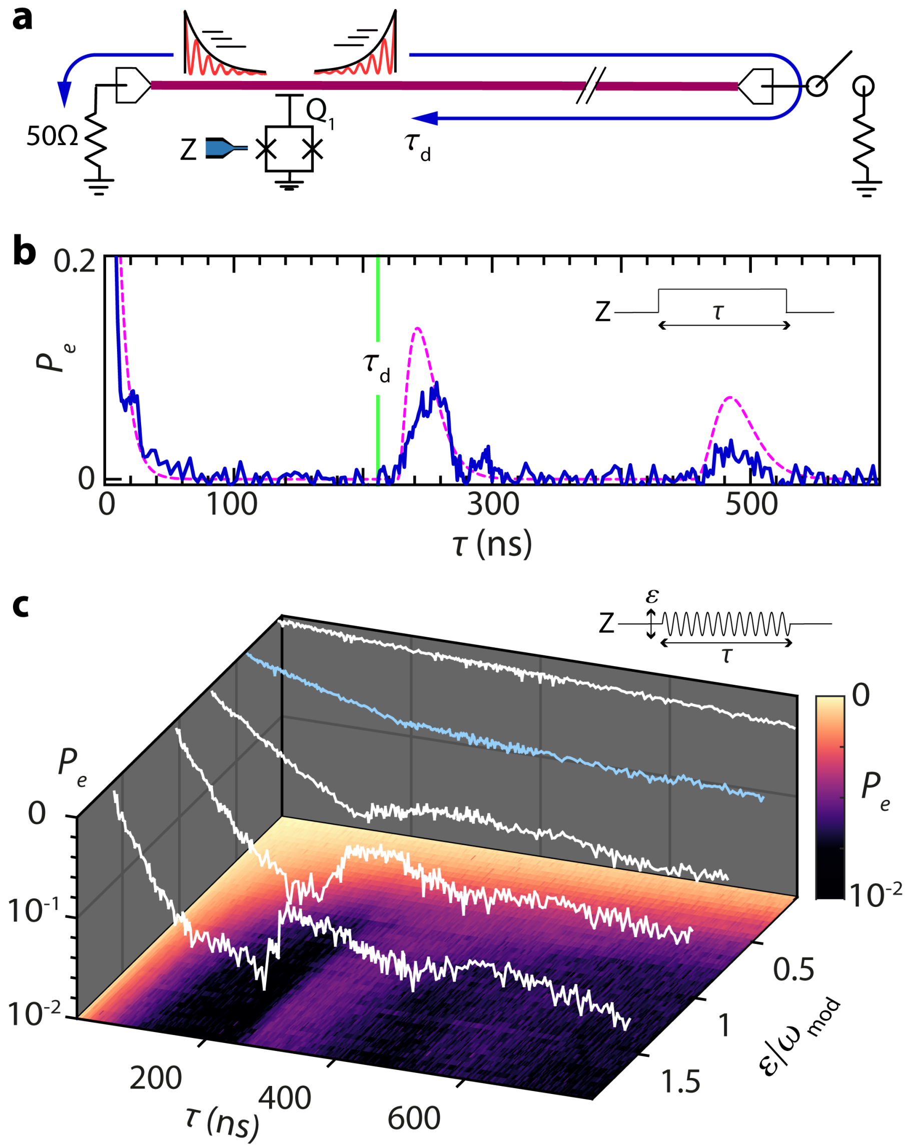

Figure 2.4: **Time-delayed feedback from a slow-light reservoir with a reflective boundary a.** Illustration of the experiment, showing the qubit coupled to the metamaterial waveguide which is terminated on one end with a reflective boundary via a microwave switch. **b.** Measured population dynamics of the excited state of the qubit when coupled to the metamaterial waveguide terminated in a reflective boundary. Here the bare qubit is tuned into the middle of the passband. The onset of the population revival occurs at $\tau = 227$ ns, consistent with round-trip group delay (τ_d) measurements at that frequency, while the emission lifetime of the qubit is $(\Gamma_{1D})^{-1} = 7.5$ ns. The magenta curve is a theoretical prediction for emission of a qubit into a dispersionless, lossless semi-infinite waveguide with equivalent τ_d and Γ_{1D} (see Appendix 4.6 for details). **c.** Population dynamics under parametric flux modulation of the qubit, for varying modulation amplitudes, demonstrating a Markovian to non-Markovian transition. When the modulation index (ϵ/ω_{mod}) is approximately 0.4 we have $\Gamma_{1D}(\epsilon) = 1/\tau_d$; the corresponding dynamical trace is colored in blue.

2.5 Conclusion

In conclusion, by strongly coupling Xmon qubits to a 1D structured photonic reservoir consisting of a metamaterial slow-light waveguide, we are able to probe the non-Markovian dynamical regime of waveguide quantum electrodynamics. In this regime, we observe non-exponential qubit spontaneous decay near the bandedges of the slow-light waveguide, attributable to interference resulting from the splitting of the qubit state into a radiative state in the passband and a bound state in the bandgap region of the metamaterial waveguide. Moreover, by placing a reflective boundary on one end of the waveguide, we observe recurrences in the qubit population at the round-trip time of an emitted photon, as well as a Markovian to non-Markovian transition when varying the qubit-waveguide interaction strength.

The demonstrated ability to achieve a true finite-bandwidth continuum with time-delayed feedback opens up several new research avenues for exploration [38, 40–52, 86]. As a straightforward extension of the current work, one may probe the qubit-waveguide-mirror system in a continuous, strongly-driven fashion, and use tomography to study photon correlations in the output radiation field [38]. This output field, with expected photon stream of high entanglement dimensionality, has a direct mapping to continuous matrix product states which can used for analog simulations of higher-dimension interacting quantum fields [86, 87]. With technical advancements in the tomography of microwave fields [69, 88], and realization of single-microwave-photon qubit detectors [89–91], the basic tools for characterization of these entangled photonic states and their quantum many-body-system analogues are now available.

Looking forward even further, the use of the multi-level structure of the transmon qubit, in conjunction with a second distant qubit side-coupled to the waveguide as a switchable mirror, can be used to generate 2D cluster states [7]. This system is capable of entangling consecutively emitted photons as well as photons separated in time by the round-trip waveguide delay, τ_{d}, thus achieving a $N \times M$ 2D cluster state where N is limited by the number of non-overlapping photons that can fit in the slow-light waveguide and $N \cdot M$ is limited by the coherence time of the emitter. With our achieved device parameters, we estimate that a 3×3 2D cluster state could be generated with fidelity greater than 50% (see Ref. [7] and Chapter 3 for further details). Realistic improvements in τ_{d} and T_2^* could increase the size of the state by at least an order of magnitude, with even further improvement possible via incorporation of compact high kinetic inductance superconducting thin-film resonators or acoustic delay lines [67, 92]. Additionally, by controlling the number of reflections a photon undergoes before exiting the metamaterial waveguide, cluster states of 3D or higher entanglement dimensionality can be generated, enabling the realization of fault-tolerant measurement-based quantum computation schemes [7, 73, 93].

The essential paradigm of our experiment, consisting of a single artificial atom coupled to a waveguide with a long propagation delay and sharp spectral cutoffs, could in principle be achieved in other solid-state and atomic optical system, such as trapped atoms coupled to a nanofiber or defect centers coupled to photonic crystal waveguides [57–60]. The challenge with such modalities, however, is achieving a large coupling of the emitter to the guided modes of the waveguide relative to its decay rate as well as the propagation delay of the waveguide. From an application standpoint, however, the optical domain is of great interest due to the mature technology in single-photon detectors, photonic integrated circuits for linear and nonlinear optics, and optical fibers for long range communication.

Chapter 3

UTILIZATION OF METAMATERIAL WAVEGUIDE FOR 2D CLUSTER STATE GENERATION

We envision leveraging the large time delay and sharply varying photonic DOS of a slow-light metamaterial waveguide, along with the transmon qubit multi-level structure, to generate a 2D photonic cluster state. Given a typical transmon anharmonicity of 300 MHz, tuning the $e - f$ transition instead of the $g - e$ transition into the middle of the passband would situate the $g - e$ transition frequency more than 200 MHz above the upper bandedge in our current waveguide devices. The corresponding level structure would then consist of two metastable states ($|g\rangle$ and $|e\rangle$) and a third level ($|f\rangle$) that is strongly coupled to the waveguide. It has been previously shown that such a ladder-like level structure can be utilized to generate 1D cluster states of time-bin photonic qubits through a sequential emission process [71, 94, 95].

In addition, the non-Markovian nature of the slow-light waveguide reservoir can be further exploited to enrich this one-dimensional entanglement to higher dimensions via time-delayed feedback [7]. In the case of 2D cluster state generation, this can be accomplished by using a metamaterial waveguide terminated on one end, coupling an emitter qubit to the terminated end of the waveguide, and using a second tunable qubit coupled to the output port of the waveguide as a single photon switchable mirror [96]. This mirror could be periodically switched on and off in a manner where consecutively emitted photons reflect on the mirror, interact a second time with the qubit, and subsequently exit through the waveguide's output port without additional reflections, with facile access to the photons for subsequent measurement enabled by matching of the slow-light metamaterial waveguide to a 50-Ω output waveguide. This resource efficient scheme, requiring only two qubits, entangles photons separated in time by τ_{d} in addition to the 1D entanglement between consecutively emitted photons, thus achieving a $N \times M$ 2D cluster state, where N is limited by the number of time-bin qubits that can fit in the slow-light waveguide and $N \cdot M$ is limited by the coherence time of the emitter. And remarkably, increasing the number of qubit-photon interaction events by simply increasing the number of reflections in the metamaterial waveguide allows for generation of cluster states with even higher entanglement dimensionality, paving the way for fault-tolerant measurement-based quantum computation [7, 73, 93].

Moreover, leveraging the rapid flux control of the qubit's transition frequency confers several additional advantages to the generation of multi-dimensional cluster states. For instance, it enables selective coupling and de-coupling of the $|f\rangle$ state to the waveguide via control of the detuning of the $e - f$ transition to the passband, allowing for high-fidelity manipulation of the emitter's three level quantum state separate from photon emission and re-absorption. Additionally, controlling the qubit-waveguide interaction strength via parametric flux modulation of the qubit frequency, as discussed in the main text, allows for pulse shaping of the emitted photons [97–99], which yields multiple benefits. Firstly, the fidelity of the photon re-absorption process can be significantly improved by shaping the photons to have a time-symmetric envelope with bandwidth less than Γ_{1D} [7, 83, 84]. This directly improves the fidelity of the entanglement between time-bin photonic qubits that occurs via the time-delayed feedback mechanism. Secondly, pulse-shaping allows for pre-compensation of the waveguide's residual dispersion near the middle of the passband [100], preventing broadening and distortion of propagating photons that could hinder their eventual measurement.

Already with our achieved device parameters of $\tau_{\mathrm{d}} = 227$ ns and $T_2^* = 3\mu s$ (measured at a flux insensitive sweetspot), along with an increased Γ_{1D} by a factor of two, entangling between individual time-bin qubits can be performed with over 95% fidelity through the techniques discussed in Ref. [7], allowing for generation of cluster states of up to $\sim$ 9 photons. Note that, due to the enhancement of the qubit-waveguide interaction strength via the slow-light effect [101, 102], doubling the Γ_{1D} achieved in this work would correspond to only a small increase of $\sim$ 2 fF in the capacitive coupling of the qubit to the metamaterial waveguide. Further, realistic increases in τ_{d} and T_2^* would increase the size of possible states by at least an order of magnitude; with ample room for more substantial improvement via incorporation of even more compact high kinetic inductance superconducting thin-film resonators for larger delays, and utilization of error protected qubits [103, 104] or lower-loss superconducting films [105] for higher qubit coherence. And finally, we note that techniques for tomography of microwave fields [69, 88] and single-photon detection of microwave photons utilizing superconducting qubits [89–91] have attained significant maturity over the last decade, enabling characterization of generated cluster states and their use in measurement-based quantum computation.

Chapter 4

APPENDIX: DETAILS OF DEVICE DESIGN, FABRICATION, MEASUREMENT SETUP, AND MODELING

4.1 Fabrication and Measurement Setup

Device Fabrication

The devices used in this work were fabricated on 10 mm × 10 mm silicon substrates [Float zone (FZ) grown, 525 μm thickness, > 10kΩ-cm resistivity], following similar techniques as in Ref. [78]. After standard solvent cleaning of the substrate, our first aluminum (Al) layer consisting of the ground plane, CPWs, metamaterial waveguide, and qubit capacitor was patterned by electron-beam lithography of our resist followed by electron-beam evaporation of 120 nm aluminum at a rate of 1 nm/s. A liftoff process performed in n-methyl-2-pyrrolidone at 80 °C for 2.5 hours (with 10 minutes of ultrasonication at the end) then yielded the aforementioned metal structures.

In our qubit device, the Josephson junctions were fabricated using double-angle electron beam evaporation of 60 nm and 120 nm of Al (at 1 nm/s) on suspended Dolan bridges, with an intervening 20 minute oxidation and a subsequent 2 minute oxidation at 10 mbar, followed by liftoff as described above. Note that prior to the double-angle evaporation, the sample was cleaned by an oxygen plasma treatment and a HF vapor etch. Finally, in order to electrically connect the evaporated Josephson junctions to the first Al layer, a 6 min argon ion mill was performed to locally remove surface aluminum oxide around the areas of overlap between the first Al layer and the Josephson junctions, which was followed by evaporation of an additional "bandage" layer of 140 nm Al that electrically connected the metal layers. Asymmetric Josephson junctions were fabricated in all qubits' SQUID loops to reduce dephasing from flux noise, with a design ratio of the larger junction area to the smaller junction area of approximately 6.

Measurement Setup

A schematic of the measurement chain used in this work is shown in Fig. 4.1. Measurements were performed in a 3He/4He dry dilution refrigerator, with a base fridge temperature at the mixing chamber (MXC) plate of T_{f} = 12 mK. The waveguide sample was wire bonded to a CPW printed circuit board (PCB) with coaxial con-

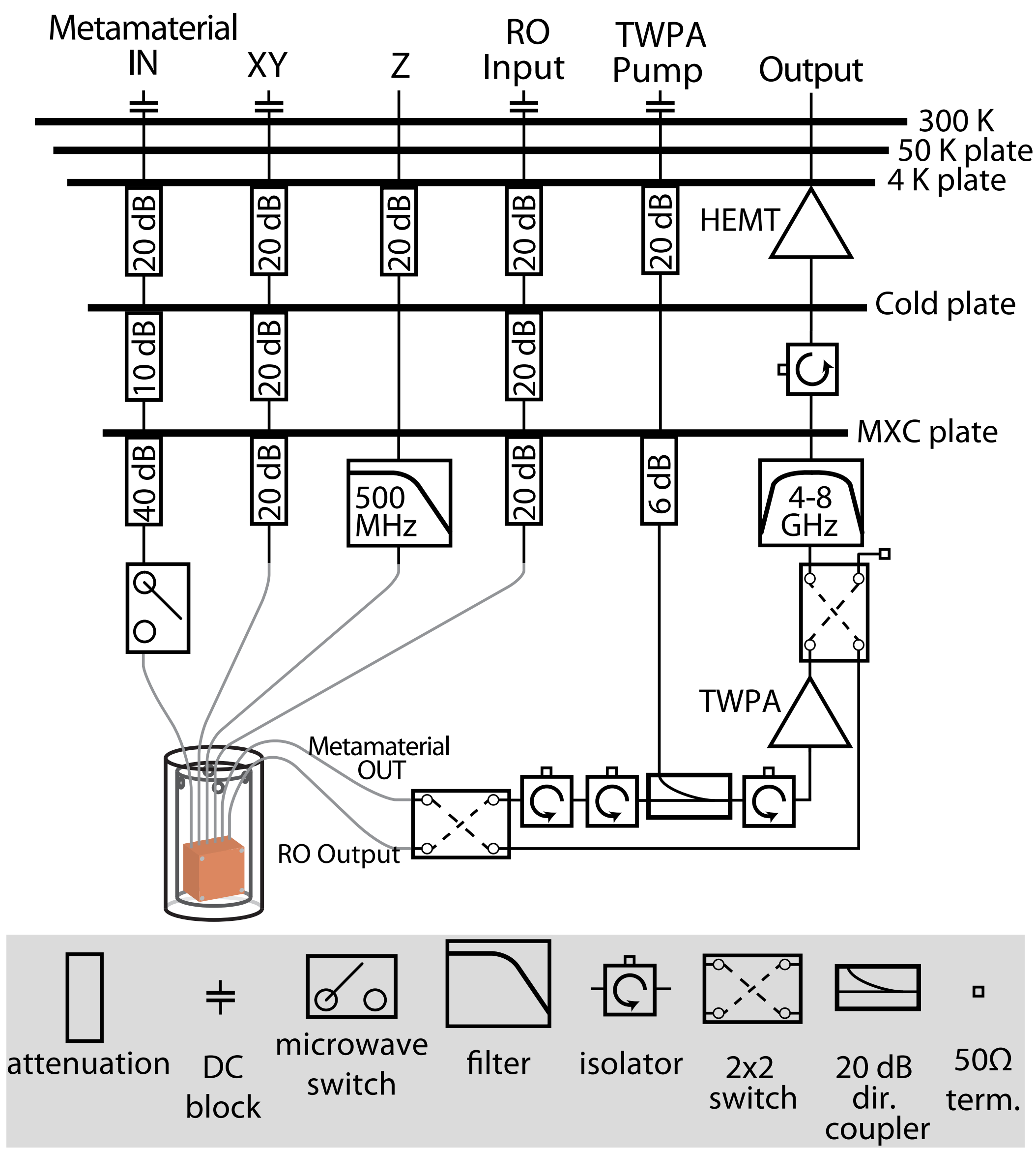

Figure 4.1: **Schematic of the measurement chain inside the dilution refrigerator.** See Appendix text for further details ("dir" is shorthand for "directional", and "term." is shorthand for "termination"). See Fig. 2.2 for electrical connections at the sample.

nectors, and housed inside a small copper box that is mounted to the MXC plate of the fridge. The copper box and sample were mounted inside a cryogenic magnetic shield to reduce the effects of stray magnetic field.

Attenuators were placed at several temperature stages of the fridge to provide thermalization of the coaxial input lines, and to reduce thermal microwave noise at the input to the sample. We used different attenuation configurations for our GHz microwave lines (Metamaterial IN, XY, RO Input, TWPA pump) as compared to our flux line (Z), with significantly less attenuation for the latter, for reasons explained in Ref. [106]. In addition, we included in the flux line a (reflective) low-pass filter, with corner frequency at 500 MHz, to minimize thermal noise photons at higher frequencies while maintaining short rise and fall time of pulses for fast flux control. Also note that the 40 dB attenuation of the "Metamaterial IN" line at the MXC plate includes a 20 dB thin-film "cold attenuator" [107] to ensure a more complete reduction of thermal photons in the metamaterial waveguide.

Our amplifier chain at the "Output" line consisted of a travelling-wave parametric amplifier (TWPA) as the initial amplification stage [108], followed by a CITCRYO4-12A high mobility electron transistor (HEMT) amplifier mounted at the 4K plate, and additional amplifiers at room temperature (Miteq AFS3-00101200-42-LN-HS, AMT A0262). For operation of the TWPA, a microwave pump signal was added to the amplifier via the coupled port of a 20dB directional coupler, with its isolated port terminated in 50-Ω. In between the two amplifiers, we have included a reflective bandpass filter (thermalized to the MXC plate) to suppress noise outside of 4–8 GHz, and used superconducting NbTi cables to minimize loss from the MXC plate to the 4K plate. We have also included two isolators in between the directional coupler and the sample in order to shield the sample from the strong TWPA pump, as well as an isolator in between the TWPA and the directional coupler in order to suppress any standing waves between the two elements due to spurious impedance mismatches; our isolators consist of 3 port circulators with the third port terminated in 50-Ω. All 50-Ω terminations are rated for cryogenic operaion and are thermalized to the MXC plate in order to suppress thermal noise from their resistive elements.

We also employed microwave switches in our measurement chain in order to provide *in situ* experimental flexibility in the following manner. As discussed in the main text, in between the "Metamaterial IN" chain and the metamaterial waveguide, we have placed a Radiall R573423600 microwave switch. By electrically opening the switch, we can establish an open circuit at the end of the waveguide furthest from Q_1, effectively creating a mirror for emission from Q_1, and thereby inducing time-delayed feedback.

In addition, in order to utilize our amplifier chain for either spectroscopic or time-domain measurements within the same cool-down, we employed Radiall R577432000 2x2 microwave switches for selective routing of the outputs of the metamaterial waveguide or the readout waveguide to the amplification chain. With our switch configuration, we ensured that when routing the readout waveguide output to the amplification chain, the metamaterial waveguide output was connected to a 50-Ω termination. This allowed us to maintain a 50-Ω environment at the metamaterial output at all times, and thereby ensured that the metamaterial waveguide remained an open quantum system due to its coupling to the 50-Ω continuum of modes. By employing two 2x2 switches instead of one, we had the ability to bypass the TWPA amplifier if desired, although ultimately the TWPA was used when collecting all measurement data presented in Figs. 2.2–2.4.

For spectroscopic measurements, the "Metamaterial IN" and "Output" lines were connected to the input and output of a ZNB20 Rohde & Schwarz vector network analyzer (VNA), respectively. For time-domain measurements, GHz excitation and readout pulses were generated by upconversion of MHz IF in-phase (I) and quadrature (Q) signals sourced from a Keysight M320XA arbitrary waveform generator (AWG), utilizing a Marki IQ-4509 IQ mixer and a LO tone supplied by a BNC 845 microwave source. Following amplification, output readout signals were down-converted (using an equivalent mixer and the same LO source) and subsequently digitized using an Alazar ATS9360 digitizer. For all measurements, qubit flux biasing was also sourced from a M320XA AWG, the TWPA pump tone was sourced by an Agilent E8257D microwave source, and all inputs to the dilution refrigerator were low-pass filtered and attenuated such that the noise levels from the electronic sources were reduced to a 300 K Johnson-Nyquist noise level.

4.2 Capacitively Coupled Resonator Array Waveguide Fundamentals

Band Structure Analysis

We consider a periodic array of capacitively coupled LC resonators, with unit cell circuit diagram shown in Fig. 2.1b. The Lagrangian for this system can be constructed as a function of node fluxes ϕ_x of the resonators, and is written as,

$$L = \sum_x \left[\frac{1}{2} C_0 \dot{\phi}_x^2 + \frac{1}{2} C_g (\dot{\phi}_x - \dot{\phi}_{x-1})^2 - \frac{{\phi_x}^2}{2L_0} \right]. \tag{4.1}$$

Since we seek traveling wave solutions to the problem, it is convenient to work with the Fourier transform of the node fluxes, defined as

$$\phi_k = \frac{1}{\sqrt{M}} \sum_{x=-N}^{N} \phi_x e^{-ikxd}, \tag{4.2}$$

where $M = 2N + 1$ is the total number of periods of a structure with periodic boundary conditions, d is the lattice constant of the resonator array, and k are the discrete momenta of the first Brillouin zone's guided modes and are given by $k = \frac{2\pi m}{Md}$ for integer $m = [-N, N]$. Using the inverse Fourier transform,

$$\phi_x = \frac{1}{\sqrt{M}} \sum_k \phi_k e^{ikxd}, \tag{4.3}$$

we arrive at the following k-space Lagrangian

$$L = \sum_k \left[\frac{1}{2} C_0 \dot{\phi}_k \dot{\phi}_{-k} + \frac{1}{2} C_g \dot{\phi}_k \dot{\phi}_{-k} \left| 1 - e^{-ikd} \right|^2 - \frac{\phi_k \phi_k}{2L_0} \right], \tag{4.4}$$

where we note that $\left|1 - e^{-ikd}\right|^2$ is equivalent to $4\sin^2(kd/2)$. We then obtain the Hamiltonian via the standard Legendre transformation using the canonical node charges $Q_k = \frac{\partial L}{\partial \dot{\phi}_k} = \dot{\phi}_{-k} \left(C_0 + 4C_g \sin^2(kd/2) \right)$, yielding:

$$H = \sum_k \left[\frac{1}{2} \frac{Q_k Q_{-k}}{\left(4C_g \sin^2(kd/2) + C_0 \right)} + \frac{\phi_k \phi_{-k}}{2L_0} \right]. \tag{4.5}$$

Promoting charge and flux to quantum operators and utilizing the canonical commutation relation $\left[\hat{\phi}_k, \hat{Q}_{k'}\right] = i\hbar\delta_{kk'}$, we define the following creation and annihilation operators:

$$\begin{aligned} \hat{a}_k &= \sqrt{\frac{m_k \omega_k}{2\hbar}} \left(\hat{\phi}_k + \frac{i}{m_k \omega_k} \hat{Q}_{-k} \right), \\ \hat{a}_k^\dagger &= \sqrt{\frac{m_k \omega_k}{2\hbar}} \left(\hat{\phi}_{-k} + \frac{i}{m_k \omega_k} \hat{Q}_k \right), \end{aligned} \tag{4.6}$$

where $m_k = \left(C_0 + 4C_g \sin^2(kd/2) \right)$. The resulting dispersion relation, ω_k, plotted in Fig. 2.1c is given by,

$$\omega_k = \frac{\omega_0}{\sqrt{1 + 4\frac{C_g}{C_0}\sin^2(kd/2)}}, \tag{4.7}$$

where $\omega_0 = 1/\sqrt{L_0 C_0}$, and $\left[\hat{a}_k, \hat{a}^\dagger_{k'}\right] = \delta_{kk'}$. Expressing the flux and charge operators in terms of $\hat{a}_k, \hat{a}^\dagger_{k'}$ and substituting them into Eq. (4.5), we recover the second-quantized Hamiltonian in the diagonal k-space basis

$$\hat{H} = \sum_k \hbar\omega_k \left(\frac{1}{2} + \hat{a}^\dagger_k \hat{a}_k\right). \tag{4.8}$$

Note that, given the translational invariance of the capacitively coupled resonator array circuit, it was expected that the the Hamiltonian would be diagonal in the Fourier plane-wave basis (Bloch Theorem).

Also note that, for two capacitively coupled LC resonators, their coupling $J = \frac{\omega_0}{2}(C_g/(C_0+C_g))$ is positive-valued [13] due to the fact that the anti-symmetric odd mode of the circuit is the lower energy eigenmode. This results in positive-valued photon hopping terms in the Hamiltonian, which directly lead to a maximum in frequency at the Γ point and opposite directions of the phase velocity and group velocity in the structure, as observed in other dispersive media [109–111].

Comparison to Tight-Binding Model

In the limit $C_0 \gg C_g$, the dispersion is well approximated to first order by a tight-binding model with dispersion given by $\omega_k = \omega_p + 2J\cos(kd)$, where $J = \omega_0(C_g/2C_0)$ is approximately the nearest-neighbor coupling between two resonators of the resonator array, and $\omega_p = (\omega_0 - 2J)$ is the center of the passband. The difference in the two dispersion relations reflects the coupling beyond nearest-neighbor that arises due to the topology of the circuit, in which any two pairs of resonators are electrically connected through some capacitance network dependent on their distance. The magnitude of these interactions is captured in the Fourier transform of the dispersion. Consider the Fourier transform for the annihilation operator of the (localized) mode of the individual resonator located at position x,

$$\hat{a}_k = \frac{1}{\sqrt{M}}\sum_x \hat{a}_x e^{-ikxd}. \tag{4.9}$$

Substituting Eq. (4.9) into Eq. (4.8), we arrive at the following real-space Hamiltonian,

$$\hat{H} = \hbar \sum_x \sum_{x'} V(x - x') \hat{a}_x^\dagger \hat{a}_{x'}, \tag{4.10}$$

where $V(x-x')$ is the distance-dependent interaction strength between two resonators located at positions x and x', and is simply given by the Fourier transform of the dispersion relation,

$$V(x - x') = \frac{1}{M} \sum_k \omega_k e^{-ikd(x-x')}. \tag{4.11}$$

For example, substituting the tight-binding dispersion $\omega_k = \omega_p + 2J\cos(kd)$ into Eq. (4.11) yields $V(x - x') = \omega_p \delta_{x,x'} + 2J\left(\delta_{x-x',1} + \delta_{x-x',-1}\right)$, which, upon substitution into Eq. (4.10), recovers the tight-binding Hamiltonian with only nearest-neighbor coupling.

In Fig. 4.2a, we plot the magnitudes of nearest neighbor ($x - x' = 1$), next-nearest neighbor ($x - x' = 2$), and next-next-nearest neighbor ($x - x' = 3$) couplings in the capacitively coupled resonator array as a function of C_g/C_0 calculated numerically via the discrete Fourier transform of the dispersion relation. It is evident that for small C_g/C_0 the nearest neighbor coupling overwhelmingly dominates.

Qubit Coupled to Passband of a Waveguide

The Hamiltonian of a transmon-like qubit coupled to the metamaterial waveguide via a single unit cell, where only the first two levels of the transmon ($|g\rangle, |e\rangle$) are considered, can be written as ($\hbar = 1, d = 1$),

$$\hat{H} = \omega_{ge} |e\rangle \langle e| + \sum_k \omega_k \hat{a}_k^\dagger \hat{a}_k + \frac{g_{\text{uc}}}{\sqrt{M}} \sum_k \left(\hat{a}_k^\dagger \hat{\sigma}^- + \hat{a}_k \hat{\sigma}^+\right), \tag{4.12}$$

where ω_k is given by Eq. (4.7). For an infinite array, the time-independent Schrodinger equation $\hat{H}|\psi\rangle = E|\psi\rangle$ has two types of solutions in the single photon manifold: there are scattering eigenstates, which have an energy within the passband, and there are bound states that are energetically separated from the passband continuum. We demonstrate this in the following analysis. First, we substitute into $\hat{H}|\psi\rangle = E|\psi\rangle$ the following ansatz for the quantum states of the composite qubit-waveguide system, i.e. for dressed states of the qubit,

$$|\psi\rangle = c_e |e, \text{vac}\rangle + \sum_k c_k \hat{a}_k^\dagger |g, \text{vac}\rangle, \tag{4.13}$$

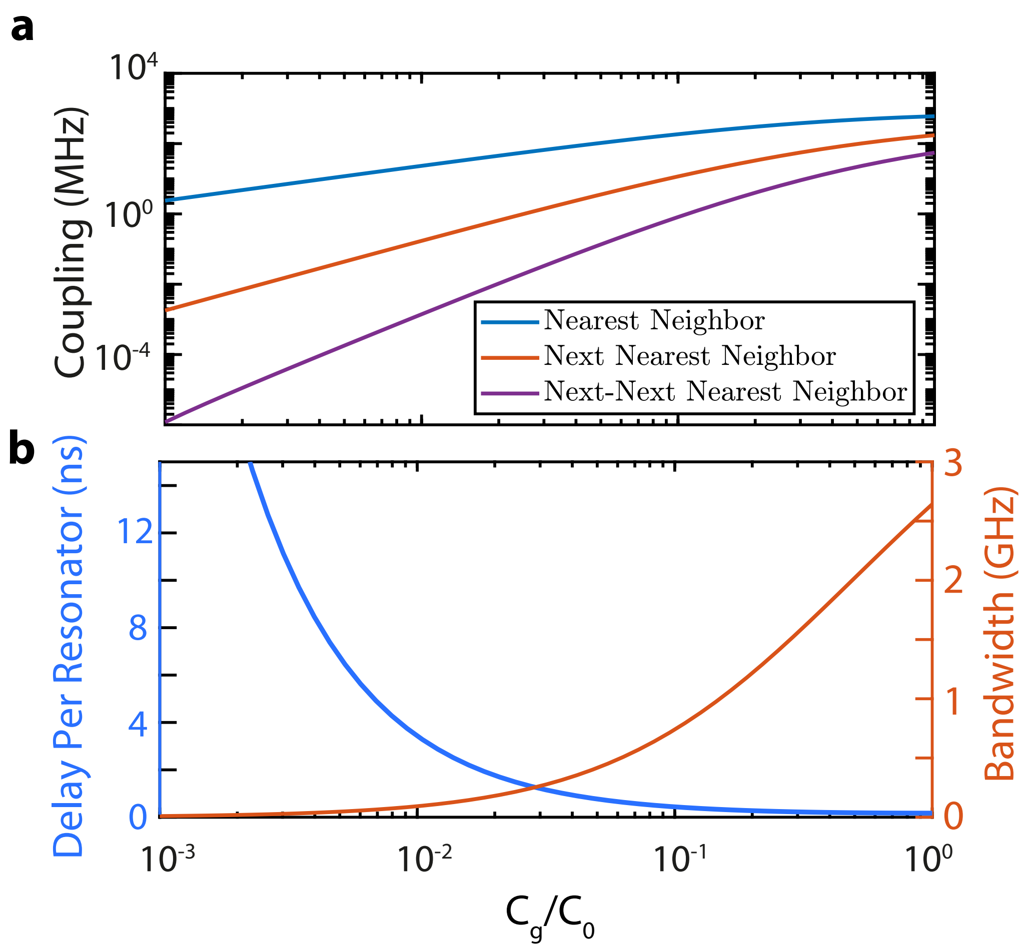

Figure 4.2: **Comparison to tight-binding model and bandwidth-delay trade-off for capacitively coupled resonator array a**. Magnitude of nearest neighbor, next-nearest neighbor, and next-next nearest neighbor inter-resonator couplings in an (infinite) capacitively coupled resonator array as a function of C_g/C_0 ratio. The bare resonator frequency was chosen to be 4.8GHz. **b.** Magnitude of delay per resonator and bandwidth of the passband as a function of C_g/C_0 ratio. The bare resonator frequency was again chosen to be 4.8GHz, and the calculated delays are for frequencies in the middle of the passband.

where $|\mathrm{vac}\rangle$ corresponds to no excitations in the waveguide. Doing this substitution and subsequently collecting terms, we arrive at the following coupled equations for c_e and c_k:

$$c_e = \frac{g_{\mathrm{uc}}}{\sqrt{M}} \sum_k \frac{c_k}{E - \omega_{ge}}, \tag{4.14}$$

$$c_k = \frac{g_{\mathrm{uc}}}{\sqrt{M}} \frac{c_e}{E - \omega_k}. \tag{4.15}$$

By further assuming that the waveguide supports a continuum of modes (which is appropriate for a finite tapered waveguide, as described in the main text), the sum can be changed into an integral $\sum_k \to \frac{1}{\Delta_k}\sum_k \Delta_k \to \frac{1}{\Delta_k}\int_{-\pi}^{\pi} \mathrm{d}k$, where $\Delta_k = 2\pi/M$. In this continuum limit, E can be found by first substituting Eq. (4.15) into Eq. (4.14) and subsequently dividing both sides by c_e, which yields the following transcendental equation for E,

$$E = \omega_{ge} + \frac{1}{2\pi}\int \mathrm{d}k \frac{g_{\mathrm{uc}}^2}{E - \omega_k}, \tag{4.16}$$

where the integral on the right-hand side of Eq. (4.16) is known as the "self-energy" of the qubit [22, 24, 25]. Note that in the opposite limit of a single resonator (where ω_k takes on a single value and the density of states $\frac{\partial\omega}{\partial k}$ becomes a delta–function at that value), Eq. (4.16) yields the familiar Jaynes-Cummings splitting $\sqrt{\delta^2 + g_{\mathrm{uc}}^2}$.

Computation of the self-energy for E such that $E > \omega_k$ or $E < \omega_k \;\; \forall k$, i.e. for energies outside of the passband, yields real solutions for Eq. (4.16). On the other hand, for energies E inside the passband, the self-energy integral contains a divergence at $E = \omega_k$ for real E while there is no divergence if E is allowed to be complex with an imaginary component; thus Eq. (4.16) has complex solutions when $\mathrm{Re}(E)$ is inside the passband. While a Hermitian Hamiltonian such as the one in Eq. (4.12) by definition does not contain complex eigenvalues, it can be shown that the magnitude of the imaginary component of complex solutions of Eq. (4.16) gives the decay rate of an excited qubit for a qubit dressed state with energy in the passband. For further details, we suggest Refs. [19, 24, 25] to the reader. Thus, the existence of complex solutions of Eq. (4.16) reflect the fact that qubit dressed states with energy in the passband are radiative states that decay into the continuum, characteristic of open quantum systems coupled to a continuum of modes. In contrast, the dressed states with (real) energies outside of the passband do not decay, and are known as qubit-photon bound states in which the photonic component of the dressed state wavefunction remains bound to the qubit and is not lost into the continuum.

For further analytical progress, we consider only the upper bandedge, and make the effective-mass approximation. This approximation is tantamount to assuming that the dispersion is quadratic, such that $\omega_k \approx \omega_0 - Jk^2$, which is obtained in the limit of small C_g/C_0 (where ω_k is well approximated by the tight binding cosine dispersion) and small k (where $\cos(k)$ to second order is approximately $1 - k^2/2$). This approximation is appropriate when ω_{ge} is close to the upper bandedge, where the qubit is dominantly coupled to the Γ-point $k = 0$ modes close to the bandedge due to the van Hove singularity in the DOS, and when the lower bandedge is sufficiently detuned from the qubit. Complimentary analysis for the lower bandedge can also be done in the same manner. For a more detailed derivation, see Refs. [24, 112, 113].

Under the effective-mass approximation, the self-energy integral in Eq. (4.16) can be easily analyzed by taking the bounds of integration to infinity, and is calculated to be $g_{\mathrm{uc}}^2/2\sqrt{J(E-\omega_0)}$. For $\omega_{ge} = \omega_0$, Eq. (4.16) then has the following two solutions:

$$E_b = \omega_0 + (g_{\mathrm{uc}}^4/4J)^{1/3}, \tag{4.17}$$

$$E_r = \omega_0 - e^{i\pi/3}(g_{\mathrm{uc}}^4/4J)^{1/3}. \tag{4.18}$$

These two solutions are indicative of a splitting of the qubit transition frequency by the bandedge into two dressed states: a radiative state with energy E_r in the passband and a bound state with energy E_b above the bandedge. The magnitude difference between the dressed state energies is $2(g_{\mathrm{uc}}^4/4J)^{1/3}$, which is the frequency of coherent qubit-to-photon oscillations for an excited qubit at the photonic bandedge.

For the remainder of the analysis, we focus on the qubit-photon bound state of the system. The wavefunction of the bound state with energy E can be obtained by first substituting Eq. (4.15) into Eq. (4.13), which yields

$$|\psi_E\rangle = c_e\left(|e\rangle + \frac{g_{\mathrm{uc}}}{\sqrt{M}}\sum_k \frac{1}{E-\omega_k}\hat{a}_k^\dagger\,|g,\mathrm{vac}\rangle\right). \tag{4.19}$$

The qubit and photonic components of the bound state can be calculated from the normalization condition of $|\psi_E\rangle$,

$$|c_e|^2\left(1 + \frac{1}{2\pi}\int \mathrm{d}k\left|\frac{g_{\mathrm{uc}}}{E-\omega_k}\right|^2\right) = 1. \tag{4.20}$$

By assuming $E > \omega_0$, the integral in Eq. (4.20) is calculated to be equal to $g_{\mathrm{uc}}^2/4\sqrt{J(E-\omega_0)^3}$, which yields the following magnitude for the qubit component of the bound state,

$$|c_e|^2 = \left(1 + \frac{1}{2}\frac{E-\omega_{ge}}{E-\omega_0}\right)^{-1}, \tag{4.21}$$

whereas the photonic component is simply $\int \mathrm{d}k|c_k|^2 = 1 - |c_e|^2$. We can thus see that when $E \approx \omega_{ge} \neq \omega_0$, the qubit is negligibly hybridized with the passband modes and $|c_e|^2 \approx 1$. On the other hand, as $\omega_{ge} \to \omega_0$, we have $|c_e|^2 \to 2/3$, indicating that the bound-state photonic component contains half as much energy as the qubit component when the qubit is tuned to the bandedge.

We can also obtain the real-space shape of the photonic bound state by inserting Eq. (4.9) into Eq. (4.19), where for a continuum of modes in k-space, we arrive at the following photonic wavefunction,

$$\sum_x e^{-|x|/\lambda} \hat{a}_x^\dagger \left|g, \mathrm{vac}\right\rangle , \tag{4.22}$$

up to a normalization constant, where $\lambda = \sqrt{J/(E - \omega_0)}$ and the qubit is assumed to reside at $x = 0$. We thus find an exponentially localized photonic wavefunction for the bound state. The localization length λ increases as J increases, indicating that the bound state becomes more delocalized across multiple resonators as the strength of coupling between the resonators in the waveguide increases, whereas λ diverges as the $E \to \omega_0$, which is associated with full delocalization of the bound-state as its energy approaches the continuum of the passband.

Group Delay

Lowering the ratio C_g/C_0 effectively lowers the photon hopping rate J between resonators, and can thus be chosen to significantly decrease the group velocity of propagating modes of the structure, albeit at the cost of decreased bandwidth of the passband modes. The group delay per resonator may be obtained from the inverse of the group velocity $\frac{\partial \omega_k}{\partial k}$, while the bandwidth can be calculated to be equal to $\omega_0 \left(1 - 1/\sqrt{1 + 4C_g/C_0}\right)$; both are plotted in Fig. 4.2b. Note that although the group velocity approaches zero near the bandedge, a traveling pulse at the bandedge frequency would experience significant distortion due to the rapidly changing magnitude of the group velocity near the bandedge. At the center of the passband where the dispersion is nearly linear, however, it is possible to have propagation with minimal distortion.

Hence, in order to effectively use the coupled resonator array as a delay line, the coupling should be made sufficiently high such that the bandwidth of propagating modes (where the dispersion is also nearly linear) is sufficiently high, and the effect of resonator frequency disorder due to fabrication imperfections is tolerable. After the resonator coupling constraints have been met, the desired delay may be achieved with a suitable number of resonators. It is thus evident that the ability to fabricate resonators of sub-wavelength size with minimal frequency disorder is critical to the effectiveness of implementing a slow-light waveguide with a coupled resonator array.

An appropriate metric to compare the performance of the resonator array as a delay line against dispersionless waveguides is to consider the delay achieved per area rather than per length, in order to account for the transverse dimensions of the resonators. In addition, typical implementations of delay lines with CPW geometries commonly require a high degree of meandering in order to fit in a packaged device; thus the pitch and turn radius of the CPW meandered trace also must be taken into account when assessing delay achieved per area. However, by making certain simplifying assumptions about the resonators it is possible to gain intuition on how efficient the resonator array is in achieving long delays compared to a dispersionless CPW. For the resonators implemented in the Main text (see Fig. 2.1), the capacitive elements of the resonator are electrically connected to one end of the meander while the opposite end of the meander is shunted to ground. This geometry is therefore topologically similar to a $\lambda/4$ resonator, and consequently the lengths of the meander and a conventional $\lambda/4$ CPW resonator will be similar to within an order of magnitude for conventional implementations (here λ is the wavelength of the CPW resonator mode).

Thus, by approximating that a single resonator of the array occupies the same area as a $\lambda/4$-section of CPW, a direct comparison between the delays of the two different waveguides can be made. In the tight-binding limit, the group delay per resonator in the middle of the passband is approximately equal to $1/2J$, where J is the coupling between two resonators of the array. Hence, for N resonators, $\tau_{\mathrm{d}}^{\mathrm{array}}/\tau_{\mathrm{d}}^{\mathrm{CPW}} = \frac{N/2J}{N\lambda/4v} \sim \omega_0/J$, where τ_d is group delay and v is the group velocity of light in the CPW. Hence, the resonator array is more efficient as a delay line when compared to conventional CPW by a factor of approximately ω_0/J (assuming group velocity is approximately equal to phase velocity in the CPW). In practice, this factor will also depend on the particular geometrical implementations of both kinds of waveguide. For example, for the resonator array described in Fig. 2.1, $\omega_0/J \approx 120$ and $\tau_{\mathrm{d}} = 55$ ns delay was achieved in the middle of the passband for a resonator array of area $A = 6\ \mathrm{mm}^2$. This constitutes a factor of 60 (500) improvement in delay per area achieved over the CPW delay line in Ref. [66] (Ref. [114]).

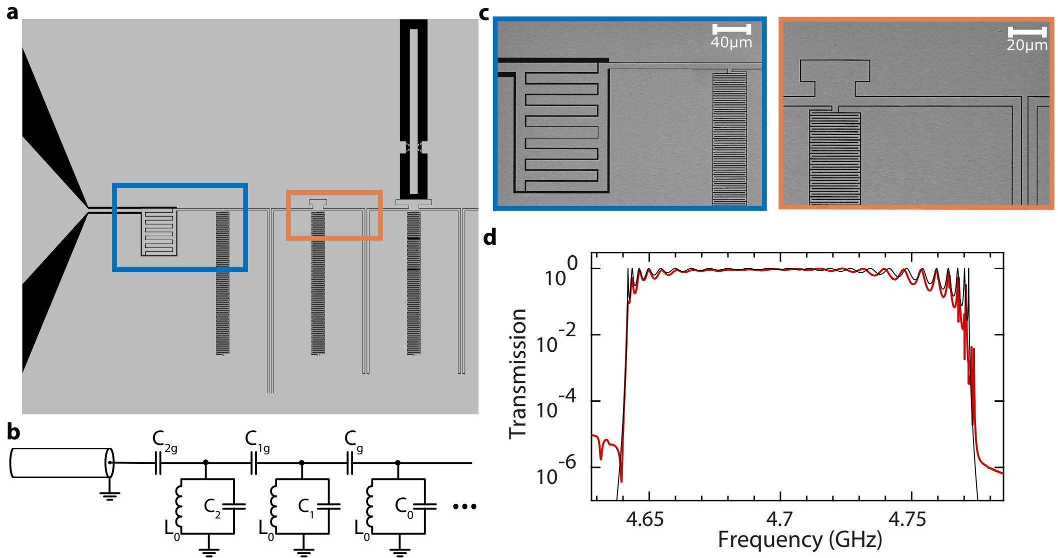

Figure 4.3: **CAD layout of boundary resonators and transmission spectrum of a resonator array with impedance matching. a.** CAD diagram showing the end of the finite resonator array, including the boundary matching circuit (which in this case includes the first two resonators) and the first unit cell. **b.** Corresponding circuit model of the end of the finite resonator array. **c.** Zoomed-in SEM images of the first (left) and second (right) boundary-matching resonators. **d.** Transmission spectrum of the full resonator array consisting of 22 unit cells and 2 boundary-matching resonators on either end of the array (for a total of 26 resonators). Measured data is plotted as a red curve and the circuit model fit is plotted as a black curve. Fit model parameters are given in the text.

4.3 Physical Implementation of Finite Resonator Array

Geometrical Design of Unit Cell

As shown in Fig. 2.1, the unit cell of the resonator array in this work includes a lumped-element resonator formed from a tightly meandered wire with a large 'head' capacitance, and 'wing' capacitors which, in addition to providing the majority of the capacitance to ground, are used to couple between resonators in neighbouring unit cells. The meandered wire has a 1 μm pitch and a 1 μm trace width for tight packing. At the top of the meander inductor is the 'head' capacitor and a pair of thin metal capacitor strips which extend to the lateral edges of the unit cell (the 'wing' capacitors). The ground plane in between the resonators' meander inductor and the lateral wing capacitors acts as an electrical 'fence', restricting the meander from coupling to neighboring resonators via stray capacitance or mutual inductance. This ensured that the bulk of the coupling between resonators was from the resonators' wing capacitive elements, thereby facilitating theoretical analysis of the structure using a simple single resonator per unit cell model. Furthermore, we included ground metal between the thin metal capacitor traces of neighbouring unit cell wing capacitors. In this way, the ground planes above and below the resonator array are tied together at each unit cell boundary, thereby suppressing the influence of higher-order transverse, slot-line modes of the waveguide.

In addition, anticipating integration with Xmon qubits, we incorporated into our unit cell design a Xmon shunting capacitance to ground, along with pads for facile addition of Josephson Junctions. This ensured that the addition of a qubit at a particular unit cell site in the resonator array minimally affected the capacitive environment surrounding that unit cell, and prevented the breaking of translational symmetry of the resonator array due to the addition of qubits. The capacitance between the Xmon capacitor and the rest of the unit cell was designed to be ~ 2 fF, yielding a qubit-unit cell coupling of $g_{\mathrm{uc}} \approx 0.8J$.

Matching of the Finite Resonator Array to Input-Output CPWs

It has been previously shown that for a finite coupled cavity array, low-ripple transmission at the center of the passband is possible by appropriate variation of the inter-resonator coupling coefficients for a few of the resonators adjacent to the ports, effectively matching the finite periodic structure to the input-output ports [115]. In the case of capacitively coupled electrical resonators, modifying the coupling capacitance in isolation results in a renormalization of the resonance frequency and thus constitutes a scattering center for propagating light. Thus, concurrent modification of both the coupling capacitance and the shunt capacitance to ground for the boundary resonators is necessary to achieve low-ripple transmission in the middle of the passband, as previously shown in filter design theory [116]. By constraining the total capacitance in each modified resonator to remain constant (and keeping the inductance constant), the total number of parameters to adjust in order to achieve low ripple transmission is merely equal to the chosen number of resonators to be modified, resulting in a low-dimensional optimization problem. A filter design software such as Microwave Office can be used to provide initial guesses on the optimal circuit parameters with high accuracy, which can then be further optimized.

In the Main text we present results on impedance matching of a resonator array spanning 26 resonators to 50-Ω CPWs via modification of two resonators at each of the array-CPW boundaries. The geometrical designs of the boundary resonators are shown in Fig. 4.3. The number of boundary resonators to modify (2) was chosen as a compromise between device simplicity and spectral bandwidth over which matching occurs. In principle, however, more resonators could have been used for matching of the finite structure to the ports in order to decrease the ripples in the transmission passband near the bandedges. Referring to the notation in Fig. 4.3b, the targets for the unit cell resonator and boundary resonator elements extracted from Sonnet [117] electromagnetic simulations were C_{2g} = 89 fF, C_{1g} = 8.9 fF, C_g = 6.47 fF, C_2 = 269 fF, C_1 = 351 fF, C_0 = 353 fF, and geometric inductance L_0 = 2.92 nH. The individual capacitive and inductive elements have parasitic inductance and capacitance, respectively, and thus were not simulated separately. Rather, circuit parameters for the three different resonators were extracted by simulating the whole resonator circuit. We extracted the circuit element parameters from these simulations by numerically obtaining the dispersion for an infinite array of each of the three types of resonators via the ABCD matrix method [77]. This yielded ω_0 and C_g/C_0; C_g was obtained from the B parameter of the $ABCD$ matrix (which contains information on the series impedance of the unit cell circuit). We found this method of extracting parameters from simulation to give much higher accuracy when compared to other approaches, such as simulating unit cell elements separately.

Figure 4.3d shows a plot of the measured transmission spectrum of the fabricated 26 unit cell slow-light waveguide based upon the above design and presented in the Main text (c.f., Fig. 2.1). A circuit model fit to the measured transmission spectrum yields the following circuit element parameters for boundary and central waveguide unit cells: C_{2g} = 87.5 fF, C_{1g} = 7.3 fF, C_g = 5.05 fF, C_1 = 352.1 fF, C_2 = 275.5 fF, C_0 = 353.2 fF, and geometric inductance L_0 = 3.151nH. Based upon this model fit, we were thus able to realize good correspondence (within 3%) between design and measured capacitances to ground, while extracted coupling capacitances are systematically lower by approximately 1.5 fF. We attribute the systematically smaller coupling to stray mutual inductance between neighboring meander inductors, which tends to lower the effective coupling impedance between the resonators. The slightly larger fit inductance compared to the design is to be expected as the kinetic inductance of the meander trace was not included in simulation. According to Ref. [118], for a 1 μm trace width and 120 nm thick aluminum wire, the expected increase in the total inductance due to kinetic inductance is approximately 5% of the geometric inductance, in reasonable correspondence to the measured value.

4.4 Disorder Analysis

Fluctuations in the bare resonance frequencies of the lumped-element resonators making up the metamaterial waveguide breaks the translational symmetry of the waveguide, and effectively leads to random scattering of traveling waves between different Bloch modes. This scattering results in an exponential reduction in the probability that a propagating photon traverses across the entire length of the waveguide. Furthermore, if the strength of scattering is large relative to the photon hopping rate, Anderson localization of light occurs where photons are completely trapped within the waveguide [76]. Thus, the aforementioned strategy for constructing a slow-light waveguide from an array of weakly coupled resonators is at odds with the inherit presence of fabrication disorder in any practically realizable device. Therefore, a compromise must be struck between choosing an inter-resonator coupling low enough to provide significant delay, but high enough such that propagation through the metamaterial waveguide is not significantly compromised by resonator frequency disorder.

Fig. 4.4a shows numerical calculations of the transmission extinction in the metamaterial waveguide as a function of σ/J, where σ is the resonator frequency disorder. This analysis was performed for a 50 unit cell waveguide, with $C_0 = 353.2$ fF, $C_g = 5.05$ fF, and $L_i = 3.101$ nH $+ \delta_i$. Here, L_i is the inductance of the i^{th} unit cell and δ_i are random inductance variations in each unit cell that give rise to a particular resonator frequency disorder, σ. These L_i were calculated by: (i) determining the resonator frequencies of each unit cell by drawing from a Gaussian distribution with mean ω_0 and variance σ^2, and (ii) solving for the corresponding inductances given the resonator frequencies and a fixed C_0. Note that we modeled the disorder as originating from inductance variations, rather than C_0 or C_g variations, based on the fact that earlier work showed that disorder in superconducting microwave resonators was primarily due to variations in kinetic inductance [119]. As we see in Fig. 4.4a, in order for the average transmission to drop by less than 0.5dB (10%), the normalized resonator frequency disorder must be less than $\sigma/J < 0.1$.

In order to quantify the resonator frequency disorder in our fabricated resonator array, one can analyze the passband ripple in transmission measurements [119] (c.f., Fig. 2.1d,e). Given that the effect of tapering the circuit parameters at the boundary is to optimally couple the normal modes of the structure to the source and load impedances, the ripples in the passband are merely overlapping low-Q resonances of the normal modes. Therefore, we can extract the normal mode frequencies from the maxima of the ripples in the passband, which will be shifted with respect the to normal mode frequencies of a structure without disorder.

Furthermore, the mode spacing is dependent on the number of resonators and, in the absence of disorder, follows the dispersion relation shown in Fig. 2.1c where the dispersion is relatively constant near the passband center and starts to shrink

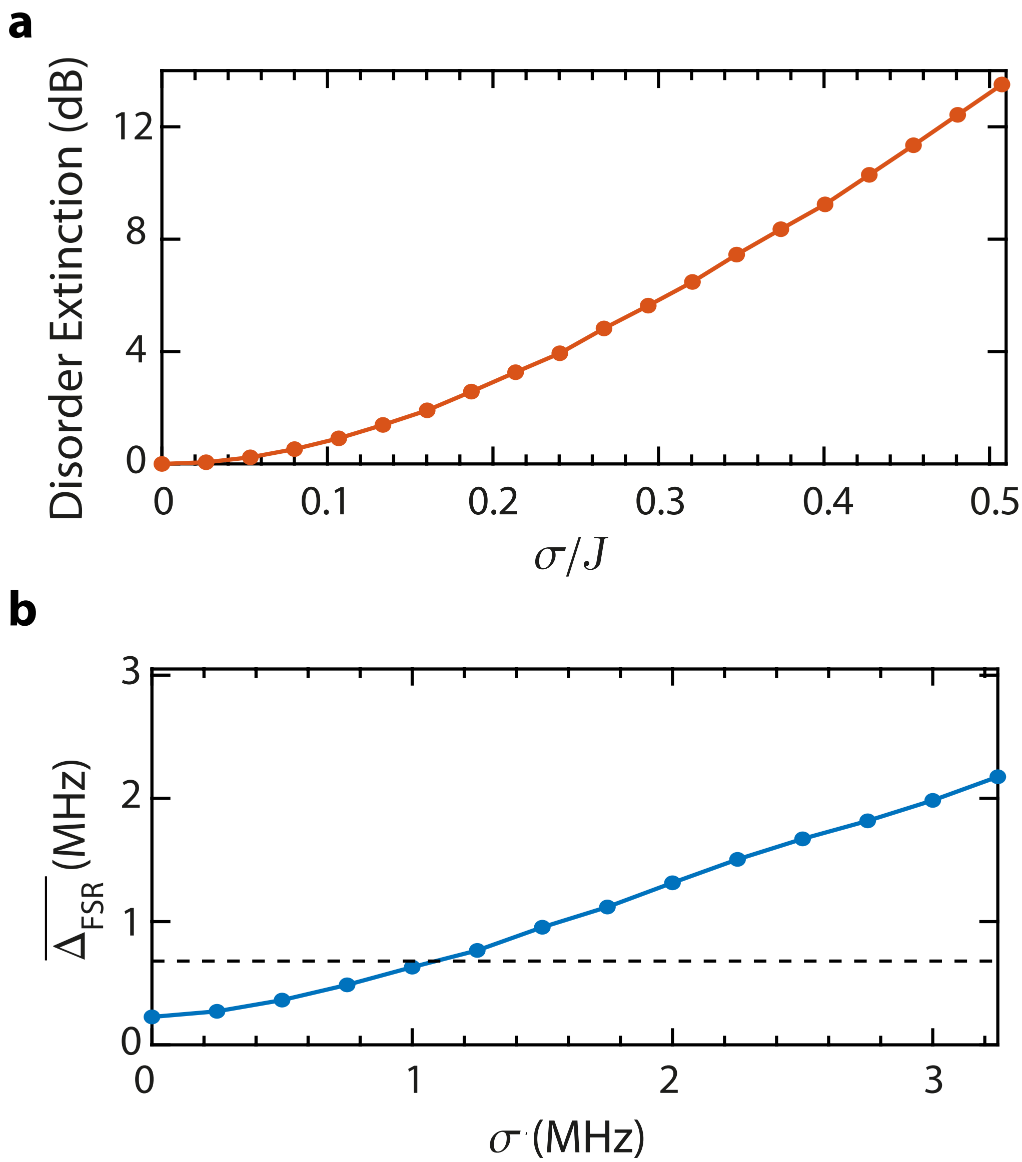

Figure 4.4: **Disorder analysis of capacitively coupled resonator array. a.** Numerically calculated extinction as a function of disorder. Here, σ is the disorder in the bare frequencies of the (unit cell) resonators making up the metamaterial waveguide and J is the coupling between nearest-neighbour resonators in the resonator array. 50 unit cells were used in this calculation, which included taper-matching sections at the input and output of the array that brought the overall passband ripple to 0.01dB. For a given disorder strength, σ, disorder extinction was calculated by taking the mean of the transmission across the passband for a given disorder realization, and subsequently averaging that mean transmission over many disorder realizations. Note that the calculated values depend on the number of unit cells. **b.** Numerically calculated variance in normal mode frequency spacing as a function of disorder. See text for details on the method of calculation of $\overline{\Delta_{\mathrm{FSR}}}$. Dashed line indicates the experimentally measured Δ_{FSR}, which was extracted from the data shown in Fig. 2.1d.

near the bandedges. In the presense of disorder, however, this pattern breaks down as the modes become randomly shifted. Our approach was therefore as follows. Starting with the fit parameters presented in Appendix 4.3, we simulated transmission through the metamaterial waveguide for varying amounts of resonator frequency disorder, σ. For each level of disorder, we performed simulations of 500 different disorder realizations, and for each different disorder realization, we computed the standard deviation in the free spectral range of the ripples, Δ_{FSR}. This deviation in free spectral range was then averaged over all disorder realizations for each value of σ, yielding an empirical relation between $\overline{\Delta_{\mathrm{FSR}}}$ and σ.

The numerically calculated empirical relation between variation in free spectral range and frequency disorder is plotted in Fig. 4.4b. Note that the minimum of $\overline{\Delta_{\mathrm{FSR}}}$ at $\sigma = 0$ is set by the intrinsic dispersion of the normal mode frequencies of the unperturbed resonator array. As such, in order to yield a better sensitivity to disorder, we chose to only use the center half of the passband in our analysis where dispersion is small. From the data in Fig. 2.1d, we calculated the experimental Δ_{FSR}. Comparing to the simulated plot of Fig. 4.4b, this level of variance in the free spectral range results from a resonator frequency disorder within the array at the 1 MHz level (or 2×10^{-4} of the average resonator frequency), corresponding to $\sigma/J \approx 1/30$. We have extracted similar disorder values across a number of different metamaterial waveguide devices realized using our fabrication process.

4.5 Modeling of Qubit Q_1 Coupled to the Metamaterial Waveguide

In this section, we present modeling of the interaction between Q_1 and the metamaterial waveguide. Note that, while we observe dynamics that are due to emission and propagation of single-photon radiation field states, which are non-classical states of light, in the single-excitation limit the dynamics of the qubit can also be described by a classical circuit model, where the qubit is represented by a faux resonator. Thus, here we share both viewpoints of analysis, and we employ two separate models to represent our system: a tight-binding model with nearest and next-nearest neighbor coupling which we analyze via a numerical master equation solver, and a classical circuit model (shown in Fig. 4.6). We find excellent agreement between the two models.

Tight-Binding Model

System Hamiltonian and Model Formalism

For transient time-domain simulations, instead of using the Hamiltonian presented in equation 4.12, we instead employ the following tight-binding model (with individual resonator positions denoted by the indices x and i)

$$\begin{aligned}\hat{H} = \omega_{ge} \left|e\right\rangle \left\langle e\right| + \sum_{x=1}^{M} \omega_x \hat{a}_x^\dagger \hat{a}_x + (J_x \hat{a}_x^\dagger \hat{a}_{x+1} + J_{nnn} \hat{a}_x^\dagger \hat{a}_{x+2} \\ + h.c) + \sum_{i=1,3,4} g_i \hat{\sigma}_x \left(\hat{a}_i^\dagger + \hat{a}_i\right),\end{aligned} \tag{4.23}$$

where M is the number of resonators, ω_x are the frequencies of the individual resonator modes, and, as discussed in section 4.2, in our parameter regime the capacitively coupled resonator array Hamiltonian can be well approximated as a tight-binding Hamiltonian with dominant nearest-neighbor coupling J_x and small ($\sim J/100$) next-nearest neighbor coupling J_{nnn} (which we keep as a constant in the model for simplicity). In our model, for all unit cells, we set $\omega_x = \omega_p = \omega_0 - 2J$, which is the passband center frequency and constitutes the bare resonator frequency ω_0 renormalized by its coupling to neighboring resonators; however, for the taper resonators, we introduce moderate detunings in order to capture the weak reflections within the slow-light waveguide evidenced by the measured data (see Fig. 2.3). Further, we include qubit coupling to multiple resonators in the array in our model with couplings g_i, where i indicates resonator position in the array, in order to capture both g_{uc} and the weak non-local coupling of the qubit to a few of the neighboring unit cells that was evidenced by the measured data.

Going into the rotating frame of the passband center frequency ω_p and applying the rotating wave approximation (RWA) to remove counter-rotating terms, we arrive at the following Hamiltonian

$$\begin{aligned}\hat{H} = \Delta_{ge} \left|e\right\rangle \left\langle e\right| + \sum_{x=1}^{M} \delta_x \hat{a}_x^\dagger \hat{a}_x + (J_x \hat{a}_x^\dagger \hat{a}_{x+1} + J_{nnn} \hat{a}_x^\dagger \hat{a}_{x+2} \\ + h.c) + \sum_{i=1,3,4} g_i \left(\hat{a}_i^\dagger \hat{\sigma}^- + \hat{a}_i \hat{\sigma}^+\right),\end{aligned} \tag{4.24}$$

where $\Delta_{ge} = \omega_{ge} - \omega_p$ and $\delta_x = \omega_x - \omega_p$; see Fig. 4.5a for a visual diagram of the model. It can be shown that the Hamiltonian in equation 4.24 preserves the number of

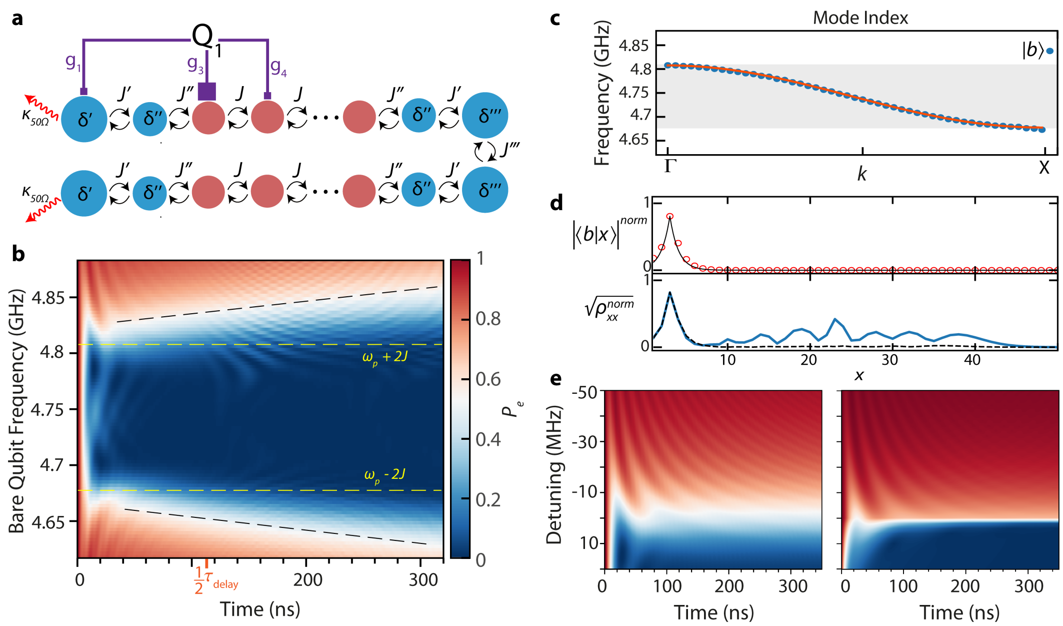

Figure 4.5: **Master equation numerical simulations of our qubit-slowlight waveguide system.** **a.** Diagram of tight-binding model used in simulations. Simulation parameters are described in the text. Note that the next-nearest neighbor coupling J_{nnn}, which is present in the model for all resonators, is omitted from the diagram for readability purposes. **b.** Simulation of Fig. 2.3b dataset. Bandedges are highlighted in dashed yellow lines, while dashed black lines are guides to the eye. **c.** Scatter plot of the eigenenergies of the Hamiltonian in equation 4.24 with $\Delta_{ge}/(2\pi) = 83$ MHz (in the single excitation manifold) offset by ω_p. The orange curve is a plot of the dispersion relation (see equation 4.7). The eigenmode with energy outside of the passband corresponds to the bound state of the system $|b\rangle$ **d.** Plot of photonic states of the system as a function of position x. Top panel: plot of the photonic wavefunction of the bound eigenstate of the system $|b\rangle$ in open red dots; "*norm*" indicates that the photonic wavefunction coefficients $\langle x|b\rangle$ are normalized by $\sqrt{\sum_x |\langle x|b\rangle|^2}$, where $|x\rangle$ corresponds to the state $|0_1, 0_2, \ldots, 1_x, \ldots, 0_M; g\rangle$. The solid black line corresponds to a plot of $Ae^{|x-3|/\lambda}$, where $\lambda = \sqrt{J/(E_b - \omega_0)}$ and A is a normalization constant. Bottom panel: plot of the photonic portion of the simulated qubit-waveguide state after $t = 90$ ns. The solid blue line corresponds to a simulation with initial state $|0_1, 0_2, \ldots, 0_M; e\rangle$; the dashed black line corresponds to a simulation with initial state $|b\rangle$. ρ_{xx}^{norm} refers to the scaled density matrix element $\rho_{xx}/\left(\sum_{x=1}^{10} \rho_{xx}\right)$. This particular scaling is chosen because it similarly scales the photonic part of the state within the first 10 resonators of the array, thereby aiding visual comparison between the blue and dashed black curves. **e.** Comparison of the dynamics simulated by a modified tight-binding model of a qubit coupled to a metamaterial waveguide (left), and by population equations of motion derived in Ref. [22] (right). Refer to (**b**) for colorbar. Both models assume $g_{\mathrm{uc}}/2\pi = 19$ MHz, as well as $J/2\pi = 33$ MHz. See text for description of modified model. We use $(g_{\mathrm{uc}}^4/4J)^{1/3}$ in place of β for simulations using equations 2.21-2.28 from Ref. [22].

excitations N by noting that the commutator $\left[\hat{H}, \hat{N}\right] = 0$ with $\hat{N} = \sum_{x=1}^{M} \hat{a}_x^\dagger \hat{a}_x + \hat{\sigma}^+\hat{\sigma}^-$. Consequently, the dynamics of the system can be partitioned into subspaces with fixed excitation number, and for the purposes of modeling the data in Fig. 2.3 of a qubit's radiative dynamics in a structured photonic reservoir, we only need to consider the subspaces of $N = 0, 1$. The Hamiltonian in this reduced subspace can be computed by explicitly evaluating the matrix elements $\langle\phi|\,\hat{H}\,|\phi'\rangle$ between different states $\{|\phi\rangle\}$ in the zero and single excitation manifold, and subsequently directly used in numerical master equation simulations. Finally, while the Hamiltonian in equation 4.24 generates the unitary dynamics of the system, the external loading of the system to the input/output 50-Ω waveguides is incorporated into the model via dissipation with rate $\kappa_{50\Omega}$ in the first and last resonators of the array, which is generated in our master equation simulations via collapse operators which transfer population from the single excitation states $|1_1, 0_2, 0_3, \ldots, 0_M; g\rangle$ and $|0_1, 0_2, 0_3, \ldots, 1_M; g\rangle$ to the (trivial) zero-excitation ground state of the system $|0_1, 0_2, 0_3, ..., 0_M, g\rangle$. Note that master equation simulations of the qubit's non-Markovian radiative dynamics are only possible here due to the fact that we are explicitly simulating all the photonic degrees of freedom of the slow-light waveguide in addition to the qubit's degrees of freedom. A Lindbladian master equation simulation of solely the qubit's degrees of freedom, with the photonic degrees of freedom traced out, would not capture its non-Markovian radiative dynamics. Moreover, a simulation of the entire qubit-waveguide system is only amenable here due to our restriction of the Hilbert space to its low-energy sector, and would quickly grow intractable if higher number of excitations were allowed.

Referring to equation 4.24 and Fig. 4.5a, our model assumed the following parameters (2π factors are omitted for readability): $M = 50$, $\delta_1 = \delta_{50} = \delta' = -13.9$ MHz, $\delta_2 = \delta_{24} = \delta_{27} = \delta_{49} = \delta'' - 4.7$ MHz, $\delta_{25} = \delta_{26} = \delta''' = 323$ MHz, $J_1 = J_{24} = J_{26} = J_{49} = J' = 44.1$ MHz, $J_2 = J_{23} = J_{27} = J_{48} = J'' = 32.47$ MHz, $J_{25} = J''' = 349$ MHz, $J_{nnn} = 0.3$ MHz, all other $J_x = J = 32.52$ MHz, all other $\delta_x = 0$, and $\kappa_{50\Omega} = 169.92$ MHz (note that the values of δ''' and J''' are very different from other values in order to accurately capture the circuit of the waveguide's bend section as discussed in the Main Text). Note that these parameters are consistent with the circuit parameters of the model shown in Fig. 4.6 that is later discussed. Furthermore, in the model we coupled the qubit to the first, third, and fourth resonators of the array (as opposed to just the third resonator), with couplings $g_1 = 2.2$ MHz, $g_2 = g_{\text{uc}} = 26.4$ MHz, $g_3 = 3.5$ MHz. Physically, the coupling to resonators 1 and 4 was not intentional and was due to parasitic capacitance. We set $g_2 = 0$ in the model because the second metamaterial resonator was not expected to parasitically couple to the qubit as strongly as the first and fourth resonator due to the absence of an interdigitated capacitor or an integrated Xmon shunting capacitance (see Fig. 4.3 for images of the second resonator of the metamaterial waveguide). The g_1 and g_4 parasitic couplings were crucial to reproduce some of the subtle features in the measured data; this will be discussed in detail below.

Dynamical Simulations and Eigenenergy Analysis

Fig. 4.5b shows the simulated dynamics from numerical master equation simulations as a function of Δ_{ge} (note that bare qubit frequency $\omega_p + \Delta_{ge}$ is shown in the plot instead for comparison purposes to Fig. 2.3) with initial state $|0_1, 0_2, \ldots, 0_M; e\rangle$. It is evident that there is agreement between Fig. 4.5b and the measured data in Fig. 2.3b, indicating that our model captures the salient dynamical features of our measured data. Furthermore, with the Hamiltonian in Equation 4.24, we can numerically calculate its eigenstates and the eigenenergy spectrum; as an example, the spectrum when $\Delta_{ge}/(2\pi) = 83$ MHz is plotted in Fig. 4.5c. Fig. 4.5c shows a band of states within the passband, and a state with energy outside of the passband. Because $M = 50$, the Hamiltonian is that of a finite-sized system and the band of states within the passband represent the normal modes of the finite waveguide structure; however, in the presence of input/output waveguides, they represent a band of scattering states that support wave propagation between the input/output waveguides. The state with energy outside of the band, however, is the bound eigenstate $|b\rangle$. We calculate bound state energies as a function of bare qubit frequency Δ_{ge}, and converting bare qubit frequency to the physically applied flux through the SQUID loop used to tune the qubit frequency Φ (via measured qubit minimum/maximum frequencies and the extracted anharmonicity), we numerically obtain the predicted energy of the system's bound eigenstates as a function of flux bias and plot it on Fig. 2.2d as dashed black lines. As Fig. 2.2d shows, we obtain good quantitative agreement between the prediction of our model and the spectroscopically measured bound state energies of the qubit-waveguide system.

In our model, the g_3 coupling primarily sets the coupling of the qubit to the metamaterial waveguide. Its magnitude relative to the J between the unit cells, along with the qubit frequency $\omega'_{ge}(\Phi)$, predominantly determines the frequency of oscillations near the bandedge, as well as the decay rate into the waveguide in the passband. In the absence of other parasitic couplings, this decay rate is theoretically determined to be $\sim g_{\mathrm{uc}}^2/v(\omega'_{ge}(\Phi))$ [112], where $v(\omega'_{ge}(\Phi))$ is the group velocity of the metamaterial waveguide at the qubit-waveguide interaction frequency $\omega'_{ge}(\Phi)$. The parasitic coupling g_4, however, is necessary to replicate the asymmetry in the dynamics near the upper and lower bandedges. This is because the lower bandedge modes have an oscillating charge distribution between unit cells, while the upper bandedge modes have a slowly-varying charge distribution across the unit cells (which is typical of 1D tight-binding systems). The parasitic coupling of the qubit to the neighboring unit cell therefore has the effect of lowering the qubit coupling to the lower bandedge modes due to cancellation-effects arising from the opposite charges on neighbouring resonators for lower bandedge modes. On the other hand, coupling of the qubit to the upper bandedge modes which have slowly-varying charge distributions, is enhanced.

In addition, in simulations, the onset of oscillations seen at $\tau \approx 115$ ns could be delayed or advanced by increasing or decreasing the number of resonators in between the qubit and the bend in the metamaterial waveguide model, while it could be removed altogether by removing the bend section. This indicated that these late time oscillations are a result of spurious reflection of the qubit's emission at the bend, due to the imperfect matching to the 50-Ω coplanar waveguide in between the two resonator rows (which is manifested in this model through parameters δ''' and J'''). Note that this impedance mismatch and reflections are amplified near the bandedges, where the Bloch impedance rapidly changes.

Photonic State Spatial Analysis

In the main text, the observed qubit emission dynamics into the slow-light waveguide are described in terms of the interplay of the qubit-waveguide dressed states; in particular, the bound and continuum dressed states of the qubit-waveguide system. Here we further elucidate this description of our system via our modeling, using as an illustrative example the dynamics of the system when the qubit is tuned 18 MHz above the upper bandedge ($\Delta_{ge}/(2\pi) = 83$ MHz), corresponding to the brown curve in Fig. 2.3c.

Firstly, in the main text, we assert that initializing the qubit in state $|e\rangle$ with its frequency in the proximity of the passband effectively initializes it into a superposition of bound and continuum dressed states. This can be explicitly verified by first numerically calculating the eigenstates and the eigenenergy spectrum of the Hamiltonian, as was done for Fig. 4.5c. As previously discussed, the state with energy outside of the band is the bound eigenstate $|b\rangle$, and the photonic component of its wavefunction is plotted in the top panel of Fig. 4.5d. It is evident from Fig. 4.5d that the photonic component of the bound state wavefuncion is localized around resonator 3, which is the unit cell that the qubit is predominantly coupled to. As discussed in section 4.2, the bound state is exponentially localized with localization length approximately $\lambda = \sqrt{J/(E_b - \omega_0)}$ where E_b is the energy of the bound state; this theoretical photonic wavefunction is plotted in the top panel of Fig. 4.5d with a solid black line, and shows good agreement with the numerically calculated $|b\rangle$ wavefunction plotted in red open dots. Numerically calculating the overlap between the $|0_1, 0_2, 0_3, ..., 0_M, e\rangle$ state and the bound eigenstate yields $|\langle b|0_1, 0_2, 0_3, ..., 0_M, e\rangle|^2 \approx 0.8$, agreeing well with equation 4.21.

Secondly, in the main text we also assert that the amplitude of the early-time oscillations quickly dampen away as the energy in the radiative continuum dressed state is quickly lost into the waveguide, while the energy in the bound state remains localized around the qubit, albeit slowly decaying (details of this slow decay are given in the next paragraph). In order to illustrate this point, in the bottom panel of Fig. 4.5d we plot the photonic portion of the system's state at time $t = 90$ ns, at which point the early-time oscillations have subsided and the qubit can be observed to be slowly decaying. It is evident that while part of the state is delocalized in the array, a significant portion is still localized around the qubit location; this portion corresponds to the bound state portion of the initial state $|0_1, 0_2, 0_3, ..., 0_M, e\rangle$ after time evolution.

Thirdly, in order to understand the slow decay of the qubit following the early-time oscillations, note that a non-negligible proportion of the bound state wavefunction is found on resonator 1, the taper resonator directly coupled to output waveguide, signifying finite overlap between the bound state and the external 50-Ω environment of the output waveguide. This overlap constitutes the dominant intrinsic loss channel for the bound state and leads to its slow decay, which in the $t \to \infty$ limit results in the full decay of qubit even if its frequency is tuned outside the passband. Near the bandedges, it is this loss that results in a slow population decay as compared to the initial fast dynamics in the data (see top panel of Fig. 2.3c for a clear example), and results in the feature highlighted by dashed black lines in Fig. 4.5b. This feature would be flat for an infinite-sized resonator array and there would be partial "population trapping" [25] of the qubit in the $t \to \infty$ limit if its bare frequency was detuned from the passband and there were no other intrinsic loss channels. Note that the g_1 coupling between the qubit and the resonator directly coupled to the 50-Ω port is necessary to quantitatively replicate the slow decay rates of the qubit when its frequency is outside of the passband. In the absence of the g_1 coupling, this overlap was not sufficiently high in the simulations given the coupling of the qubit to the metamaterial waveguide (extracted from separate measurements in the passband). Therefore, this overlap was made larger, while minimizing the increase to the overall coupling of the qubit to the metamaterial waveguide, by incorporating the small g_1 coupling to the first resonator of the array.

Finally, it can be observed in Fig. 2.3b and Fig. 4.5 that there are differences in both duration and amplitude between the early-time oscillations and the late-time oscillations that occur at $\tau \approx 115$ ns. This is because, when the qubit frequency is near the bandedges, the reflected emission is distorted through its propagation in the metamaterial waveguide due to the significant dispersion near the bandedges. This results in a spatio-temporal broadening of the emitted radiation, which is evident in the bottom panel of Fig. 4.5d. The frequencies of both sets of oscillations, however, are set by g_{uc} and J as discussed in the main text.

Comparison to Paradigmatic Model of Spontaneous Emission Near the Edge of a Photonic Bandgap

As alluded to in the main text, the early-time oscillations observed in our work are, qualitatively, a generic feature of the interaction between a qubit and a bandedge in a dispersive medium, and not merely an attribute of our specific system. In order to illustrate this point, in Fig. 4.5e, we further compared the initial oscillations to the theory presented by John and Quang in Ref. [22] of a qubit whose frequency lies in the spectral vicinity of a bandedge. The model assumed for Ref. [22] was that of an atom (qubit) with point dipole coupling to an infinite periodic dielectric environment, whose frequency is in the spectral vicinity of only a single bandedge. Thus, in order to make a comparison to this theory, we changed the model of our system described by equation 4.24 and Fig. 4.5a in the following manner: (i) we removed the parasitic couplings of the qubit to neighboring unit cells, in order to simplify the coupling to a single point coupling, (ii) we increased the size of the array and moved the qubit to the middle in order to remove boundary effects from the dynamics, (iii) we reduced the overall coupling of the qubit to the metamaterial waveguide so it predominantly couples to only the bandedge it is least detuned from. Note, however, that the dispersion relation of the waveguide is different than the dispersion assumed in Ref. [22]. Nonetheless, above the bandedge, we see good qualitative agreement between the dynamics modeled both by the modified model and the population equation of motion derived in Ref. [22] (in particular, equation 2.21), with both simulations exhibiting very similar oscillatory decay to what is observed in Fig. 4.5b and 2.3b. This further confirms our interpretation of the early-time non-Markovian dynamics in Fig. 2.3 discussed in the Main text: that the non-exponential oscillatory decay is due to the interaction between the qubit and the strong spike in the density of states at the bandedge.

Circuit Model

In addition to dynamical master equation simulations, we also performed modeling via classical circuit analysis, where the qubit is represented by a linear resonator; this is an accurate representation of the qubit-waveguide system in the single-excitation limit. Time-resolved dynamical simulations were performed with the LTSpice numerical circuit simulation package, while frequency response simulations were performed with Microwave Office and standard circuit analysis. Our model, shown in Fig. 4.6, assumes the following metamaterial waveguide parameters: C_{2g} = 92.5 fF, C_{1g} = 7.8 fF, C_g = 5.02 fF, C_2 = 273 fF, C_1 = 351.2 fF, C_0 = 353.2 fF, and L_0 = 3.099 nH, which were obtained from fitting the transmission through the metamaterial device shown in Fig. 2.2a with the qubit detuned away (600 MHz) from the upper bandedge. While in principle there are three independent parameters for every resonator (capacitance to ground, coupling capacitance, and inductance to ground), the set of metamaterial parameters above in addition to the qubit parameters were sufficient to achieve quantitative agreement between simulations and our data.

Our model utilizes a qubit capacitance (excluding the capacitance to the metamaterial waveguide) of C_Σ = 77.8 fF, which, when assuming $E_c \approx -\hbar\eta$, is consistent with measurements of the anharmonicity that was extracted by probing the two-photon transition between the $|g\rangle$ and $|f\rangle$ states. Furthermore, in the model we coupled the qubit to the first, third, and fourth resonators of the array, with capacitive couplings C_{1qg} = 0.16 fF, C_{3qg} = 1.9 fF, and C_{4qg} = 0.25 fF, while C_{2qg} = 0 fF, for reproducing both the dominant and the subtle features in the measured data due to the same reasons described in the preceding discussion.

Time Domain

Figure 4.6b shows the simulated dynamics of our circuit model as a function of bare qubit frequency (where the qubit inductance was swept to change the bare qubit frequency). It is evident that there is agreement between Fig. 4.6b and the measured data in Fig. 2.3b, indicating that our circuit model captures the salient dynamical features of our measured data. Moreover, we find excellent agreement between our circuit model and the tight-binding model presented in the preceding discussion, which was expected given that the parameters of the circuit model map nearly directly to the parameters of the tight-binding model. Thus, both models are

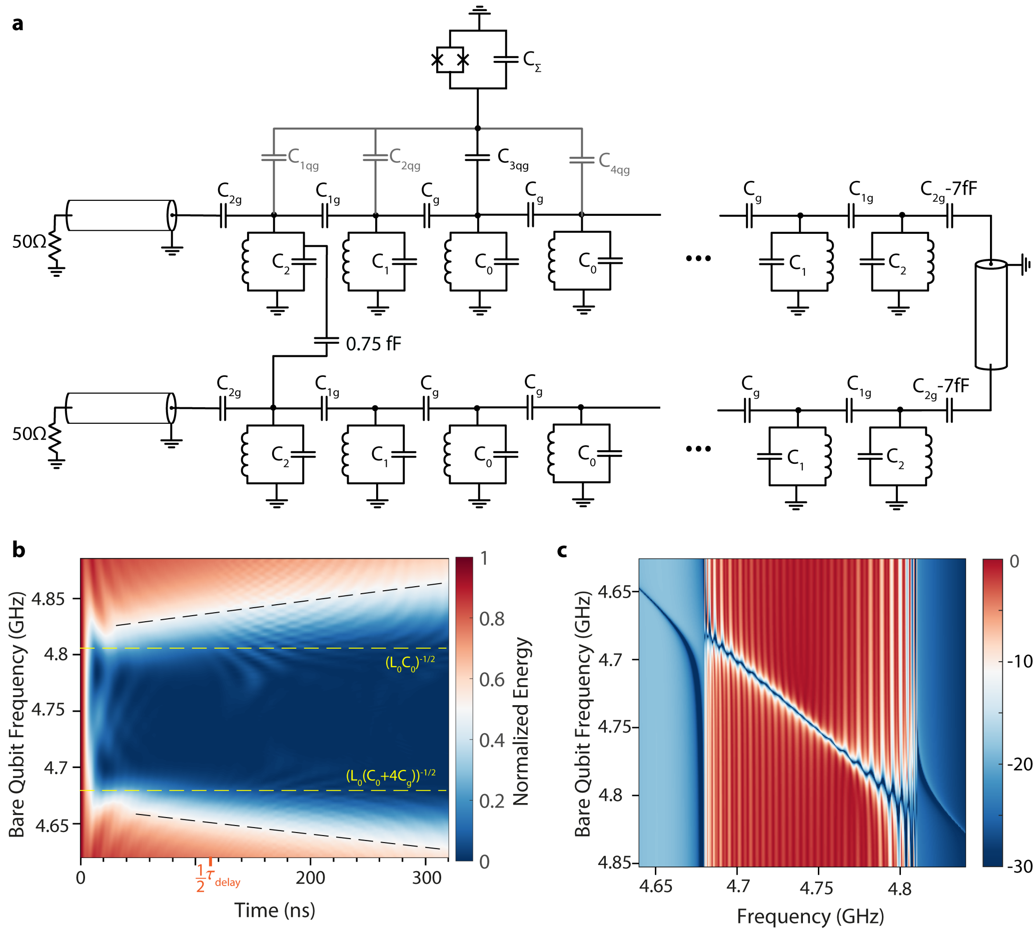

Figure 4.6: **Circuit model simulations of the qubit-slowlight waveguide system. a.** Full circuit model used in simulations. All inductors were made equivalent, with inductance L_0. Parameters are further discussed in the text. **b.** Simulation of Fig. 2.3b dataset. Intensity plot is of energy in the faux-qubit resonator normalized by the initial energy; this simulated time-dependent normalized energy corresponds directly to the qubit's excited state population measurements of Fig. 2.3b. Simulation parameters are described in the text. Bandedges are highlighted in dashed yellow lines, while dashed black lines are guides to the eye. **c.** Simulation of Fig. 2.2d dataset. Circuit model and simulation parameters are described in the text. Simulations were done with the aid of the Microwave Office software package.

appropriate for analyzing the data of Figure 2.3, and the insights into the system gained from the tight-binding model in the preceding discussion directly carry over to this circuit model.

Frequency Domain

In addition to time-domain simulations of our circuit model representing the fabricated qubit-waveguide system, in Fig. 4.6c we plot an intensity color plot of the transmission through the slow-light waveguide as the bare qubit frequency is tuned across the passband using the circuit model (c.f., the corresponding measurement data plotted in Fig. 2.2d). Note that in order to capture the background transmission levels as well as the interaction of the qubit with the background transmission, we included a small direct coupling capacitance of 0.75 fF between the first and last resonators of the array. These two resonators have the largest crosstalk. This is due to the large portion of charge contained in the interdigitated capacitors between the resonators and the input-output waveguides. In simulations without this background transmission, the qubit mode break-up near the bandedge and signatures of the bound-state outside of the passband were significantly weaker.

In addition, the series capacitance of the boundary resonators coupled to the input-output waveguides was made 7 fF higher than the series capacitance of the boundary resonators coupled to the short CPW section in the bend, which is due to the proximity of the large bondpads used to probe the waveguides. Our simulations are in excellent qualitative agreement with the data presented in Fig. 2.2d. They also capture the spectroscopic non-Markovian features of our data – the repulsion of the bound state's energy from the bandedge and the persistence of the bound state even when the bare qubit frequency overlaps with the passband (see Refs. [61, 62, 112] for further details).

4.6 Modeling of Qubit Coupled to Dispersion-less Waveguide in Front of Mirror

In this section, we present the modeling of the time-delayed feedback phenomenon described in the main text. Here, we employ a dispersion-less waveguide in our model instead of our slow-light waveguide in order to compare our data to the dynamics of an ideal scenario where pulse distortion and propagation losses are absent. We employ a dispersion-less waveguide with equivalent round-trip delay of $\tau_{\mathrm{d}} = 227$ ns to the slow-light waveguide. The theoretical model we use is described at length in Ref. [41]; below we briefly summarize the derivation of the model found in this reference.

Ref. [41] starts with the following Hamiltonian, where the coupling to different waveguide modes is now allowed to vary as a function of k,

$$\hat{H} = \omega_{ge} \left|e\right\rangle \left\langle e\right| + \int dk \omega_k \hat{a}_k^\dagger \hat{a}_k + \int dk g_k \left(\hat{a}_k^\dagger \hat{\sigma}^- + \hat{a}_k \hat{\sigma}^+\right), \tag{4.25}$$

and the same single-excitation ansatz of equation 4.13, but with time-dependent coefficients $c_e(t)$ and $c_k(t)$ (and where a continuum of modes is already assumed).

Following similar analysis to Appendix 4.2, equations 4.25 and 4.13 are substituted into the time-dependent Schrodinger equation $\partial_t |\psi(t)\rangle = -i\hat{H}|\psi(t)\rangle$, and after collecting terms and going into the rotating frame of the qubit, the authors arrive at the following system of coupled differential equations:

$$\dot{c_e}(t) = -i\int dk g_k c_k(t), \tag{4.26}$$

$$\dot{c_k}(t) = -i\Delta_k c_k(t) - i g_k c_e(t). \tag{4.27}$$

where $\Delta_k = \omega_{ge} - \omega_k$. The authors then explicitly integrate equation 4.27 to obtain a solution for $c_k(t)$, and substitute that solution into equation 4.26. In order to evaluate the resultant equation of motion for $c_e(t)$, the authors make the following assumptions: (i) they assume the dispersion is linearized around the qubit frequency such that $\omega_k = \omega_{ge} + v(k - k_0)$, where v is the group velocity, and (ii) $g_k = \sqrt{\Gamma_{1D} v/\pi}\sin kx_0$, where x_0 is the qubit position in the waveguide. The particular form of g_k is chosen by asserting that the field assumes a $\sin kx$ spatial profile such that the field fulfills the boundary condition of being zero at the waveguide termination; thus the field strength at the qubit is $\sin kx_0$. With these expressions for ω_k and g_k, the resultant equation of motion for $c_e(t)$ can be simplified to the following form

$$\dot{c_e}(t) = -\frac{\Gamma_{1D}}{2}c_e(t) + \frac{\Gamma_{1D}}{2}e^{i2k_0x_0}c_e(t-\tau_d)\theta(t-\tau_d) \tag{4.28}$$

where τ_d is the round-trip delay and θ is the heavyside step function; the first term on the right-hand side is responsible for the decay of the qubit, while the second term is responsible for photon re-absorption. Equation 4.28 is finally solved via methods described in Ref. [120], yielding the following analytic expression for the dynamics of a qubit excited state population when coupled to a semi-infinite dispersion-less waveguide:

$$c_e(t) = e^{\Gamma_{1D}t/2}\sum_n \frac{1}{n!}\left(\frac{\Gamma_{1D}}{2}e^{i\phi+\Gamma_{1D}\tau_d/2}\right)^n (t-n\tau_d)^n\theta(t-n\tau_d) \tag{4.29}$$

where $\phi = 2k_0x_0$ is the round-trip phase gained by the propagating emitted pulse.

Substituting $\Gamma_{1D}/(2\pi) = 21$ MHz and $\tau_d = 227$ ns into equation 4.29, we obtain the magenta curve plotted in Fig. 2.4b. As discussed in the main text, our measured

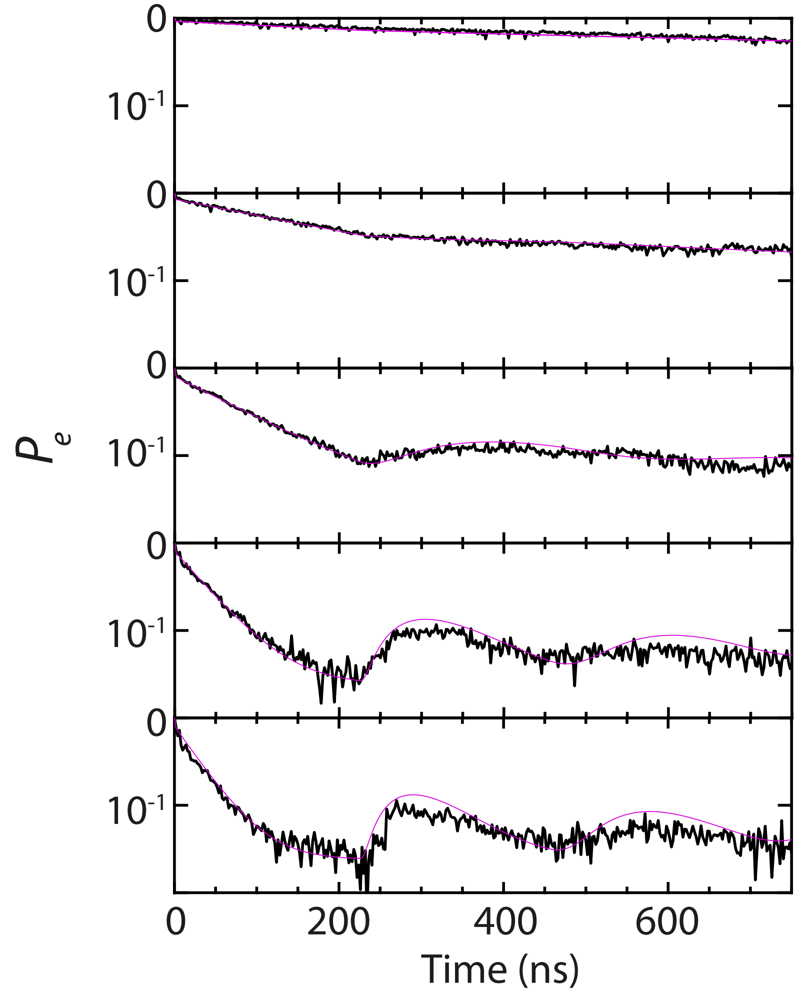

Figure 4.7: **Markovian to Non-Markovian crossover.** Replots of the five (white) line cuts of Fig. 2.4c, with accompanying theoretical predictions for emission of a qubit into a dispersionless, lossless semi-infinite waveguide. In the theoretical model, τ_d was maintained fixed for all simulations, while the qubit emission rate Γ_{1D} and round-trip phase ϕ were allowed to vary as fit parameters in to capture the effects of the changing flux-modulation amplitude, which not only changes Γ_{1D} but also causes a residual DC-shift of the average qubit frequency [85], which in turn affects ϕ. Moreover, a thermal qubit population of 2.4% was assumed. From top panel to bottom panel, the fit parameters Γ_{1D} and ϕ are, respectively: $\Gamma_{1D}/2\pi = 0.17$ MHz, $\phi = \pi/2.6$; $\Gamma_{1D}/2\pi = 0.6$ MHz, $\phi = \pi/2.6$; $\Gamma_{1D}/2\pi = 1.8$ MHz, $\phi = \pi/2.1$; $\Gamma_{1D}/2\pi = 5$ MHz, $\phi = \pi/2.6$. Note that the parameter ϕ has negligible effect for dynamics involving large Γ_{1D} where revival events are clearly discernible, and for dynamics involving small Γ_{1D}, ϕ simply modulates the emission rate. However, for intermediate Γ_{1D} such as $\Gamma_{1D}/2\pi = 0.6$ MHz, 1.8 MHz, the shapes of the population dynamics curves are sensitive to ϕ.

dynamics compare favorably to the ideal scenario of no dispersion-induced distortion of the traveling emitted pulse, as well as no propagation losses, captured by the model discussed above. Thus, the limited recurrence observed can be mostly attributed to emission into the open end of the waveguide, as well as inefficient re-absorption of the emitted wavepacket due to its exponential shape.

In addition, we have also plotted similar comparisons between this ideal model of the observed time-delayed feedback phenomenon, and the data shown in Fig. 2.4c. For this comparison, we choose to plot the five line cuts plotted in white in Fig. 2.4c, along with comparisons to the theoretical model. The agreement between the two for all five curves is similar to the agreement observed in Fig. 2.4b. Quantification of the non-Markovianity of the discussed model under various parameters is presented in Ref. [37]; however, as the reference notes, there are many competing manners to quantify non-Markovianity.

PART 2: QUANTUM TRANSDUCTION

As mentioned in the introduction to the thesis, Part 2 will deal with the development of a quantum transducer device that can convert microwave frequency photons from a superconducting qubit (f ~ 5 GHz) into optical photons in the telecommunications band (f ~ 200 THz). These optical photons can then be transmitted over long distances using low loss optical fibers at room temperature opening up prospects for quantum communication between remote superconducting qubit based quantum processors. There are many different schemes for quantum transduction including schemes based on cold atoms [121–123], rare earth ions [124–127], electro-optics [128–135], and electro/piezo-optomechanics [10, 136–149]. In this thesis, we develop a piezo-optomechanical quantum transducer device.

Our transducer device can be split into two parts: 1. A piezo-acoustic part that converts microwave photons from a superconducting qubit into microwave phonons using the piezo-electric effect. 2. An optomechanical part that subsequently converts the microwave phonons into optical photons using an optomechanical interaction. Building on past work done in the Painter group, we utilize a (modified) one-dimensional optomechanical crystal (1D-OMC) to generate the optomechanical coupling. A brief summary of the theory of cavity optomechanics and the basic concepts underlying 1D-OMC devices developed by past generations of students in the Painter group is presented in Chapter 5. The design of the piezo-acoustic cavity is presented in Chapter 6. These two independently designed parts are then connected together to form our full transducer device. Details of the design of the full device and analysis of the expected efficiency and added noise of the transducer are also presented in Chapter 6.

In Chapter 7, we will discuss the repetition rate at which we can operate the transducer device presented in Chapter 6. The repetition rate is limited by the generation of quasiparticles (breaking of Cooper pairs) in the superconductor when an optical pulse is applied in close proximity to the superconducting circuit. The quasiparticle relaxation time is a key factor determining the repetition rate of the transducer device. We will develop niobium (Nb) based transmon qubits (in contrast to the all-aluminum (Al) transmon qubits used in Part 1) and test their optical power handling capability. When exposed to optical illumination, we find that Nb-based transmon qubits recover on a faster timescale than Al-based transmon qubits and hence are more suited for incorporation into a quantum transducer device.

The final two chapters of Part 2 will deal with some of the nanofabrication challenges in realizing our transducer device. As will be seen in Chapter 6, our transducer device is designed on a thin film lithium niobate on silicon-on-insulator platform (LN on SOI). An etch process for etching lithium niobate on silicon-on-insulator and the challenges involved is discussed in Chapter 9. Integrating niobium based superconducting circuits with the transducer device requires fabrication of niobium qubits on silicon-on-insulator substrates. A fabrication process for niobium based superconducting qubits on silicon-on-insulator substrates is developed in Chapter 8.

Chapter 5

BACKGROUND: CAVITY OPTOMECHANICS AND 1D OPTOMECHANICAL CRYSTALS

In this chapter, we briefly introduce the theory of cavity optomechanics and the design of optomechanical devices used in the subsequent chapters. This discussion will be brief and focused mainly on one-dimensional optomechanical crystals (1D OMC). For a more complete review of the theory of cavity optomechanics, please see [150, 151]. For detailed studies of 1D OMC devices carried out in the Painter group, please see [152–156].

5.1 Cavity Optomechanics Hamiltonian

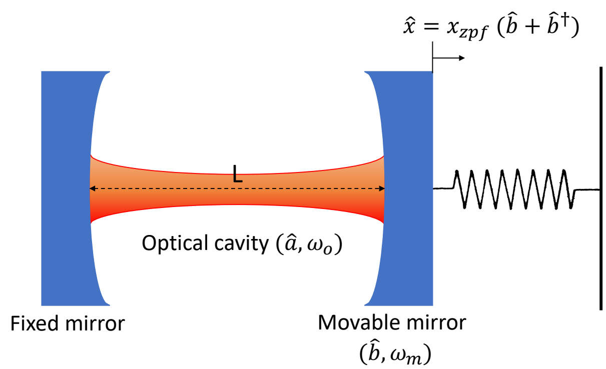

Figure 5.1: **Canonical cavity optomechanical system consisting of a Fabry-Perot optical cavity with a movable mirror.**

The canonical cavity optomechanical system shown in Fig.5.1 consists of a Fabry-Perot optical cavity where one mirror (of mass ‘m’) is attached to a spring and free to move. Optical photons entering this cavity exert a radiation pressure force which causes displacement of the mirror. This in turn changes the effective length of the Fabry-Perot cavity and modulates the cavity frequency. The Hamiltonian representing this system can be written as:

$$\hat{H} = \hbar\omega_c(x)\hat{a}^{\dagger}\hat{a} + \hbar\omega_m\hat{b}^{\dagger}\hat{b} \tag{5.1}$$

Here the first term represents the optical cavity at frequency $\omega_c(x)$ which depends on the displacement ‘x’ of the movable mirror. The second term represents the mechanical motion of the mirror at frequency ω_m. The optical frequency can be written as $\omega_c(x) = 2\pi * c/(2(L+x))$ where c is the speed of light and L+x is the effective length of the Fabry-Perot cavity. For $x \ll L$, we can approximate the frequency of the optical cavity as

$$\begin{aligned} \omega_c(x) &= 2\pi \left(\frac{c}{2L} (1-x) \right) \\ &= \omega_o - \frac{x}{L}\omega_o \end{aligned} \tag{5.2}$$

where $\omega_o = 2\pi * (c/2L)$ is the bare cavity frequency corresponding to x = 0. Identifying the position operator of the mechanical mode as $\hat{x} = x_{\text{zpf}} \left(\hat{b} + \hat{b^\dagger} \right)$ where $x_{\text{zpf}} = \sqrt{\hbar/(2m\omega_m)}$ is the zero-point motion of the mechanical oscillator, we arrive at the following Hamiltonian

$$\hat{H} = \hbar\omega_o \hat{a}^\dagger \hat{a} + \hbar\omega_m \hat{b}^\dagger \hat{b} - \hbar g_0 \hat{a}^\dagger \hat{a} \left(\hat{b} + \hat{b^\dagger} \right) \tag{5.3}$$

where $g_0 = \omega_o x_{\text{zpf}}/L$. While we derived the Hamiltonian in Eq.5.3 starting for a Fabry-Perot cavity with a mechanically compliant mirror, it is applicable to a wide variety of cavity optomechanical systems including the specific nanomechanical 1D optomechanical crystals we will use in this thesis. In our experiments, we will typically drive the optical cavity with a laser at frequency ω_L. We can rewrite the Hamiltonian in Eq.5.3 in a rotating frame at the laser frequency ω_L as

$$\hat{H} = -\hbar\Delta \hat{a}^\dagger \hat{a} + \hbar\omega_m \hat{b}^\dagger \hat{b} - \hbar g_0 \hat{a}^\dagger \hat{a} \left(\hat{b} + \hat{b^\dagger} \right) \tag{5.4}$$

where $\Delta = \omega_L - \omega_o$. The optical field consists of a large coherent part (α) with small quantum fluctuations ($\delta\hat{a}$), so we linearize the Hamiltonian by making the substitution $\hat{a} = \alpha + \delta\hat{a}$. We can then rewrite the interaction part of the Hamiltonian as

$$\begin{aligned} \hat{H}_I &= \hbar g_0 \hat{a}^\dagger \hat{a} \left(\hat{b} + \hat{b^\dagger} \right) \\ &= \hbar g_0 \left(\alpha + \delta\hat{a}^\dagger \right) (\alpha + \delta\hat{a}) \left(\hat{b} + \hat{b}^\dagger \right) \\ &= \hbar g_0 \left(\hat{b} + \hat{b}^\dagger \right) \left(\alpha^2 + \alpha\delta\hat{a}^\dagger + \alpha\delta\hat{a} + \delta\hat{a}^\dagger \delta\hat{a} \right) \end{aligned} \tag{5.5}$$

The first term in the last line of Eq.5.5 is proportional to α^2 and corresponds to a static radiation pressure force exerted on the mechanical oscillator causing a constant displacement. By redefining the origin of displacement we can ignore this term. The last term is smaller by a factor of α, so we will ignore this term too. As a result, we are left with

$$\hat{H}_I = \hbar g_0 \alpha \left(\delta\hat{a} + \delta\hat{a}^\dagger \right) \left(\hat{b} + \hat{b}^\dagger \right) \tag{5.6}$$

The full linearized Hamiltonian in the rotating frame is

$$\hat{H} = -\hbar\Delta\hat{a}^{\dagger}\hat{a} + \hbar\omega_m\hat{b}^{\dagger}\hat{b} - \hbar g_0\alpha\left(\delta\hat{a} + \delta\hat{a}^{\dagger}\right)\left(\hat{b} + \hat{b}^{\dagger}\right) \tag{5.7}$$

We identify $\alpha = \sqrt{n_{\text{cav}}}$ as the square root of the number of photons in the optical cavity and refer to $G = g_0\sqrt{n_{\text{cav}}}$ as the optomechanical coupling rate and g_0 as the *single photon* optomechanical coupling rate.

5.2 Equations of Motion

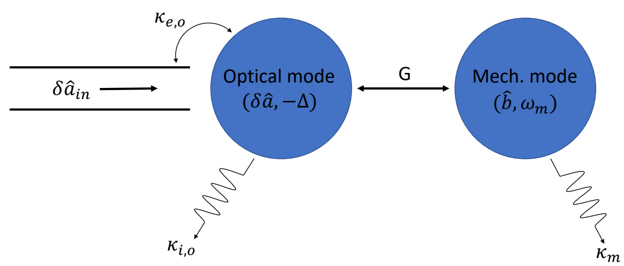

Figure 5.2: **Schematic of a driven optical cavity coupled to a mechanical mode.**

Using the linearized Hamiltonian of Eq.5.7 and applying input-output formalism to the case of a driven optical mode coupled to a mechanical mode as shown in Fig.5.2, we can write down the equations of motion for the optical and mechanical fields as

$$\begin{aligned}\delta\dot{\hat{a}} &= \left(i\Delta - \frac{\kappa_o}{2}\right)\delta\hat{a} + iG\left(b + b^{\dagger}\right) + \sqrt{\kappa_{e,o}}\delta\hat{a}_{in} + \sqrt{\kappa_{i,o}}\delta\hat{a}_{in,i}\\ \dot{\hat{b}} &= \left(-i\omega_m - \frac{\kappa_m}{2}\right)\hat{b} + iG\left(\delta\hat{a} + \delta\hat{a}^{\dagger}\right) + \sqrt{\kappa_m}\hat{b}_{in,i}\end{aligned} \tag{5.8}$$

Here κ_o is the total optical loss rate which we have divided into intrinsic loss $\kappa_{i,o}$ and extrinsic loss $\kappa_{e,o}$ as shown in Fig.5.2. κ_m is the total mechanics loss rate, $\delta\hat{a}_{in}$ is the input optical field, and $\delta\hat{a}_{in,i}$ and $\hat{b}_{in,i}$ are quantum noise operators for the optical and mechanical modes, respectively.

We can solve these coupled equations by Fourier transforming to the frequency domain which yields

$$\begin{aligned}\delta\hat{a}[\omega] &= \frac{-iG\left(\hat{b}[\omega] + \hat{b}^{\dagger}[\omega]\right) - \sqrt{\kappa_{e,o}}\delta\hat{a}_{in}[\omega] - \sqrt{\kappa_{i,o}}\delta\hat{a}_{in,i}[\omega]}{i\left(\Delta + \omega\right) - \frac{\kappa_o}{2}}\\ \hat{b}[\omega] &= \frac{-iG\left(\delta\hat{a}[\omega] + \delta\hat{a}^{\dagger}[\omega]\right) - \sqrt{\kappa_m}\hat{b}_{in,i}[\omega]}{i\left(\omega - \omega_m\right) - \frac{\kappa_m}{2}}\end{aligned} \tag{5.9}$$

Substituting the expression for $\delta\hat{a}[\omega]$ in the expression for $\hat{b}[\omega]$ in Eq.5.9, it can be shown that the optomechanical interaction modifies the mechanical frequency as $\omega_m' = \omega_m + \delta\omega_m$ and also modifies the mechanical loss rate as $\kappa_m' = \kappa_m + \gamma_{om}$ where

$$\begin{aligned} \delta\omega_m &= \frac{G^2\omega_m}{\omega}\mathrm{Re}\left[\frac{1}{(\Delta+\omega)+i\frac{\kappa_o}{2}} + \frac{1}{(\Delta-\omega)-i\frac{\kappa_o}{2}}\right] \\ \gamma_{om} &= -\frac{2G^2\omega_m}{\omega}\mathrm{Im}\left[\frac{1}{(\Delta+\omega)+i\frac{\kappa_o}{2}} + \frac{1}{(\Delta-\omega)-i\frac{\kappa_o}{2}}\right] \end{aligned} \tag{5.10}$$

For the purpose of quantum transduction, we are particularly interested in the optomechanical damping rate γ_{om} at the mechanical frequency ($\omega = \omega_m$). Further, we make the following assumptions:

1. We assume we are in the sideband resolved regime defined by $\omega_m \gg \kappa_o$. For the transducer device considered in this thesis, $\omega_m \sim 2\pi \times 5\text{GHz}$ while $\kappa_o \sim 2\pi \times 500\text{MHz}$ so this assumption is justified
2. We will drive our transducer device with a laser at a frequency (ω_L) that is red detuned from the optical resonance by the mechanical frequency. $\omega_L = \omega_o - \omega_m \implies \Delta = -\omega_m$.

With these assumptions we find

$$\gamma_{om} = \frac{4g_0^2 n_{\text{cav}}}{\kappa_o} \tag{5.11}$$

where we have explicitly written the optomechanical coupling G in terms of the *single photon* optomechanical coupling rate g_0 and the intra-cavity photon number n_{cav}.

Intuitively, we are converting phonons from the mechanical mode into photons in the optical cavity. This is a parametric process where the laser drive is acting as a pump to make up for the frequency difference between the phonons and the optical photons ($\omega_L = \omega_m - \omega_o$). The rate at which we can convert phonons to photons is given by the optomechanical scattering rate γ_{om} which is dependent on the laser pump power via the intra-cavity photon number n_{cav}. An important figure of merit is the optomechanical cooperativity defined as

$$C_{om} = \frac{\gamma_{om}}{\kappa_m} \tag{5.12}$$

Intuitively we can think of γ_{om} as the 'good damping' rate where phonons in the mechanical mode are being converted into photons in the optical mode which we can then detect. κ_m on the other hand is the undesirable 'bad damping' rate where phonons in the mechanical mode are leaking out into the environment and being lost. We can then understand the optomechanical cooperativity as the ratio of the 'good damping' into the optical mode (γ_{om}) divided by the 'bad damping' κ_m. This will be a very important figure of merit to keep in mind when we discuss the efficiency of our quantum transducer device in Chapter 6.

5.3 1D Optomechanical Crystals

There are a wide variety of systems that have been used to realize optomechanical coupling. These range from microscopic systems such as cold atoms coupled to an optical cavity [157, 158] to macroscopic systems involving suspended mirrors [159–161]. In our transducer, we will utilize a nanoscale device called a 1D optomechanical crystal (1D OMC). We are interested in coupling microwave frequency phonons (~ 5GHz) to telecom band photons (~ 200 THz). Due to the large difference in the velocity of light and sound, the wavelength of telecom band photons and microwave phonons is roughly equal (~ μm scale). This is convenient as it allows us to co-localize microwave frequency mechanical modes and telecom band optical modes in the same wavelength scale device (~ μm). Recall from our expression for $g_0 = \omega_0 x_{\text{zpf}}/L$, shrinking the size (L) of our optomechanical system down to the wavelength scale allows us to achieve large single photon optomechanical coupling. Here we describe the basic design of a 1D OMC. This topic has been covered in great detail in previous work from the Painter group so our discussion here will be brief.

A 1D optomechanical crystal is shown in Fig 5.3 a. It consists of a nano-beam patterned from a 220 nm thick silicon device layer of a silicon on insulator substrate. By shrinking the thickness and width of the beam to be sub-wavelength, we get an effective 1D structure. At either end of the nano-beam, we have the 'mirror region' which consists of an array of identical periodically patterned elliptical holes that act as a metamaterial and are designed to support a *simultaneous* optical bandgap centered around 194 THz and acoustic bandgap centered around 5GHz (Fig 5.3 b,c). (Technically these bandgaps are really pseudo-bandgaps—they act as bandgaps only for modes possessing a particular symmetry. However, in the ideal situation, modes of different symmetry do not couple to each other so as long as our mode of interest possesses the correct symmetry, it can be well isolated inside the pseudo-bandgap.) In the middle of the nano-beam, we have the 'defect region' where we break the translational symmetry of the mirror region by adiabatically tuning the dimensions

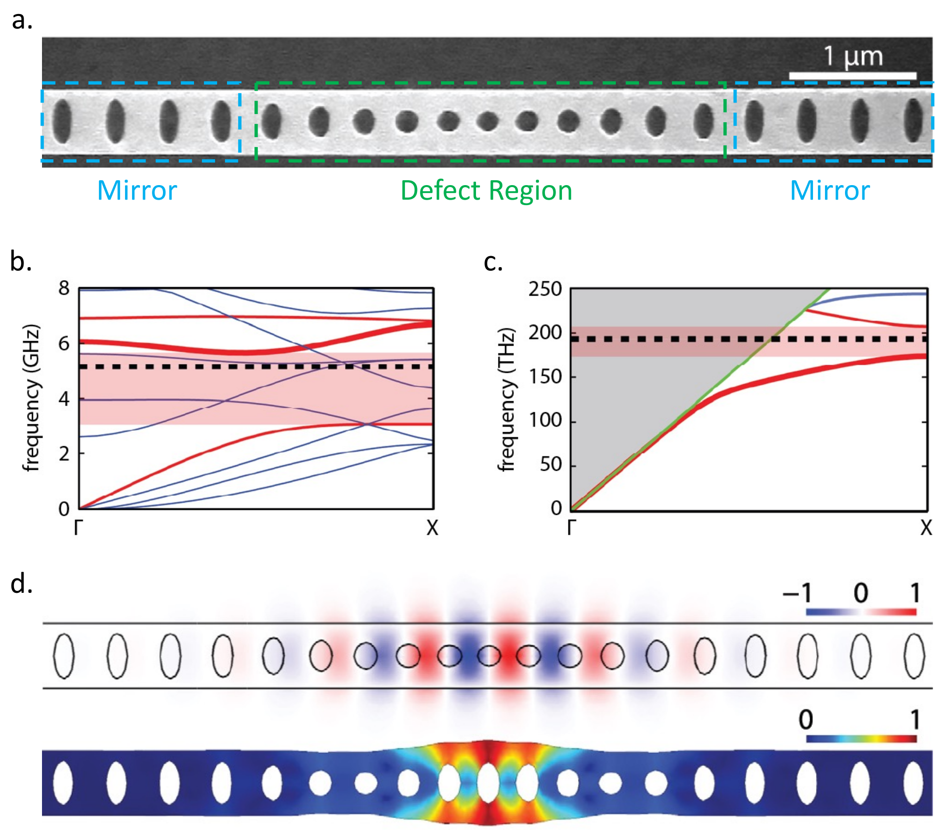

Figure 5.3: **1D optomechanical crystal. a.** Scanning electron microscope (SEM) image of a 1D optomechanical crystal cavity. **b.** mechanical and **c.** optical band structure for propagation along the x-axis in the nominal mirror unit cell, with quasi-bandgaps (red regions) and cavity mode frequencies (black dashed) indicated. In **b.**, modes that are y- and z-symmetric (red bands), and modes of other vector symmetries (blue bands) are indicated. In **c.**, the light line (green curve) divides the diagram into two regions: the gray shaded region above representing a continuum of radiation and leaky modes, and the white region below containing guided modes with y-symmetric (red bands) and y-antisymmetric (blue bands) vector symmetries. The bands from which the localized cavity modes are formed are shown as thicker curves. **d.** The normalized optical E_y field and the normalized mechanical displacement field $\mathbf{Q}$ of the localized optical and mechanical modes, respectively. Figure reproduced from [152]

of the holes. This ‘defect region’ supports both an optical mode at 194 THz inside the optical bandgap and an acoustic mode at 5 GHz inside the acoustic bandgap. Conceptually, by periodically patterning holes in the nano-beam, we are modulating the effective refractive index thus creating a distributed Bragg mirror where we get constructive interference of multiple reflections which tightly confines the optical field to the defect region. Similarly, the array of holes is also periodically modulating the mass of the nano-beam giving us an effective ‘acoustic Bragg mirror’ which serves to tightly confine the acoustic field.

We can use finite element simulation methods to calculate the electric field profile **E** and the displacement profile **Q** of the 1D OMC. This allows us to calculate the single photon optomechanical coupling g_0 which has two contributions,

1. A moving boundary contribution ($g_{0,\mathrm{MB}}$) similar to the moving end mirror of a Fabry-Perot cavity which can be calculated as

$$g_{0,\mathrm{MB}} = -\frac{\omega_o}{2}\frac{\oint (\mathbf{Q}\cdot\hat{\mathbf{n}})(\Delta\epsilon\mathbf{E}_{||}^2 - \Delta\epsilon^{-1}\mathbf{D}_{\perp}^2)dS}{\int \mathbf{D}\cdot\mathbf{E}} \tag{5.13}$$

   where **Q** is the normalized displacement profile on the silicon surface, $\hat{\mathbf{n}}$ is the surface normal, $\mathbf{E}_{||}$ is the electric field parallel to the surface, $\mathbf{D}_{\perp}$ is the electric displacement field perpendicular to the surface, $\Delta\epsilon = \epsilon_{\mathrm{Si}} - \epsilon_{\mathrm{Air}}$, and $\Delta\epsilon^{-1} = \epsilon_{\mathrm{Si}}^{-1} - \epsilon_{\mathrm{Air}}^{-1}$.

2. A photoelastic contribution ($g_{0,\mathrm{PE}}$) where the strain induced by the mechanical displacement causes a change in the refractive index. This contirbution can be calculated as

$$g_{0,\mathrm{PE}} = \frac{\omega_o\epsilon_0 n^4}{2}\frac{\int_{\mathrm{Si}} \mathbf{E}^{\dagger}\cdot[\mathbf{pS}]\cdot\mathbf{E}\,dV}{\int \mathbf{D}\cdot\mathbf{E}\,dV}, \tag{5.14}$$

   where ω_o is the optical frequency, n is the refractive index, **E** is the electric field, **p** is the photoelastic tensor, and **S** is the strain tensor.

The total single photon optomechanical coupling rate is $g_0 = g_{0,\mathrm{MB}} + g_{0,\mathrm{PE}}$. The optical and mechanical mode shapes of a 1D OMC are plotted in Fig 5.3 d. It is clear that both the optical and acoustic fields are co-localized and confined tightly to the defect region leading to a large overlap between these fields giving rise to a large single photon optomechanical coupling rate g_0. State of the art 1D OMC devices in silicon have been shown to achieve $g_0 \sim 1.1$MHz [152]. The carefully engineered acoustic and optical bandgaps surrounding our modes of interest help minimize radiation losses yielding high quality factors for the acoustic and optical modes. The ease of fabrication and low material loss of silicon further helps to create modes with very low intrinsic loss. State of the art 1D OMC devices have demonstrated intrinsic optical linewidths $\kappa_{i,o} \sim 500$MHz and mechanical linewidths $\kappa_m \sim 4$kHz [162]. Large g_0 and small κ_o and κ_m are essential for maximizing the optomechanical cooperativity and hence the transduction efficiency as we will see in Chapter 6.

Chapter 6

DESIGN OF A WAVELENGTH-SCALE PIEZO-OPTOMECHANICAL QUANTUM TRANSDUCER

6.1 Introduction

A quantum transducer can be specified as a linear device with a certain conversion efficiency, added noise level, and repetition rate. Current approaches for microwave to optical quantum transduction rely on a strong optical pump to mediate the conversion process between single photon-level signals at both frequencies. Increasing pump power allows for higher conversion efficiency, but due to parasitic effects of optical absorption in various components of the transducer and the vast difference in energy scales between optical and microwave frequencies, this often adds more noise to the conversion process. For applications in the quantum regime, the number of added noise photons per transduced photon should be less than 1. In several approaches, this trade-off between efficiency and noise has been a key obstacle to transduction of quantum signals [10, 133, 141, 144, 145, 149]. Recently a piezo-optomechanical approach has been used to demonstrate optical measurements of the quantum state of a superconducting transmon qubit with added noise levels below 1 photon [10]. In this work, we build on this piezo-optomechanical transduction approach with a design optimized for high efficiency and low noise. The goal of this design is to achieve performance improvements essential to detect quantum correlations in transduced photons on reasonable timescales.

Fig. 6.1a illustrates the mode picture of our transduction scheme. An intermediary mode $\hat{b}_m$ of a nanomechanical oscillator simultaneously couples to microwave photons from mode $\hat{c}_q$ of a microwave circuit, and to optical photons from mode $\hat{a}_o$ of an optical cavity. Microwave photons are converted to phonons via a resonant piezoelectric interaction, and these phonons are subsequently converted into optical photons via a parametric optomechanical interaction. The microwave photon-phonon conversion is realized by tuning the circuit frequency ω_q on resonance with the mechanical frequency ω_m. The phonon-optical photon conversion is realized by driving the optical cavity at frequency ω_d that is red-detuned by exactly the mechanical frequency s.t $\omega_d - \omega_o = -\omega_m$.

We realize the intermediary mechanical mode in the above schematic by connecting a

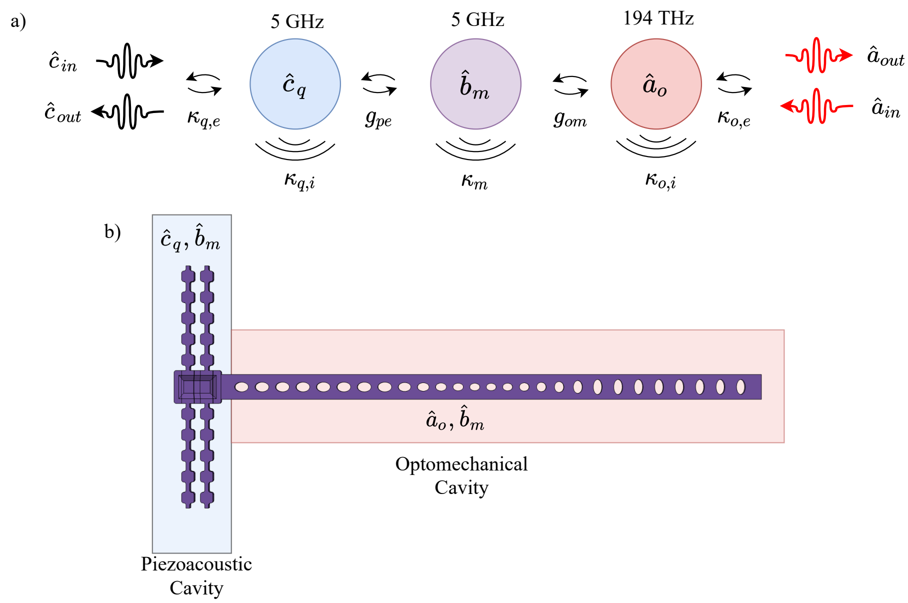

Figure 6.1: **Schematic of piezo-optomechanical transducer.** **a.** Mode schematic for piezo-optomechanical transduction. **b.** Device schematic for the transducer in this work. The device can be split into two regions, one which couples strongly to microwave electric fields and one which couples strongly to optical fields. Both are part of the same mechanical 'supermode' $\hat{b}_m$.

wavelength-scale piezoacoustic cavity and an optomechanical crystal (OMC) cavity (see Fig. 6.1b). The acoustic modes of these components are strongly hybridized to form a mechanical 'supermode' whose mechanical displacement highly overlaps in one region with the field of a microwave circuit, and in another region with the field of an optical cavity. Using physically separate cavities allows us to independently optimize the piezoacoustic and optomechanical components of the transducer. Our design is formed from thin-film lithium niobate (LN) on the device layer of a silicon-on-insulator (SOI) chip. We define the piezo-acoustic cavity in LN, which has large piezoelectric coefficients [163]. We define the OMC in silicon, since its large photoelastic coefficients [164] and refractive index [165] allow high optomechanical coupling. Well-established nanofabrication processes also allow high optical and mechanical quality factors for silicon OMCs [152, 162]. For the microwave circuit in this design, we consider a transmon qubit [16] with electrodes routed over the LN region to allow for capacitive coupling to the piezoacoustic cavity. The transmon is patterned using niobium, a standard material platform for realizing high-coherence qubits [166, 167]. The buried oxide layer underneath these components is etched away, leaving a suspended silicon membrane as the substrate for our device.

Our design procedure begins with independently optimizing the piezoacoustic and

OMC cavities for high g_{pe} and g_{om}, respectively. We design for closely matched acoustic modes at 5 GHz in both resonators, and for an optical mode at telecom wavelength (1550 nm). During the design process, it is crucial to maintain a low acoustic mode density such that the transduction schematic in Fig. 1a using a single acoustic mode remains valid. Further, since thin film LN has higher microwave dielectric and acoustic loss than silicon, we aim to minimize the piezo volume in our device. The two independently optimized cavities are then physically connected, and the parameters of the resulting hybrid acoustic modes are analyzed. Using this approach, we design a transducer with expected conversion efficiency at the percent level while maintaining added noise photons <0.5.

6.2 Piezo Cavity Design

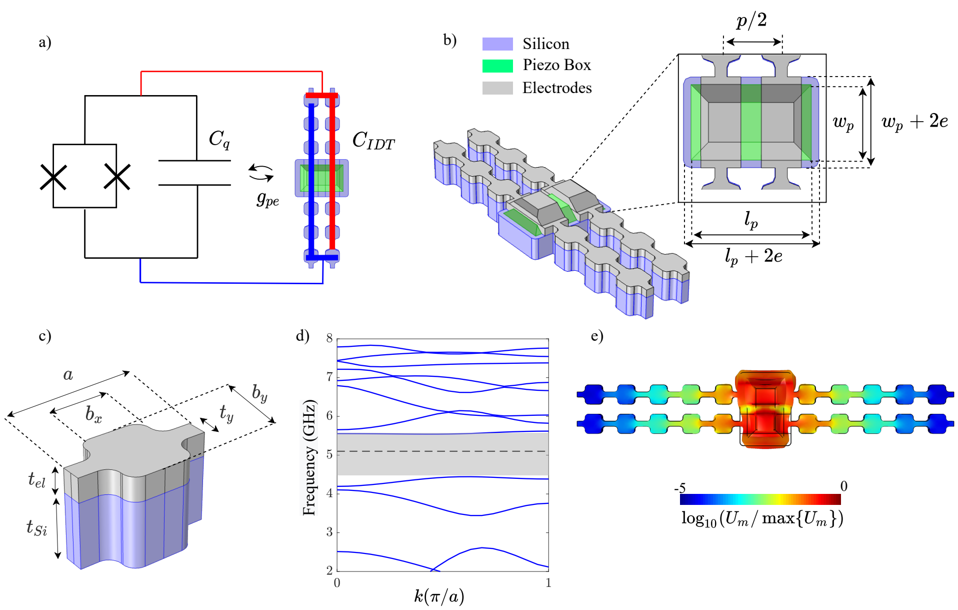

Figure 6.2: **Design of phononic shield a.** Schematic illustrating the capacitive routing of the piezoacoustic cavity to a transmon qubit. The qubit here can be replaced with a microwave resonator without loss of generality. **b.** Piezoacoustic cavity geometry, with relevant dimensions defined in blowout top view. **c.** Phononic shield unit cell, with relevant dimensions defined. **d.** Mechanical bandstructure of phononic shield unit cell in c), with (a, b_x, b_y, t_y) = (445, 225, 265, 70)nm. We observe a complete acoustic bandgap in excess of 1GHz around 5GHz. **e.** Log scale of mechanical energy U_m for piezoacoustic cavity mode at 5GHz, normalized to maximum value. We find >4 orders of magnitude suppression for 5 phononic shield periods.

The piezoacoustic cavity consists of a slab of lithium niobate on top of a suspended silicon membrane patterned in the shape of a box. We work with 100nm thin-film -Z-cut lithium niobate on top of a 220nm thick suspended silicon device layer. 80nm-thick Nb electrodes run over the top of the slab and are routed in the form of an interdigital transducer (IDT) which capacitively couples the cavity to a microwave circuit such as a transmon qubit, as seen in Fig. 6.2a.

The box is surrounded by a periodically patterned phononic shield to mitigate acoustic radiation losses and to clamp the membrane to the surrounding substrate. The clamps are spaced periodically so that the IDT electrodes are routed over the top of each clamp, providing a means for electrical routing which is not acoustically lossy.

The phononic shield uses an alternating block and tether pattern (see relevant dimensions in Fig. 6.2c) consisting of metal electrodes on top of a silicon base. By tuning the parameters a, b_x, b_y, and t_y, we achieve a >1GHz acoustic bandgap centered around 5GHz, the frequency of the mechanical mode of interest (Fig 6.2d). This yields strong confinement of mechanical energy inside the piezo region for sufficient number of shield periods, enabling high mechanical quality factors. By simulating the mechanical energy density across the entire cavity, we find that 5 shield periods provide >4 orders of magnitude suppression of acoustic radiation into the environment, as shown in Fig. 6.2e.

The dimensions of the piezo box (outlined in Fig. 6.2b) are designed to support a periodic mechanical mode whose periodicity matches that of the IDT fingers. This results in high overlap between the electric field from the IDT and the electric field induced by mechanical motion in the piezo box. This overlap gives a microwave photon-phonon piezoelectric coupling rate which is derived using first order perturbation theory:

$$g_{pe} = \frac{\omega_m}{4\sqrt{2U_m U_q}} \int_{\mathrm{LN}} \mathbf{D}_m \cdot \mathbf{E}_q \, dV. \tag{6.1}$$

Here the integral is taken over the entire LN slab, $\mathbf{D}_m$ is the electric displacement field induced from mechanical motion in the piezo region, and $\mathbf{E}_q$ is the single-photon electric field generated by the transmon qubit across the IDT electrodes. The fields are normalized to their respective zero-point energies $\hbar\omega_m/2$, yielding the pre-factor in front of the integral in (1). U_m is the total cavity mechanical energy, and $U_q = \frac{1}{2}(C_q + C_{\mathrm{IDT}})V_0^2$ is the total IDT electrostatic energy. We note that the electrostatic energy is dependent on both the qubit capacitance C_q and IDT finger capacitance C_{IDT}, and therefore the coupling rate scales as $(C_q + C_{\mathrm{IDT}})^{-1/2}$. For our calculations in this work, we assume $C_q = 70\mathrm{fF}$ which is a typical value for transmon qubit capacitance. Replacing the transmon qubit with a high-impedance microwave resonator will allow lower $C_q \sim$ few fF [168], and can therefore further increase this coupling rate. $C_{\rm IDT}$ is calculated with finite-element electrostatic simulation and is typically on the order 0.1fF, a small contribution compared to transmon C_q.

The small value of $C_{\rm IDT}$ also minimizes the energy participation of the qubit electric field in the lossy piezo region, given by the ratio $\zeta_q = C_{\rm IDT}/C_q \sim 10^{-3}$. The contribution of lithium niobate to the qubit loss rate $\kappa_{q,i}$ is then estimated as $\zeta_q \kappa_{q,\rm LN}$. Using reported dielectric loss tangents in lithium niobate $\tan\delta = 2.5 \times 10^{-3}$ [169] giving $\kappa_{q,\rm LN}/2\pi = 12.5$MHz, we estimate the LN contribution to qubit loss to be $\zeta_q \kappa_{q,\rm LN}/2\pi \sim 10$kHz. This contribution is ~5x smaller than typical loss rates $\kappa_{q,\rm SOI}/2\pi \sim 50$kHz reported in transmon qubits fabricated on SOI [78]. As a result, the contribution of the piezo cavity to qubit loss is not a limiting factor, and justifies the on-chip coupling scheme outlined in Fig. 6.2a.

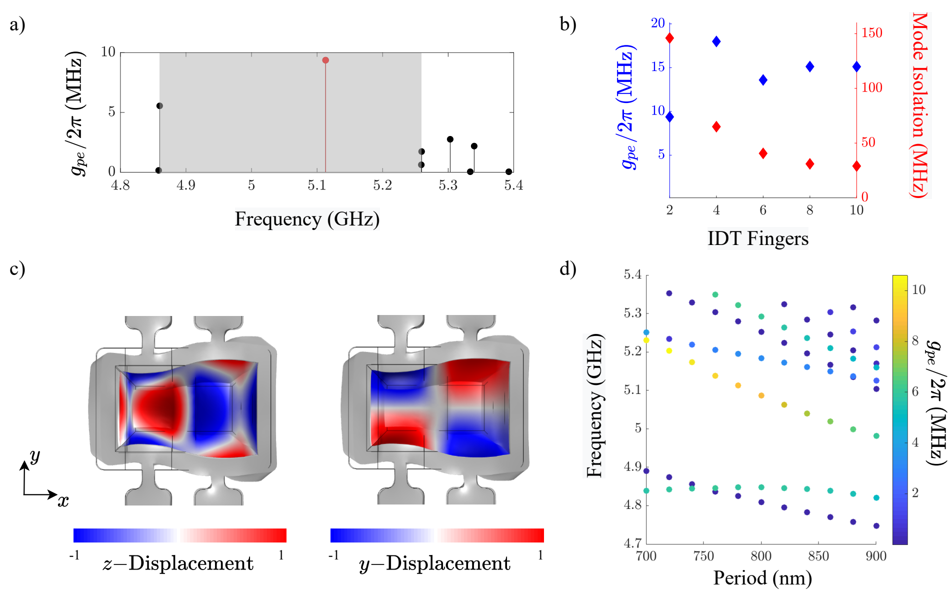

Figure 6.3: **Design of piezoacoustic cavity. a.** Mode structure for optimized piezoacoustic cavity design with $(p, w_p, e) = (783, 423, 118)$ nm. Mode of interest (red) achieves $g_{pe}/2\pi$ of 9.5MHz. Shaded grey region indicates the mode isolation window with the nearest mode >150MHz away. **b.** $g_{pe}/2\pi$ and mode isolation for optimized designs with differing number of IDT fingers. We observe g_{pe} saturating beyond $N = 4$ fingers, and mode isolation decreasing with increasing number of fingers. **c.** Mechanical mode shape of red mode in (a). Right shows the in-plane (breathing) and left shows the out-of-plane (Lamb-wave) components of the optimized mechanical mode. **d.** Mode structure and piezoelectric coupling vs. IDT period, with data points colored according to g_{pe}.

An important design consideration with this type of piezoacoustic cavity is the number of IDT fingers used. For N IDT fingers, the length l_p of the piezo region is given by $l_p = Np/2$, where p is the IDT period. As the number of fingers increases, the increased size of the piezo box results in a more crowded mode structure (Fig.

6.3b), and it is more difficult to isolate a single mechanical mode without coupling to parasitic modes in the vicinity of the mode of interest. This is of key importance as these parasitic modes may not hybridize well with the OMC cavity and reduce overall transduction efficiency. Reducing the size of the piezo region is also important to reduce microwave photon and phonon decoherence, as lithium niobate has high microwave dielectric and acoustic loss tangents compared to silicon (further discussion in Sec. 6.4). For these reasons, we choose a 2-finger design to minimize these effects. The strong piezoelectric nature of lithium niobate allows for g_{pe} values high enough for strong microwave photon-phonon coupling, even in the limit of 2 IDT fingers. We emphasize the small dimensions of the piezoacoustic cavity in this design in contrast with previous work on piezo-optomechanical quantum transducers [cite]. The benefits of this approach come at the cost of higher sensitivity of the piezo modes to changes in cavity dimensions. This can have large effects on hybridization with the OMC cavity and the performance of the final transducer device, which relies on resonant matching of acoustic modes in both regions. We show further in Sec. 6.4 that the achievable hybridization between piezo and OMC modes with this small piezo volume approach is large enough to protect the design against typical fabrication disorder.

The mechanical mode of interest is periodic with out-of-plane (Lamb-wave) and in-plane breathing components. The Lamb-wave component of the mode induces an electric field in the piezo region with high overlap with the IDT electric field, while the breathing component of the mode enables hybridization with the breathing mode of the optomechanical crystal to be attached in the full device (see Fig. 6.3c). The piezo mode can be tuned with three key parameters p, w_p, and e. p is the periodicity of the IDT fingers and is used to parameterize the piezo box length, given by $l_p = Np/2$ as described earlier. p is used to tune the frequency of the mode of interest (Fig. 6.3d) while maintaining appropriate phase-matching of the mode periodicity with the IDT fingers. w_p is the piezo box width, which can be increased to increase g_{pe} via larger mode volumes or decreased to reduce the mode crowding that results from larger box size. Finally, we define a silicon-piezo buffer parameter e, which extends the silicon box length/width by an amount e compared to the piezo box. This buffer is needed to protect against silicon/piezo box misalignment in the fabrication process, and acts as an added degree of freedom for tuning frequency, g_{pe}, and mode isolation. We use numerical optimization to tune parameters (p, w_p, e) to arrive at a design with high piezoelectric coupling and mode isolation. We employ a Nelder-Mead simplex optimization [170, 171] similar to that described in [152]. After optimization, we obtain a single mechanical mode with $g_{pe}/2\pi = 9.5$MHz, which is isolated by >150MHz from other mechanical modes (Fig. 6.3a). We will use this single mode to strongly couple to the modes of an optomechanical crystal cavity to create the mechanical supermode of Fig. 6.1a.

6.3 Optomechanics Design

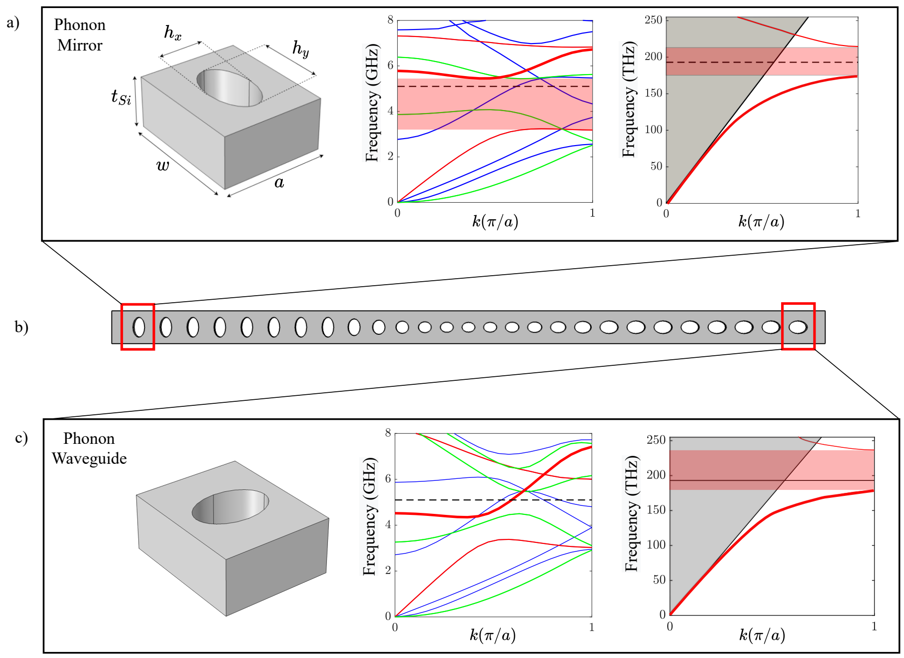

Figure 6.4: **Design of the optomechanical cavity. a.** Unit cell geometry, mechanical, and optical bandstructure of phonon mirror region with $(a, w, h_x, h_y) = (436, 529, 189, 320)$nm. Mechanical bands are color-coded by symmetry, with red (green) corresponding to breathing (Lamb-wave) mode symmetry classes. Blue bands represent all other symmetries. Mechanical bandgap for breathing modes and optical bandgap are both highlighted in red. **b.** Full OMC geometry, with phonon mirror and phonon waveguide unit cells highlighted. **c.** Unit cell geometry, mechanical, and optical bandstructure of phonon waveguide region with $(a, w, h_x, h_y) = (436, 529, 295, 205)$nm. Mechanical bands color-coded as in (a). Breathing mode crosses 5.1GHz resulting in waveguide-like behavior at the mechanical frequency. The optical bandgap is maintained.

The optomechanical crystal cavity is designed in a similar fashion to previous work [152], with the crucial change of a modified unit cell design on one side of the cavity to enable strong mechanical hybridization with the piezo cavity. This separates the OMC into three distinct regions: a phonon mirror, defect region, and phonon waveguide (see Fig. 6.4 for details). The phonon mirror unit cell (Fig. 6.4a) is designed to have a simultaneous mechanical and optical bandgap for modes of certain symmetry classes. In the defect region, the phonon mirror unit cell transitions to a defect cell designed to co-localize a 5.1GHz mechanical breathing mode and a 194THz ($\lambda_0 = 1550$nm) optical mode. The phonon waveguide unit cell (Fig. 6.4c) is mechanically transparent to breathing mode phonons at 5.1GHz, while maintaining a large bandgap for optical modes. This is achieved by modifying the ellipticity of the phonon mirror unit cell. We see in Fig. 6.4b that the resulting mechanical mode is permitted to leak out into the phonon waveguide region, while the optical mode remains highly localized within the defect region.

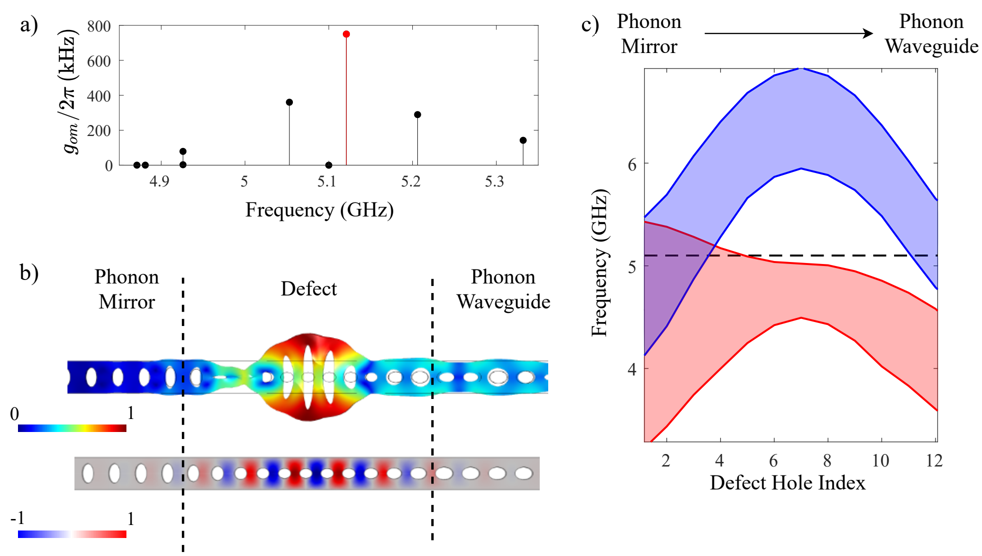

Figure 6.5: **Optomechanical cavity mode structure.** **a.** Resultant mode structure of optimized OMC design. Highest g_{om} mode (highlighted in red) gives 750kHz optomechanical coupling. **b.** OMC mechanical and optical mode shapes, along with unit cell length at each hole in the defect region. Phonon mirror, phonon waveguide, and defect region are labeled and outlined. **c.** Bandgap of different symmetries as a function of hole index along the defect region. Red shaded region represents the bandgap for breathing mode symmetries, and blue shaded region represents the bandgap for Lamb-wave mode symmetries.

The optomechanical coupling rate is calculated from the optical frequency shift arising due to the photoelastic effect [172] and moving dielectric boundaries [173], giving $g_{om} = g_{om,\mathrm{PE}} + g_{om,\mathrm{MB}}$. For a detailed derivation of both contributions to g_{om}, see [174]. The photoelastic contribution is derived from 1st order perturbation theory as

$$g_{om,\mathrm{PE}} = \frac{\omega_o \epsilon_0 n^4}{2} \frac{\int_{\mathrm{Si}} \mathbf{E}^\dagger \cdot [\mathbf{pS}] \cdot \mathbf{E}\, dV}{\int \mathbf{D} \cdot \mathbf{E}\, dV}, \tag{6.2}$$

where ω_o is the optical frequency, n is the refractive index, $\mathbf{E}$ is the electric field, $\mathbf{p}$ is the photoelastic tensor, and $\mathbf{S}$ is the strain tensor.

The moving boundaries component is derived similarly as

$$g_{om,\mathrm{MB}} = -\frac{\omega_o}{2} \frac{\oint (\mathbf{Q} \cdot \hat{\mathbf{n}})(\Delta\epsilon \mathbf{E}_{\parallel}^2 - \Delta\epsilon^{-1} \mathbf{D}_{\perp}^2) dS}{\int \mathbf{D} \cdot \mathbf{E}\, dV}, \tag{6.3}$$

where $\mathbf{Q}$ is the normalized mechanical displacement field, $\hat{\mathbf{n}}$ is the surface normal, $\mathbf{E}_{||}$ is the electric field parallel to the surface, $\mathbf{D}_{\perp}$ is the electric displacement field perpendicular to the surface, $\Delta\epsilon = \epsilon_{\text{Si}} - \epsilon_{\text{Air}}$, and $\Delta\epsilon^{-1} = \epsilon_{\text{Si}}^{-1} - \epsilon_{\text{Air}}^{-1}$.

One may expect the coupling rates in this design to suffer due to the delocalization of the mechanical mode. However, we find that after a Nelder-Mead simplex optimization of various OMC dimensions similar to [152], the resulting design gives multiple modes with high values of $g_{om}/2\pi$, with the maximum coupling rate exceeding 750kHz (Fig. 6.5a). This is comparable to state-of-the-art OMC designs in silicon which achieve $g_{om}/2\pi$ up to ~1MHz [162].

The radiation-limited optical quality factor Q_o can be simulated and is found to be in excess of 10^6, corresponding to an intrinsic optical loss rate $\kappa_{o,i}/2\pi \sim 200$MHz. However, Q_o is usually practically limited to $\sim 500{,}000$ ($\kappa_{o,i}/2\pi \sim 400$MHz) [162] due to optical scattering from surface defects introduced in the fabrication process. To ensure this limit is reached, we configure the optimization such that g_{om} is maximized while maintaining Q_o above $\sim 10^6$, well above the realistic Q_o limit.

The total optical loss rate is given by $\kappa_o = \kappa_{o,i} + \kappa_{o,e}$, where $\kappa_{o,e}$ is the decay rate associated with input coupling. $\kappa_{o,e}$ is controlled with a coupling waveguide and is typically designed so that $\kappa_{o,e} = \kappa_{o,i}$. The total optical loss rate is then $\kappa_o \approx 2\kappa_{o,i}/2\pi = 800$MHz.

When hybridizing the modes of the piezoacoustic and OMC cavities, we must consider the relative motional symmetry of the two cavity modes. Our OMC design contains only breathing motion, whereas the piezo cavity design contains both breathing and Lamb-wave components. If the OMC bandstructure permits propagation of 5GHz phonons with Lamb-wave symmetry, then the OMC breathing mode will hybridize with leaky, delocalized modes of Lamb-wave symmetry. This can reduce optomechanical coupling and contribute significantly to mechanical losses in the device. For this reason, the phonon mirror and waveguide dimensions are chosen such that their bandstructure exhibits a bandgap for modes of Lamb-wave-like symmetries. This is seen in the mechanics band diagrams of Fig. 6.4, where we see a bandgap for Lamb-wave-like modes (colored in green) in both the phonon mirror and waveguide region.

Fig. 6.5c further illustrates this idea by showing the mechanical bandgap of unit cells across the defect region for both breathing and Lamb-wave-like modes, shaded in red and blue, respectively. At the phonon waveguide side, the breathing mode bandgap falls below 5GHz, permitting the breathing motion of the piezo mode to couple strongly to the defect region. However, 5GHz lies inside the Lamb-wave bandgap, so that Lamb-wave motion from the piezo cavity decays in the phonon waveguide and does not interact with the defect region.

6.4 Full Device Design

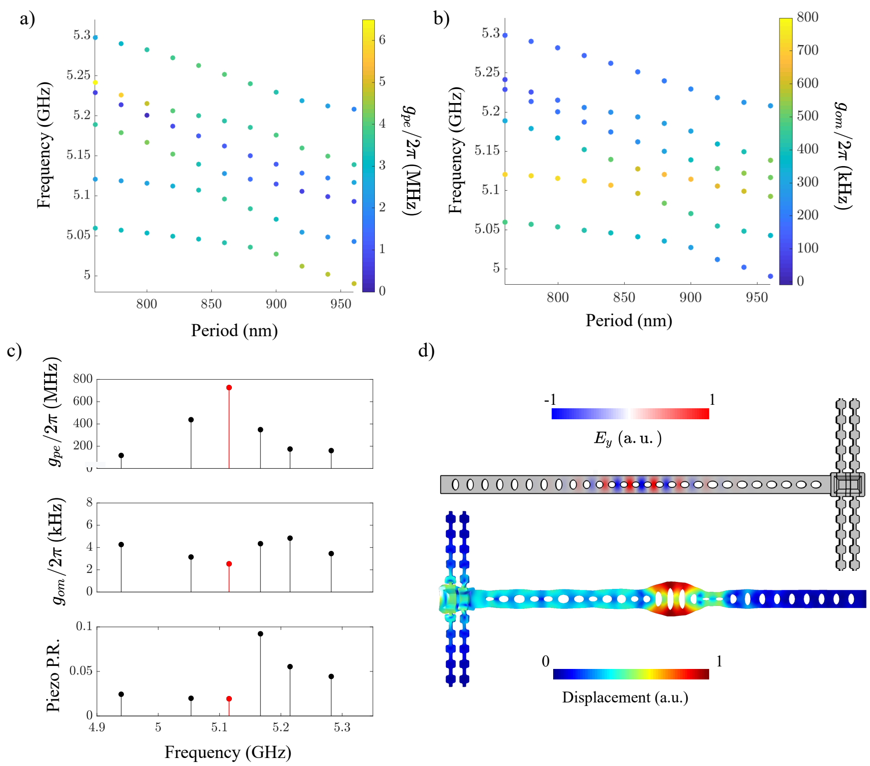

Figure 6.6: **Full piezo-optomechnaical transducer design. a.** Full transducer piezoelectric coupling and mode structure vs. IDT period. Shown are all modes which have either high piezoelectric or high optomechanical coupling. Data points are colored according to g_{pe} value. **b.** Full transducer optomechanical coupling and mode structure vs. IDT period. Shown are the same modes as in (a), only colored according to optomechanical coupling. **c.** Mode structure at p =800nm, showing g_{pe}, g_{om}, and energy participation ratio in the piezoelectric region. Red shows mode with highest combined g_{om} and g_{pe}, and lowest piezo participation (<2%). **d.** Mechanical mode profile of the mode highlighted in red in (c).

After independently designing the piezoacoustic and optomechanical cavities, we connect the two as shown in Fig. 6.6d and simulate the resulting hybridized mode structure. To observe the hybridization of the piezo and optomechanical modes, we sweep the IDT period in the piezo region to tune the piezo mode through the multiple optomechanical resonances. We find that over a frequency window >250MHz, there is a large number of mechanical modes with simultaneous high piezoelectric and optomechanical coupling rates. The phonon waveguide allows for strong enough mode hybridization that the piezoelectric coupling is distributed across a large number of modes. As shown in Fig. 6.6c, the mechanical energy participation in the piezo region ζ_m is in the range 1-10%. We find that across the entire hybridization window, at least one mode can be identified with $g_{om}/2\pi > 500$kHz, $g_{pe}/2\pi > 1$MHz, and $\zeta_m < 5\%$. In Fig. 6.6c, this mode is highlighted in red with $g_{om}/2\pi = 725$kHz, $g_{pe}/2\pi = 2.5$MHz, and $\zeta_m < 2\%$. We will use the values from this mode to quantify further calculations in this work. In practice, the frequencies and couplings of these mechanical modes are subject to change due to multiple sources of fabrication disorder. The multi-mode structure and relatively large hybridization ensure that the full device is robust to these shifts. While the exact frequencies and couplings may shift, Fig. 6.6a and 6.6b illustrate that the qualitative nature of the mode structure remains unchanged for a large range of frequency shifts. Additionally, the modes are separated far enough in frequency that their parasitic effect on each other's transduction efficiencies is minimal.

We may use the simulated piezo participation ratio and radiation loss to estimate the mechanical decoherence rate κ_m of our device. There are two dominant contributions to decoherence in our design. The first is acoustic radiation loss into the surrounding substrate. This can be simulated and is found to be in the range $\kappa_{\text{rad}}/2\pi \sim 1-10$kHz for all modes in Fig. 6.6, with $\kappa_{\text{rad}}/2\pi = 2.3$kHz for the mode highlighted in Fig. 6.6c. The second is coupling to two-level systems (TLS), which in both lithium niobate [175] and silicon [162] has been shown to be the dominant decoherence mechanism for GHz-frequency acoustic cavities at single phonon level powers and milliKelvin temperatures. For mechanical piezo participation ratio ζ_m, the TLS induced decoherence rate can be estimated by $\kappa_{\text{TLS}} = \zeta_m\kappa_{\text{LN}} + (1-\zeta_m)\kappa_{\text{Si}}$. Using reported TLS-limited linewidths $\kappa_{\text{LN}}/2\pi \sim 100-300$kHz in lithium niobate [146, 175] and $\kappa_{\text{Si}}/2\pi \sim 5$kHz in silicon [162], and taking $\zeta_m = 2\%$, we estimate a TLS induced decoherence rate of $\kappa_{\text{TLS}}/2\pi \sim 10$ kHz. The total mechanical decoherence rate is then estimated to be in the range $\kappa_m/2\pi \sim 10-20$kHz.

6.5 Efficiency and Added Noise

To analyze the efficiency and noise of our design, we consider a pulsed scheme for microwave to optical state transfer on a transmon qubit connected to the transducer [10]. The qubit is first tuned on resonance with the mechanical mode for a time $t = \pi/g_{pe}$ to complete a microwave photon-phonon swap operation, and subsequently detuned far off-resonance. A red-detuned ($\omega_d - \omega_o = -\omega_m$) laser pulse is then used to upconvert this phonon into an optical photon. The intrinsic efficiency of such a pulsed scheme is simply given by $\eta_i = \eta_{pe}\eta_{om}$, where η_{pe} is the piezo-electric photon-phonon swap efficiency, η_{om} is the optomechanical phonon-photon conversion efficiency.

η_{pe} can be calculated from a master equation simulation of the qubit-mechanics system. Using $g_{pe}/2\pi$ = 2.5MHz, estimated $\kappa_q/2\pi$ = 60kHz from Section 6.2, estimated mechanics decoherence rate $\kappa_m/2\pi$ = 20kHz from Section 6.4, we find $\eta_{pe} = 0.95$. The optomechanical readout step determines both η_{om} and the dominant noise contribution to the transducer, which arises from optical absorption heating of the mechanical mode. For a laser pulse duration τ, η_{om} is given by [10]

$$\eta_{\mathrm{om}}(\tau) = \frac{\gamma_{om}}{\gamma_{om} + \kappa_m}(1 - e^{-(\gamma_{om}+\kappa_m)\tau}) \tag{6.4}$$

where $\gamma_{om} = 4g_{om}^2 n_o/\kappa_o$ is the optomechanical scattering rate, and n_o is the number of intracavity optical photons corresponding to peak power of the optical pulse. In principle, this efficiency may be unity in the limit $\tau \gg 1/(\gamma_{om} + \kappa_m)$ and $\gamma_{om} \gg \kappa_m$. However, optically-induced heating of the mechanical mode severely limits τ in order to maintain <1 added noise photon. This leads to a fundamental tradeoff between efficiency and added noise resulting from heating dynamics in optomechanical systems. Maximizing efficiency for a given level of added noise requires careful choice of pulse duration τ and optical power n_o.

The added noise phonons $n_m(\tau)$ during optical readout are thought to originate from optical excitation of material defect states which undergo phonon-assisted relaxation via the mechanical mode of interest [154, 176, 177]. The timescale τ_h for n_m to exceed 1 noise phonon depends strongly on n_o and is found to vary greatly in different devices. Experiments in low-loss ($\kappa_m \lesssim$ 10kHz) pure silicon OMC devices report $\tau_h \sim 1\mu$s [156, 162], whereas silicon OMCs integrated in a piezo-optomechanical transducer with κ_m = 1MHz report much shorter $\tau_h \sim$ 100ns [10]. This suggests the presence of additional sources of optically induced heating and mechanical damping in piezo-optomechanical transducers that are potentially correlated. Possible sources are optical absorption by the IDT electrodes, TLS-limited loss in the piezo region, and surface defects in the OMC region from additional steps in the transducer fabrication process. While the dynamics of optically induced heating in piezo-optomechanical devices is a subject of future studies, it is clear that a transducer design aimed at improving optomechanical readout efficiency and noise should make the acoustic mode involved in the transduction process as silicon-like as possible.

In the design presented above, we minimize the dimensions of the piezo cavity so that most of the energy in the mechanical mode lives in the OMC region. The estimated mechanical damping rates based on participation ratios of various regions and calculated optomechanical coupling rates are comparable to those realized in pure silicon OMCs. Therefore, we may approximate the heating dynamics of our design as similar to that reported in previous silicon OMC work [156]. Using this heating model, we estimate ~0.5 added noise photons for a pulse with $n_o = 45$ and $\tau = 500$ns. Using the previously estimated values $\kappa_m/2\pi = 10$kHz, $\kappa_o/2\pi = 800$MHz, and $g_{om}/2\pi = 725$kHz (s.t. $\gamma_{om}/2\pi = 120$kHz), we estimate a pulse with $n_o = 45$ and $\tau = 500$ns can achieve $\eta_{om} \sim 30\%$. Combined with $\eta_{pe} = 0.95$, we achieve an estimated intrinsic efficiency $\eta_i \sim 29\%$.

There are additional noise sources which we have not considered here such as photodetector dark counts and residual photons from the optical pump pulse. However, given the measured photon count rates for these noise sources in previous milliKelvin optomechanics experiments in our group, these noise sources are negligible compared to those from optical absorption heating discussed above.

The total efficiency of our device is given by $\eta = \eta_i \eta_k \eta_{ext}$, where $\eta_k = (\kappa_{o,e}/\kappa_o)$ determines the fraction of optical photons emitted into the coupling waveguide, and η_{ext} is the external photon collection efficiency. For $\kappa_{o,e} \approx \kappa_{o,i}$ (critical coupling) we have $(\kappa_{o,e}/\kappa_o) \approx 0.5$. In typical optomechanics experiments, η_{ext} is mainly determined by the fiber-to-device coupling efficiency, insertion loss of the optical pump filtering setup, and quantum efficiency of single photon detectors. In our typical experimental setup we estimate these factors are 0.6, 0.2, and 0.9, respectively and lead to $\eta_{ext} \sim 0.1$. The product of all three efficiency estimates above yields a total transducer efficiency $\eta \sim 1.5$ %.

Finally, we consider the expected repetition rate for the transduction sequence in the pulsed scheme described above. In previous work, this was limited to 100Hz by the ~10-ms timescale for quasiparticle (QP) relaxation in the aluminum transmon coupled to the transducer [10]. We expect that using niobium with QP relaxation timescale in the ~ns range [11, 12] will allow for repetition rates in the 10kHz range (more on this in Chapter 7). At this repetition rate and estimated total efficiency η ~1.5%, we expect a single photon count rate of ~ 150Hz and a photon coincidence rate of order 1Hz. The latter, which is the key figure of merit for second order intensity correlation measurements as well as heralded remote entanglement generation, indicates reasonable measurement times in the range of an hour for these experiments.

6.6 Conclusion

We have presented an optimized design for a wavelength scale piezo-optomechanical transducer suitable for on-chip coupling to a transmon qubit. We have independently simulated and optimized the design of a piezoacoustic cavity and an optomechanical crystal cavity, and hybridized their acoustic mode structure in a way which is highly robust to fabrication disorder. We emphasize that our choice of material platform and minimized piezoacoustic cavity dimensions allows us to design for high piezoelectric swap efficiency without significantly compromising qubit coherence, and with optomechanical readout efficiencies comparable to state-of-the-art 1D OMC devices. With the expected performance from this transducer design, experiments measuring quantum correlations in photons generated by the transducer as well as a demonstration of heralded remote entanglement between two transducer devices should be feasible on reasonable measurement timescales. Finally, we note that the efficiency, noise, and repetition rate of the above transducer design are expected to be limited by optomechanical heating rates. Future design improvements can be made by employing 2D optomechanical crystal cavities, which through better thermal conductivity to the substrate, have achieved higher optomechanical cooperativities at lower added noise [178]. Replacing the on-chip transmon qubit with a high-impedance microwave resonator can further increase piezoelectric coupling strength, and thereby improve the fidelity of the microwave photon-phonon swap operation. Such a transducer device could be connected to an off-chip qubit in a modular transducer, which alleviates performance restrictions from co-fabrication of qubits and transducers.

Chapter 7

NIOBIUM BASED TRANSMON QUBITS ON SILICON SUBSTRATES FOR QUANTUM TRANSDUCTION

7.1 Introduction

In Chapter 6, we discussed the design of our piezo-optomechanical transducer and the expected conversion efficiency and added noise of our device. Another important figure of merit of the transducer is its repetition rate. Since our transducer operates in pulsed mode, the repetition rate is simply the rate at which we can repeat the transduction pulse sequence. The transduction pulse sequence is shown in Fig. 7.1a. It begins with a XY pulse on the qubit that prepares the qubit in the desired state. Next the qubit frequency is tuned to be on resonance with the mechanical mode of the piezo-optomechanical transducer for a time t_{swap} such that the microwave excitation in the qubit is exchanged for a phonon in the mechanical mode. The qubit is then detuned from the mechanical mode. Next a red-detuned optical pump pulse converts the phonon into and optical photon which is subsequently detected on a photodetector. This optical pulse consists of ~ 200THz frequency optical photons which have energy larger than the superconducting gap of typical superconducting materials. Since our superconducting qubit is in close proximity to our piezo-optomechaical transducer, absorption of these highly energetic optical photons can break Cooper pairs in the superconductor creating excess quasiparticles (QPs). Tunneling of these non-equilibrium quasiparticles across the Josephson junction of a superconducting qubit creates excess loss in the qubit [179] leading to a transducer dead time until the excess quasiparticles relax either by recombination to form a Cooper pair with the emission of a phonon or via an electron-phonon scattering process [180]. This quasiparticle relaxation time in general is a material and substrate dependent property. For the all-aluminum (Al) qubits on a silicon-on-insulator substrate used in the transducer device demonstrated in [10], the qubit recovery time after the optical generation of quasiparticles was on the order of ~10ms (see Fig. 7.1)b. Other measurements of quasiparticle relaxation in Al based superconducting circuits have also indicated relaxation times on the order of ~ ms [181, 182]. Niobium (Nb) is another commonly used superconducting material with much shorter measured quasiparticle relaxation times (~ns) [11, 12]. However junctions with a Nb/NbOx/Nb stack have been found to have poor quality compared to junctions utilizing an AlOx tunnel barrier [183]. In this chapter, we design and fabricate Nb-based transmon qubits with Al/AlOx/Al tunnel junctions on a silicon substrate and measure their recovery time when exposed to optical illumination.

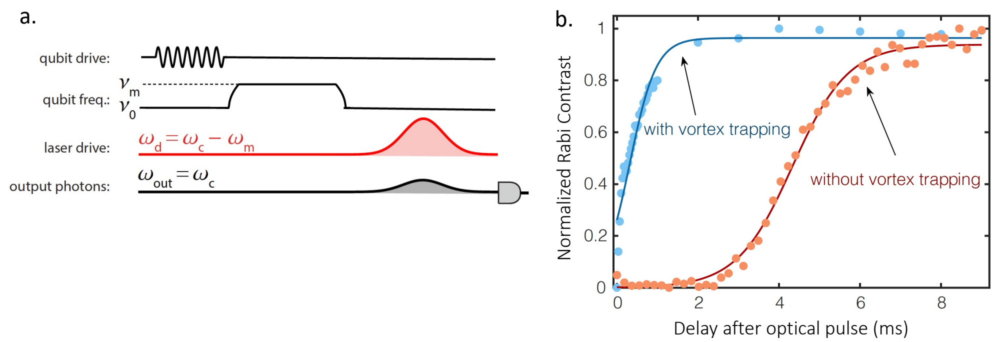

Figure 7.1: **Pulse sequence and laser induced quasiparticle recovery for a quantum transducer device. a.** Pulse sequence and **b.** Laser induced quasiparticle recovery for a quantum transducer device. Figure reprinted by permission from Springer Nature Customer Service Center GmbH: Springer Nature, *Nature*, Ref. [10], ©2020

.

7.2 Qubit Design

An optical image of our Niobium (Nb) based transmon qubit on a silicon substrate is depicted in Figure 7.2. An interdigitated capacitor patterned from Nb forms the shunt capacitance of the transmon. A pair of identical Al/AlOx/Al Josephson junctions form a SQUID loop that allows frequency tuning of the qubit. 'Bandage' layers made of Nb electrically contact the Al leads of the Josephson junctions to the underlying Nb layer. The qubit is capacitively coupled to a lumped element readout resonator. There is a single microwave co-planar waveguide (CPW) that is capacitively coupled to both the readout resonator and the transmon qubit and serves to interrogate the readout resonator as well as excite the qubit. The readout resonator, CPW, and ground plane are all fabricated from niobium (Nb). Note there is no on-chip Z-line for flux tuning the frequency of the qubit. Instead an external DC biased coil placed several millimeters above the chip is used to apply a magnetic field to the qubit for frequency tuning. The designed qubit parameters are listed in Table (7.1).

7.3 Device Fabrication

This section lists the fabrication steps for realizing a Nb based transmon qubit with Al/AlOx junctions on a 1cmx1cm Si chip. The process is split into 3 layers.

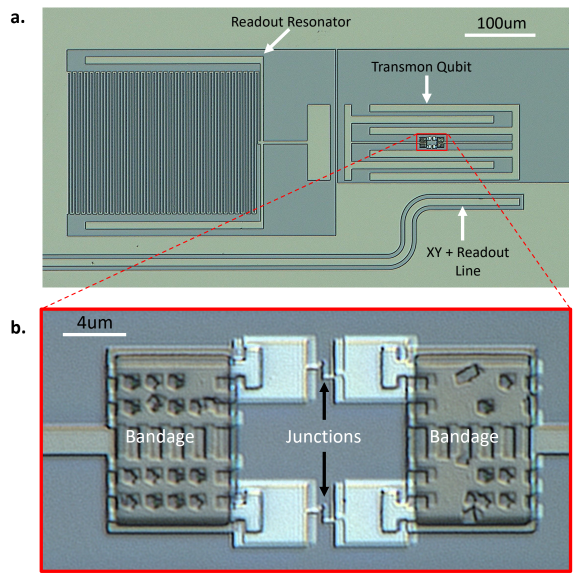

Figure 7.2: **Optical image of Niobium transmon qubit on silicon. a.** Optical image of a fabricated niobium device on silicon consisting of a readout resonator, transmon qubit and XY + readout line. **b.** Zoomed-in optical image of the SQUID loop showing the Josephson junctions and the 'bandage' layer for electrical contact between the aluminum and niobium layers. Light blue areas are aluminum. Grey areas are niobium.

Parameter	Designed Value
Qubit Frequency	5.5GHz
Readout Frequency	7.4GHz
Qubit Capacitance	73fF
E_J/E_C	70
Qubit Readout Coupling	80MHz
Qubit XY Coupling	<5kHz

Table 7.1: Qubit design parameters

Layer 1: This layer defines the markers for lithographic alignment, ground plane, qubit capacitor, readout resonator, and CPWs. All these features are fabricated from Nb. The steps for this layer are detailed below:

1. <u>Chip Cleaning</u>
   - Acetone 5min sonication
   - IPA 5min sonication
   - N_2 blow dry
   - O_2 plasma ash at 150W, 12sccm O_2 flow for 2min
   - 15s dip in 10:1 Buffered HF followed by 2x 10s DI H_20 rinse

2. Spin/Bake
   - Pre-bake at 180°C for 3min
   - Spin ZEP 520a at 3000 rpm for 1 min
   - Post-bake at 180°C for 3min
3. E-Beam Lithography
   - Beam current 50nA
   - Fracturing resolution 20nm
   - Dose 230 $\mu C/cm^2$
4. Development
   - ZED N50 for 2.5min
   - MIBK for 30s
   - N_2 blow dry
   - O_2 plasma ash at 150W, 12sccm O_2 flow for 2min
5. E-beam Evaporation of Nb
   - 15s BOE dip just before loading in evaporator to strip native oxide
   - Evaporate 150nm thick Nb at 0.4nm/s
6. Lift-off
   - NMP at 150°C for 2hr
   - Acetone 5min sonication
   - IPA 5min sonication
   - N_2 blow dry
   - O_2 plasma ash at 150W, 12sccm O_2 flow for 2min
   - 15s dip in 10:1 Buffered HF followed by 2x 10s DI H_20 rinse

At this stage, we have used e-beam lithography, e-beam evaporation, and metal lift-off to define our Nb circuit which forms layer 1.

Layer 2: In the second layer we will define our Al/AlOx Josephson Junctions. We use a Dolan bridge technique utilizing a bi-layer resist stack and angled e-beam evaporation to define the junctions. The steps are:

1. Spin/Bake
   - Pre-bake at 170°C for 3min
   - Spin Copolymer MMA EL-11 at 2200 rpm for 1 min
   - Bake at 170°C for 3min
   - Spin PMMA 950 A4 at 2200 rpm for 1 min
   - Post-Bake at 170°C for 3min
2. E-Beam Lithography
   - Beam current 1nA
   - Fracturing resolution 2nm
   - Base Dose 940 $\mu C/cm^2$, relative dose = 0.48
3. Cold Development
   - 3:1 IPA:DI H_20 for 90s at 10°C with stirring at 500rpm
   - IPA for 10s at 10°C with stirring at 500rpm
   - N_2 blow dry
   - O_2 plasma ash at 150W, 12sccm O_2 flow for 20s
4. Angled E-beam Evaporation of Al with in-situ oxidation
   - 15s BOE dip just before loading in evaporator to strip native oxide
   - Evaporate 60nm thick Al at 1nm/s, 40° angle from normal
   - Static oxidation at 10mbar O_2 pressure for 20mins
   - Evaporate 120nm thick Al at 1nm/s, -20° angle from normal
5. Lift-off
   - NMP at 150°C for 2hr
   - Acetone 5min sonication
   - IPA 5min sonication
   - N_2 blow dry
   - O_2 plasma ash at 150W, 12sccm O_2 flow for 2min
   - No BHF dip as BHF reacts with Al. No anhydrous vapor HF (VHF) either since VHF attacks Nb.

Now we have our Nb circuit with Al junctions.

Layer 3: The final layer is layer 3 where we use bandages to electrically connect the Al layer to the Nb layer. The bandages are essentially rectangles of Nb that connect the Al and Nb layers and are deposited via e-beam evaporation with an in-situ Ar mill to remove any native oxide from the surface to make good electrical contact. The steps are:

1. Spin/Bake
   - Pre-bake at 180°C for 3min
   - Spin ZEP 520a at 3000 rpm for 1 min
   - Post-bake at 180°C for 3min
2. E-Beam Lithography
   - Beam current 50nA
   - Fracturing resolution 20nm
   - Dose 230 $\mu C/cm^2$
3. Development
   - ZED N50 for 2.5min
   - MIBK for 30s
   - N_2 blow dry
   - O_2 plasma ash at 150W, 12sccm O_2 flow for 2min
4. E-beam Evaporation of Nb
   - In-situ Ar mill with beam voltage 400V, accelerator voltage 80V and beam current 21.6mA for 6mins
   - Evaporate 150nm thick Nb at 0.4nm/s
5. Lift-off
   - NMP at 150°C for 2hr
   - Acetone 5min sonication
   - IPA 5min sonication
   - N_2 blow dry
   - O_2 plasma ash at 150W, 12sccm O_2 flow for 2min

7.4 Experimental Setup

The measurements of the fabricated Nb-based qubit chip are performed in a dilution refrigerator at a base temperature of T = 10 mK. The chip is wirebonded to a printed circuit board (PCB) with multiple 50 Ω co-planar waveguides. Each co-planar waveguide on the PCB is wirebonded to a corresponding co-planar waveguide on chip which is used to both excite and readout the qubit. Microwave connectors soldered to one side of the PCB allow microwave signals to be sent to the device. The opposite side of the PCB is cut right to the edge of the chip to allow for a lensed optical fiber to be placed in close proximity to the chip. A 3-axis positioner is used to precisely position the optical fiber at a height 200um above the plane of the qubit and a distance of 2mm from the qubit (Fig. 7.3). This geometry is intended to mimic the scattered light in our transducer device. A 1550nm laser is used to illuminate the chip via the lensed optical fiber. An acousto-optic modulator (AOM) allows pulsing of the laser and is used to control both the duration and repetition rate of the pulse. Microwave signals are generated and read out using the techniques described in Chapter 1. A digital delay generator is used to maintain synchronization between the optical and microwave pulses. A hand-wound coil made from Nb-Ti superconducting wire mounted a few millimeters above the chip is used to generate a magnetic field to tune the frequency of the qubit. DC current is applied to the coil using a low noise DC source.

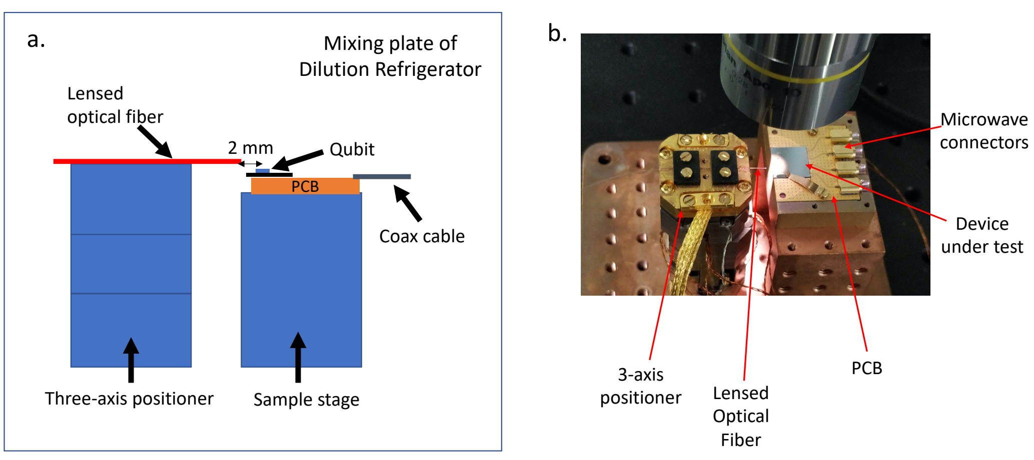

Figure 7.3: **Experimental setup for optical tests on Nb transmon qubits. a.** Schematic and **b.** Photograph of the experimental setup on the mixing plate of a dilution refrigerator

7.5 Qubit Characterization

We begin by locating the readout resonator by performing a reflection measurement using a vector network analyzer (VNA). Once we have located the readout resonator, we locate the qubit, tune the qubit frequency at a desired detuning from the readout resonator and proceed to characterize the qubit in the absence of optical illumination. We perform standard lifetime (T_1) and coherence time (T_2^*) measurements, the results of which are shown in Fig 7.4.

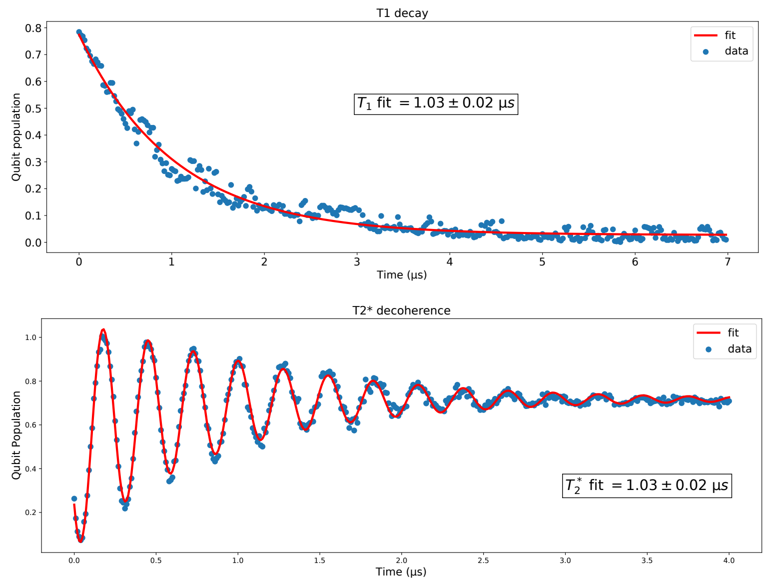

Figure 7.4: T_1 **and** T_2^* **time constants of a niobium qubit on silicon.**

7.6 Qubit Response to Optical Illumination

Next we turn our attention to measurements with optical illumination. Since we will be inferring the qubit response by monitoring the readout resonator spectrum, we must first characterize the bare readout resonator response under optical illumination. By sufficiently detuning the qubit from the readout resonator the qubit can be effectively decoupled from the readout resonator. This allows us to characterize the optical response of the readout resonator without the influence of the qubit. We perform spectroscopy on the readout resonator as we apply a 100 ns long, 85 μW peak power laser pulse at a repetition rate of 10 kHz. The result of this measurement is shown in Fig **??**. Clearly, there is no measurable change in the spectrum of the readout resonator after the laser pulse. This is as expected since the readout resonator is made entirely of Nb which has a very fast QP response.

Now we flux bias the qubit to be 320 MHz detuned from the readout resonator. We

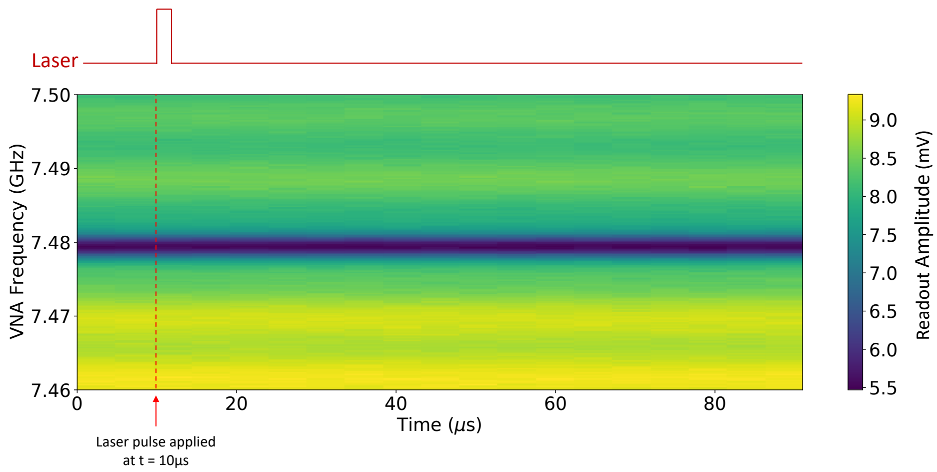

Figure 7.5: **Readout resonator spectroscopy under optical illumination**

probe the amplitude of the readout signal as an XY drive tone is swept around the qubit frequency. When the XY drive frequency is on resonance with the qubit frequency, the qubit is excited and the readout amplitude changes (in our measurement this appears as a dip in the readout amplitude). We use this technique to monitor the qubit frequency as we apply a 100 ns laser pulse at a 5 kHz repetition rate and peak power 240 μW. The result of this measurement is shown in Fig **??**.

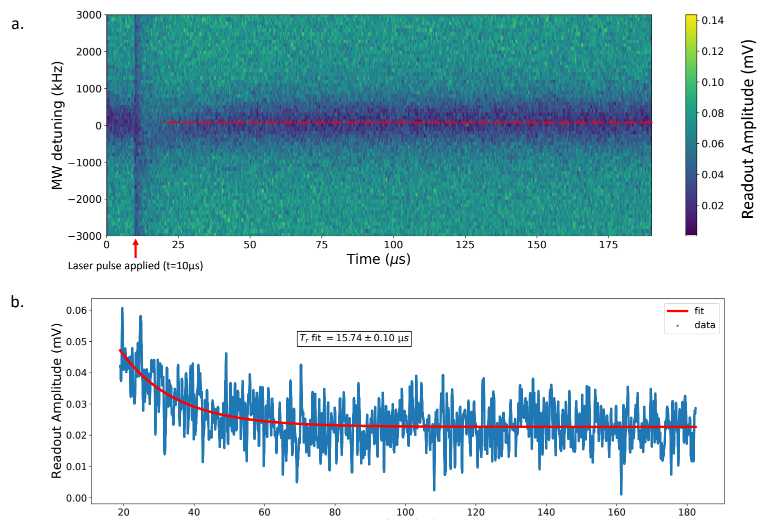

Figure 7.6: **Spectroscopy of Nb qubit under optical illumination.** **a.** Spectroscopy of Nb Qubit under optical illumination. **b.** Line-cut at 0 detuning showing recovery of the readout amplitude. Fitting to an exponential yields a recovery timescale of 15.7 μs. Measurements performed with 100 ns laser pulse, 5 kHz repetition rate and 240 μW peak power.

We observe a sharp change in the qubit spectrum as the laser is pulsed. In particular, at t = 10 μs when the laser is turned on, there is a downshift of the qubit frequency and a corresponding increase in the amplitude of the readout signal. As the delay from the laser pulse increases, the readout amplitude and qubit frequency relax back to their steady state value. A line cut at 0 microwave detuning shows the recovery of the readout signal. We find this recovery process fits well to an exponential with a relaxation time constant of 15.7 μs.

In the above measurement, we are probing the qubit by applying a continuous wave (CW) microwave signal to the XY drive line. We now utilize pulsed microwave signals on the XY line to measure the population, energy decay rate ($\gamma_1 = \frac{1}{2\pi T_1}$) and decoherence rate ($\gamma_2^* = \frac{1}{2\pi T_2^*}$) of the qubit as a delay from the laser pulse. A set of these measurements performed at a 10 kHz repetition rate with a 100 ns laser pulse and a peak laser power of 85 μW is shown in Fig. 7.7.

Focusing on the population measurement, (Fig. 7.7a.), we observe the laser pulse initially inducing some excess population in the qubit which then relaxes to a steady state value on a timescale of $\sim$ 30 μs. We also note that the steady state population ($P_{e,SS}$) is higher than the thermal population in the laser off case (indicated by the gray line). Measurements of the energy decay rate (γ_1) and the decoherence rate (γ_2^*) show a similar fast recovery timescale on the order of $\sim$ 10 μs and an excess decoherence rate in the steady state ($\gamma_{2,SS}^*$) due to a process slower than the repetition period (100 μs).

To gain further insight into this slow process, we measure the steady state population ($P_{e,SS}$) and decoherence rate ($\gamma_{2,SS}^*$) of the qubit at a delay of 81 μs from the laser pulse while sweeping the peak power of the laser pulse. The results are shown in Fig. 7.8.

We fit the steady state population at each laser power to a Boltzmann distribution $n_{th}(T_{eff})$ with an effective temperature T_{eff}. We find that this effective qubit temperature scales linearly with peak laser power in the low power regime $T_{eff}(P) = T_{off} + \beta P$, with T_{off} = 126 mK and β = 1.6 ± 0.097 mK/μW. We find a similar linear scaling of the decoherence rate of the qubit as a function of laser power (P), $\gamma_{2,SS}^*(P) = \gamma_{2,off} + \beta P^n$, with $n = 1.03 \pm 0.17$ and $\beta = 0.53 \pm 0.41$ kHz/μW^n.

We further probe the dependence of the steady state population $P_{e,SS}$ as a function of repetition rate and laser pulse duration Fig. 7.9. We find that the population fits well to a Boltzmann distribution with an effective temperature that scales linearly in

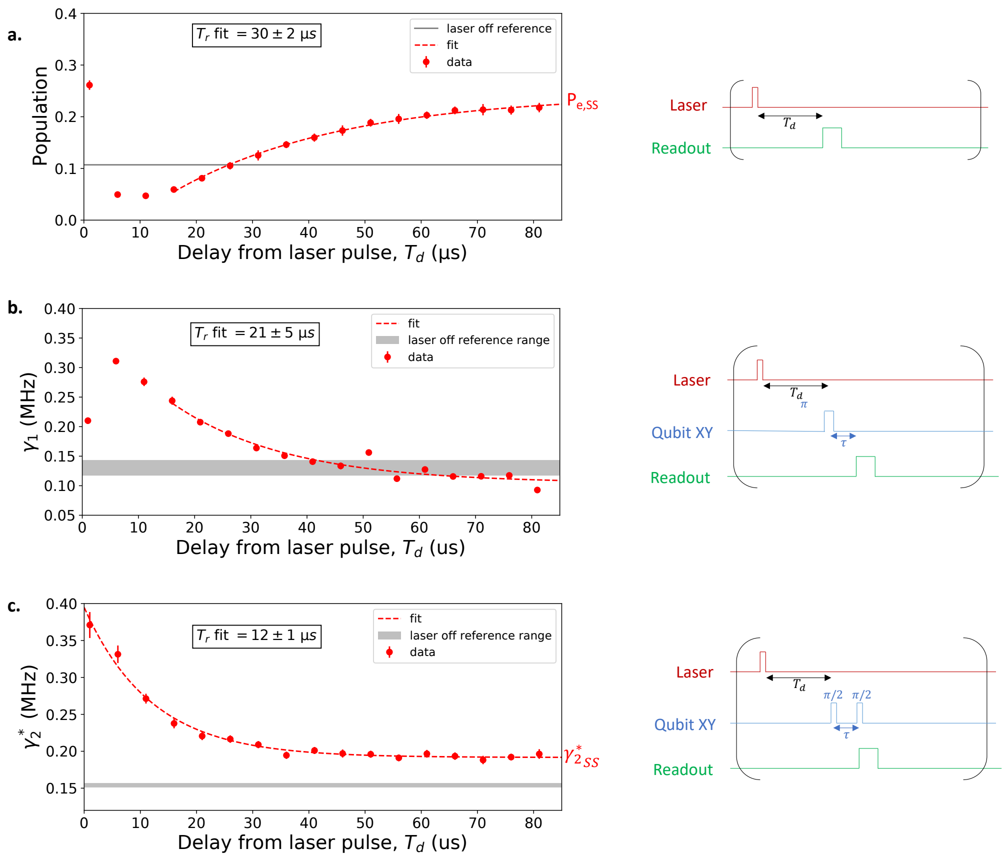

Figure 7.7: **Recovery of niobium qubit after laser illumination. a.** Qubit excited state population, **b.** energy decay rate (γ_1), and **c.** decoherence rate (γ_2^*) versus delay, T_d from a 100 ns long laser pulse (peak power: 85 μW, repetition rate: 10 kHz). Gray line indicates a reference measurement with the laser off. Dashed line is an exponential fit indicating a recovery time, T_r. With the laser on, the steady state population ($P_{e,SS}$) and decoherence ($\gamma_{2,SS}^*$) is higher than the laser off value (gray line). The right column shows the corresponding pulse sequences used for each measurement.

both repetition rate and laser pulse duration. Our results indicate a trade-off between power, repetition rate, and pulse duration. For a given pulse duration, we can use higher peak laser powers by operating at lower repetition rates.

So far we have been focusing on the qubit population and decoherence at long delays (81 μs) from the laser pulse. We also investigate the effect on the qubit decoherence rate when the laser pulse is applied *during* a Ramsey pulse sequence on the qubit. The pulse sequence for this measurement is shown in the inset of Fig. 7.10. We time the laser pulse to arrive just after the first $\frac{\pi}{2}$ pulse of the Ramsey sequence and probe the effect of the laser pulse on the decoherence rate of the qubit as a function of peak laser power (Fig.7.10a.) and repetition rate (Fig.7.10b.). Even at a high repetition rate of 50 kHz, we find a range of powers upto a few μW where the qubit is able to

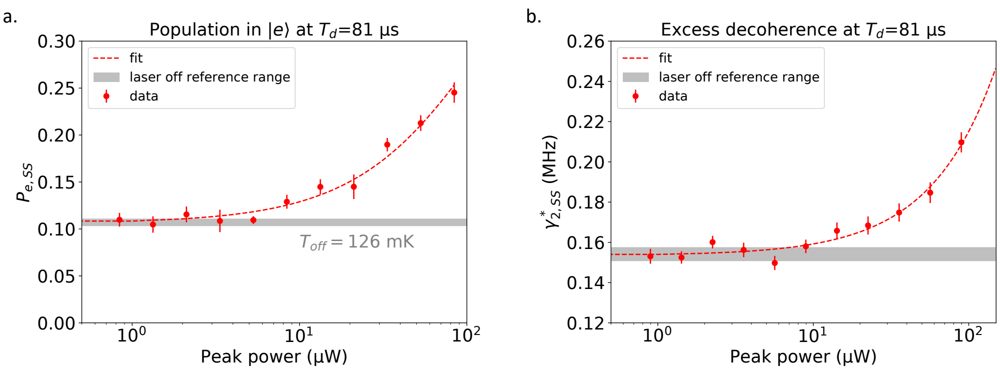

Figure 7.8: **Dependence of qubit population and decoherence on peak optical power.** Dependence of **a.** steady state excited state population, $P_{e,SS}$ and **b.** decoherence rate, $\gamma^*_{2,SS}$ of Nb qubit as a function of peak laser power (P). Experimental sequence is repeated at 10 kHz repetition rate. Horizontal gray regions indicate laser off values up to one standard deviation. Dashed line in **a.** is a fit to $n_{th}(\beta P)$, where $n_{th}(T)$ is the Boltzmann distribution assuming a two level system with temperature T. Dashed line in **b.** is a fit to the expression $\gamma_{2,off} + \beta P^n$.

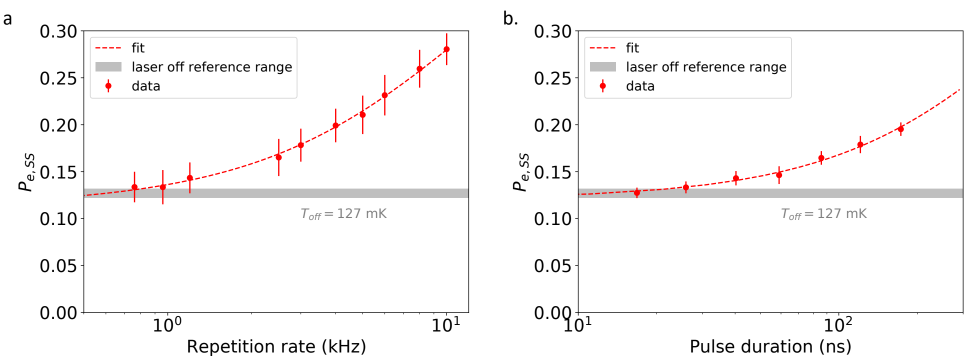

Figure 7.9: **Dependence of qubit population on repetition rate and optical pulse duration.** Steady state excited population $P_{e,SS}$ as a function of **a.** Repetition rate (R) (Peak power = $89\mu W$; pulse duration = 100 ns) and **b.** Laser pulse duration (D) (Peak power = 9.5 μW; Repetition rate = 10 kHz). Horizontal gray regions indicate laser off values up to one standard deviation. Dashed line in **a.** is a fit to a Boltzmann distribution $n_{th}(T_{eff})$, where $T_{eff}(R) = T_{off} + \beta R$, with $\beta = 16.9 \pm 0.34$ mK/kHz. Dashed line in **b.** is a fit to a Boltzmann distribution $n_{th}(T_{eff})$, where $T_{eff}(D) = T_{off} + \beta D$, with $\beta = 0.36 \pm 0.0017$ mK/ns.

maintain coherence after the laser pulse. There is a trade-off between repetition rate and peak laser power to maintain qubit coherence.

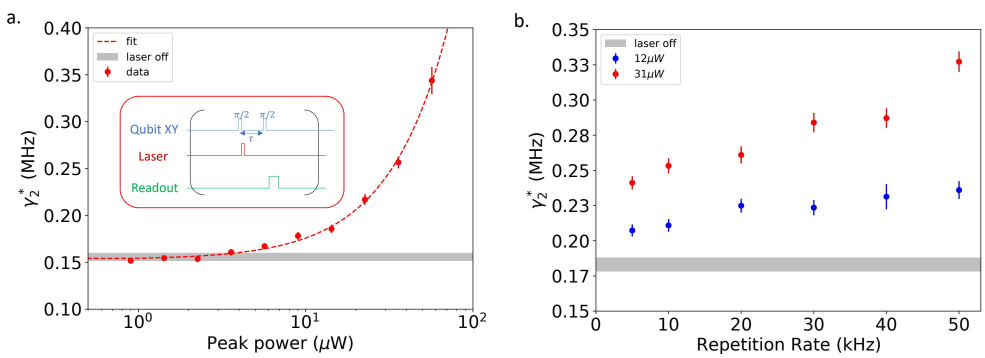

Figure 7.10: **Ramsey measurement interrupted by a laser pulse.** Decoherence rate extracted using a Ramsey sequence interrupted by a laser pulse as a function of **a.** Peak laser power (Repetition rate = 50 kHz) and **b.** Repetition rate. Horizontal gray regions indicate laser off values up to one standard deviation. Inset of **a.** shows the pulse sequence used in both measurements. Pulse duration was 100 ns for both measurements. Dashed line in **a.** is a fit to $\gamma_2^*(P) = \gamma_{2,off} + \beta P^n$, where P is peak power. $\beta = 1.42 \pm 0.32$ kHz/μW^n and $n = 1.2 \pm 0.1$.

7.7 Conclusion

In conclusion, our measurements of the population, lifetime and decoherence rate of a niobium qubit with aluminum/aluminum-oxide/aluminum junctions on a silicon substrate indicate that these qubits have an initial fast ($\sim 10\mu s$) recovery time when exposed to optical illumination. We also find evidence of a slower process that creates excess population and decoherence on a $\sim ms$ time scale. Power-dependent measurements indicate this slower process is likely thermal in origin. We find a trade-off between power and repetition rate where operating at lower repetition rates allows higher peak laser powers. Crucially, there is a range of powers upto 10 μW where we do not have significant excess population or decoherence induced by a 100 ns laser pulse upto a repetition rate of 10 kHz. Given that the transducer device in [10] operates at 2 μW power with <100 ns pulse lengths, our measurements indicate that a repetition rate of 10 kHz would be achievable by replacing the all Al qubits in the device in [10] with hybrid Nb-Al qubits. This would be a 100x improvement over the repetition rate of 100 Hz reported in [10]. However it is important to keep in mind that the experiments performed in this chapter involved using a lensed optical fiber to illuminate the entire qubit chip. In a real transducer device, the lensed fiber would couple light into an on-chip optical waveguide which would be routed to an optomechanical crystal cavity that is in close proximity to the qubit. This could change the effective optical power seen by the qubit. To test this, it is necessary to pattern optomechanical crystals on chip along with the Nb qubit for which we need to move to a silicon-on-insulator substrate. This poses some fabrication challenges which form the subject of the next chapter.

Chapter 8

TOWARDS FABRICATING NIOBIUM BASED QUBITS ON SILICON-ON-INSULATOR SUBSTRATES

In the previous chapter, we studied the optical response of niobium (Nb) based transmon qubits with aluminum/aluminum-oxide/aluminum junctions fabricated on a silicon substrate. Our results showed a favorable quasiparticle recovery time for these niobium based qubits compared to the all aluminum transmon qubits used in [10]. However, as discussed in Chapter 6, our transducer device is designed to be fabricated on the device layer of a silicon-on-insulator (SOI) substrate. To integrate our Nb-based transmon qubits with our piezo-optomechanical transducer device, we need to develop a fabrication process for realizing Nb qubits on SOI. In this chapter we discuss some of the challenges associated with fabricating Nb-based microwave circuits on SOI substrates and describe some initial steps towards realizing Nb-based transmon qubits on SOI.

8.1 Fabrication Challenges

A fabrication process for realizing **aluminum (Al)** transmon qubits on SOI is outlined in [78] and reproduced in Fig 8.1. This process relies on e-beam evaporation and metal lift-off to pattern the microwave circuit on the silicon device layer of a silicon-on-insulator substrate. This is followed by release of the device layer by etching away the buried oxide layer using anhydrous hydrofluoric acid (VHF) in vapor form—a step we will refer to as 'VHF release'. It is crucial to etch away the buried oxide layer everywhere underneath the microwave circuit as the oxide is a lossy dielectric and can contribute significantly to microwave losses. Since the size of a typical circuit consisting of a transmon qubit and associated readout resonator and control lines is on the order of ~100s of μm, this results in large (~mm sized) released membranes. While this process works well for aluminum on SOI, niobium films deposited via e-beam evaporation are under considerably higher tensile stress [184, 185]. This makes release of large area membranes challenging as the high tensile stress tends to crack and break the membranes. Further, unlike Al, Nb reacts with anhydrous hydrofluoric acid, and hence must be protected during the VHF release step.

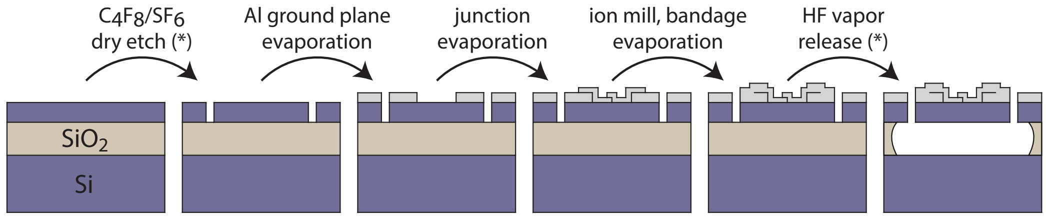

Figure 8.1: **Fabrication process for Al transmon qubits on SOI.** Figure reproduced from [78].

8.2 Development of a Sputtering Process for Niobium Thin Films

Since e-beam evaporation produces highly tensile films, we need a deposition technique that allows us to control the stress of the deposited film. An alternative to e-beam evaporation is sputter deposition. Sputtering works by bombarding a metal target with highly energetic ions (typically Ar ions) to eject target material that then condenses on the surface of the substrate forming a thin film. Sputtering allows considerable control over the deposition parameters, which can be tuned to change the stress of the deposited film. In particular, controlling the sputtering chamber pressure has been shown to be a convenient way of tuning the stress of Nb thin films deposited via DC magnetron sputtering using argon ions [186].

We utilize an AJA ATC Orion 8 UHV sputtering system for sputtering our Nb film. It is routinely capable of achieving low E-9 torr pressures ensuring high quality of the sputtered film. We perform DC magnetron sputtering using a 2 inch Nb target. The sputtering parameters are listed in Table 8.1

Parameter	**Value**
DC Power	300 W
Ar Flow Rate	20 sccm
Process Pressure	Varied to tune stress
Substrate Temperature	Room temperature
Substrate Rotation	10 rpm
RF Stage Bias	Not applied

Table 8.1: Nb sputtering parameters

We tune the process pressure to tune the stress of the deposited film. We utilize stylus profilometry to measure the bow of a 4 inch test grade silicon wafer before and after sputter deposition of a 150 nm thick Nb film. We calculate the radius of curvature from the measurement of the bow as $R = r^2/2\delta$, where R is the radius of curvature, δ is the bow of the wafer, and r is the radius of the substrate. The stress of the deposited film can then be calculated using Stoney's equation [187, 188].

$$\sigma = \frac{1}{6}\left(\frac{1}{R_{post}} - \frac{1}{R_{pre}}\right)\frac{E}{(1-\nu)}\frac{t_s^2}{t_f} \tag{8.1}$$

where,
σ = stress in deposited film
R_{post} = radius of curvature of substrate post deposition
R_{pre} = radius of curvature of substrate pre depostion
E = Young's modulus of substrate
ν = Poisson's ratio of substrate
t_s = substrate thickness
t_f = thickness of deposited film

In Fig. 8.2, we plot the stress of the deposited 150 nm Nb film as a function of sputtering process pressure. Similar to [186], we see an initial compressive stress at low sputtering pressures, which becomes increasingly tensile as we increase the process pressure. Crucially, there is a 0 crossing of the stress at low process pressures allowing us to tune the stress of our film to be near 0. In practice, we want our Nb film to have a small amount of tensile stress to compensate for the compressive stress in the silicon device layer of our SOI substrate. We target a tensile stress of ~200 MPa which is achieved at a sputtering pressure of 3.9 mTorr.

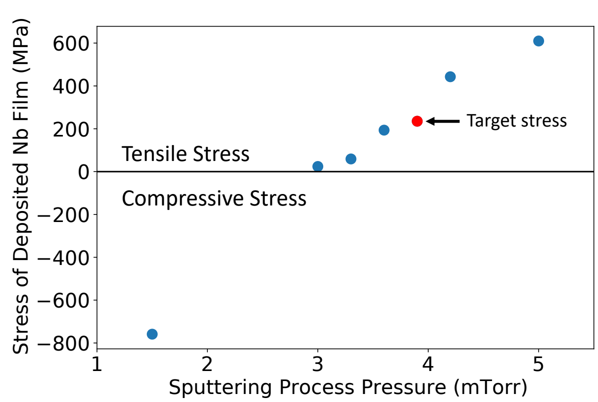

Figure 8.2: **Stress of a 150 nm thick Nb film sputtered on a Si substrate as a function of sputtering process pressure.**

8.3 Development of an Etching Process for Niobium Thin Films

Sputter deposition produces conformal coatings, that coat the sidewalls of features which makes metal lift-off difficult. As a result, we need to find an alternative technique for patterning the sputtered thin films. We utilize reactive ion etching (RIE) to pattern our sputtered Nb films. In this process, a chemically reactive plasma (utilizing a fluorine based chemistry) is used to etch the Nb film. Since our Nb film sits on a thin (220 nm) silicon device layer, care must be taken to ensure we can stop the etch without over-etching too deep into the silicon device layer. Further, since our eventual goal is to use these fabrication techniques to develop an integrated transducer with niobium qubits and a lithium niobate on SOI piezo-optomechanical device, we need to ensure that the etch selectively etches Nb without etching lithium-niobate.

We utilize an Oxford Instruments Plasmalab 100 ICP-RIE 380 system to etch our Nb films. Niobium can be etched in a variety of fluorine based [166, 189, 190] and chlorine based [167, 191] chemistries. However fluorine and chlorine based chemistries are known to etch silicon too. To minimize the silicon etch rate, we utilize a C_4F_8/O_2 chemistry. This is inspired by [192] where this chemistry is used for selectively etching SiO_2 while minimizing the etch rate of silicon. Our optimized Nb etch parameters are listed in Table 8.2. The corresponding etch rates of niobium, silicon, and lithium niobate (-Z-cut) are listed in Table 8.3. The etch rate of silicon is about 24 nm/min. This is slow enough that we can afford to over-etch the Nb by about 1 min and only thin down the Si device layer by $\sim$ 20 nm. We utilize thin film ellipsometry as feedback to precisely time the etch and prevent larger over-etching into the Si device layer.

Parameter	**Value**
ICP Power	750 W
RF Power	150 W
C_4F_8 Flow	40 sccm
O_2 Flow	3 sccm
Temperature	15 C
Process Pressure	8 mTorr
Helium Backing Pressure	4 torr

Table 8.2: Nb etching parameters

Our mask for the niobium etch is 10 nm thick alumina deposited via atomic layer deposition (ALD-alumina). The alumina mask itself is patterned by a physical argon ion based ICP-RIE etch utilizing ZEP 520a resist as a mask (parameters listed in

Material	Etch Rate
Niobium	15-25 nm/min
Silicon	24nm/min
Lithium Niobate	3.4nm/min
ALD Alumina	0.1-0.2 nm/min

Table 8.3: Etch rates of various materials in the Nb etch

Table 8.4). ALD-alumina exhibits a selectivity of ~ 100:1 over Nb for our chosen Nb etch chemistry—making it a suitable masking material (see Table 8.3 for ALD-alumina etch rate in C_4F_8/O_2 chemistry). It can easily be removed post etching with a short (~ 1 min) buffered HF dip.

Parameter	Value
ICP Power	500 W
RF Power	50 W
Ar Flow	20 sccm
Temperature	20 C
Process Pressure	10 mTorr
Helium Backing Pressure	4 torr
ALD Alumina Etch Rate	2nm/min

Table 8.4: ALD alumina etching parameters

We find that our chosen Nb etch chemistry causes some deposition on the sidewalls of the niobium features. A 10 min long O_2 plasma ashing followed by a 30s buffered HF dip serves to clear up the residue and reveals smooth, vertical sidewalls as shown in Fig. 8.3.

8.4 Protection of Nb Surface from VHF Attack

Finally, we need to address the issue of anhydrous vapor HF (VHF) reacting with the Nb surface. To protect the Nb from being exposed to VHF, we must mask the Nb with a mask that is impervious to VHF. Post the VHF release, we will have a large suspended membrane which makes removal of the masking material difficult as any solvent-based mask removal process will crack the membrane due to surface tension. Ideally we want a mask that does not need to be removed post VHF release. This mask should be thin enough that it does not greatly affect the quality factor and frequency of our microwave circuit. At the same time it should be able to conformally coat the sidewalls or our Nb features and be dense enough (pin-hole free) to be impervious to VHF.

Atomic layer deposited (ALD) alumina works well as a masking material for this

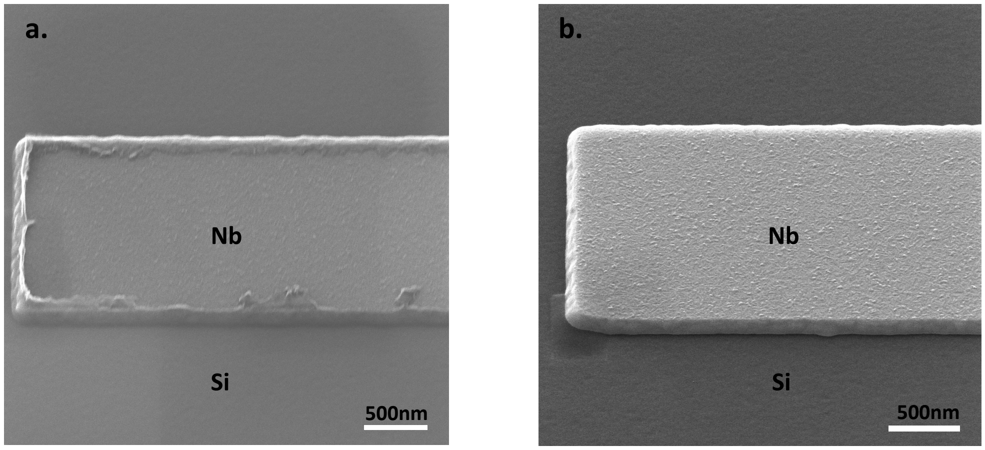

Figure 8.3: **He FIB image of etched Nb on Si. a.** Before and **b.** after O_2 plasma ashing and buffered HF clean.

purpose. Atomic layer deposition utilizes chemical precursors that sequentially react with the surface of the substrate in a self-limiting process to grow a thin film one layer at a time. It is a highly conformal process and can produce high quality, pin-hole free thin films with very precise control over film thickness.

We grow our alumina thin film in an Oxford Instruments Plasma Technology FlexAL II system utilizing a plasma assisted process at 300C with a trimethyl aluminum (TMA) precursor. We find a growth rate of 1.2 Å per cycle for this process. A 15 nm thick alumina film grown in this manner is found to be sufficient to act as a mask that protects the niobium surface from VHF attack. (Fig 8.4)

8.5 Quality of Sputtered and Etched Niobium Thin Films

Now that we have developed the individual steps for sputtering, etching and protecting the Nb film, we proceed to test the quality of the thin films produced using this fabrication process. For this purpose, we fabricate lumped element Nb microwave resonators on a Si substrate. We use an on-chip coplanar waveguide (CPW) to perform a reflection measurement and extract the intrinsic quality factor (Q_i) at cryogenic temperatures (~10 mK) and low (single photon) power levels. We chose silicon as our substrate for this test in order to enable comparison to similar e-beam evaporated resonators fabricated on Si in our lab. We find Q_i ~ 100,000 which is comparable to similar lumped element resonators fabricated via e-beam evaporation in our lab. The fabricated device and measurement results are shown in Fig. 8.5.

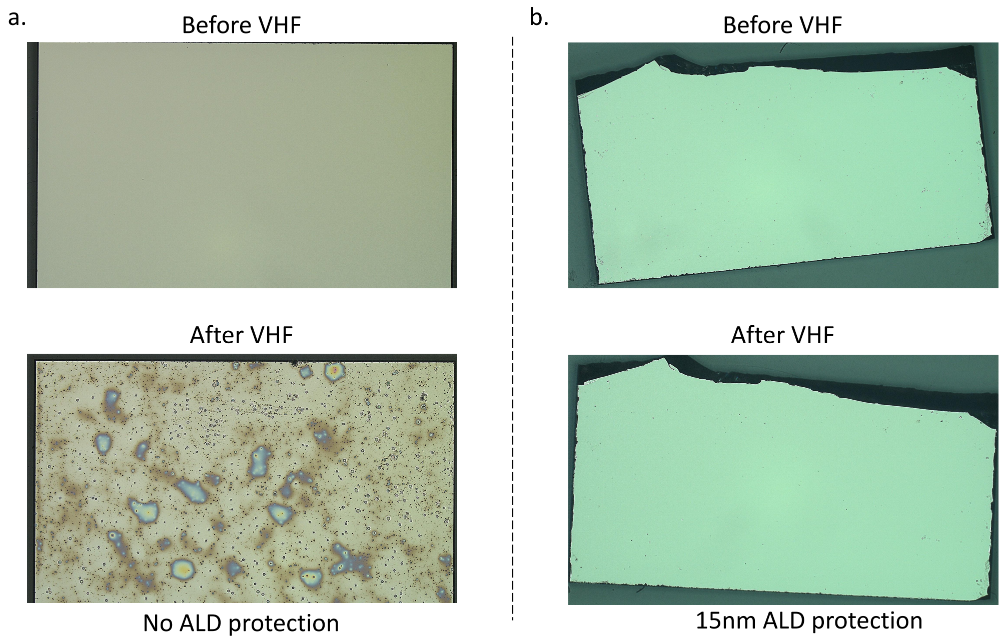

Figure 8.4: **Protection of Nb surface using ALD alumina.** Surface of Nb film before (upper panel) and after (lower panel) exposure to anhydrous vapor HF with **a.** no ALD protection layer and **b.** 15nm thick ALD protection layer.

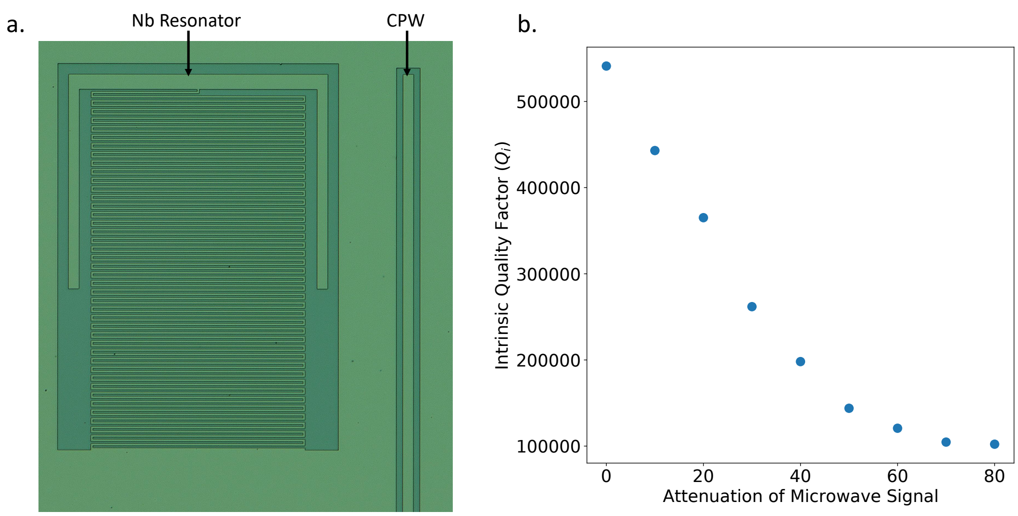

Figure 8.5: **Optical image and measured quality factor of Nb lumped element resonators. a.** Optical image of a fabricated Nb lumped element resonator on Si using the developed sputter and etch process **b.** Measured intrinsic quality factor (Q_i) as a function of microwave power.

8.6 Etch of VHF Release Holes

In the previous sections, we discussed the development of a sputter and etch process to fabricate high quality Nb-based superconducting circuits on the Si device layer of an SOI substrate. As mentioned in the introduction to this chapter, we need to etch away all the buried oxide underneath our Nb circuit to form a suspended Nb on Si membrane in order to reduce dielectric losses. We do this in a step called ‘release’, where we flow anhydrous hydrofluoric acid in vapor form (VHF) which selectively etches away the lossy silicon-oxide without attacking silicon. For this process to work, the VHF needs to be able to penetrate underneath the silicon device layer to attack the underlying oxide. To facilitate this, we pattern and etch an array of ~200 nm diameter holes with 4μm hole spacing in the silicon device layer. These holes are etched through the alumina, Nb, and Si layers and allow for vapor HF to penetrate through to the buried oxide layer and etch it away. We do this ‘HF holes etch’ in a single step using a thick (~ 800-900 nm) layer of ZEP 520a resist as an etch mask. First, to etch through the alumina layer, we use the Ar ion alumina etch with the parameters listed in Table 8.4. Once we have etched through the alumina layer, we switch to an ICP-RIE etch with SF_6/C_4F_8 chemistry (similar to the one used for aluminum transmon qubits on SOI in [78]). The SF_6/C_4F_8 etch serves to etch through both the Nb and Si device layers. The corresponding etch parameters are listed in Table 8.5.

Parameter	Value
ICP Power	1200 W
RF Power	23 W
SF_6 Flow	16 sccm
C_4F_8 Flow	40 sccm
Temperature	15 C
Process Pressure	10 mTorr
Helium Backing Pressure	4 torr

Table 8.5: VHF release holes etching parameters

8.7 Proposed Fabrication Process for Niobium Transmon Qubits on SOI

Having developed a sputter and etch process for Nb thin films and having tested the ALD alumina protection layer, we conclude this chapter by proposing a detailed fabrication process for realizing Nb based transmon qubits on SOI substrates. The process is schematically outlined in Fig. 8.6.

Layer 1: Markers, ground plane, qubit capacitor and CPWs:

1. Chip Cleaning
    - Acetone 5min sonication

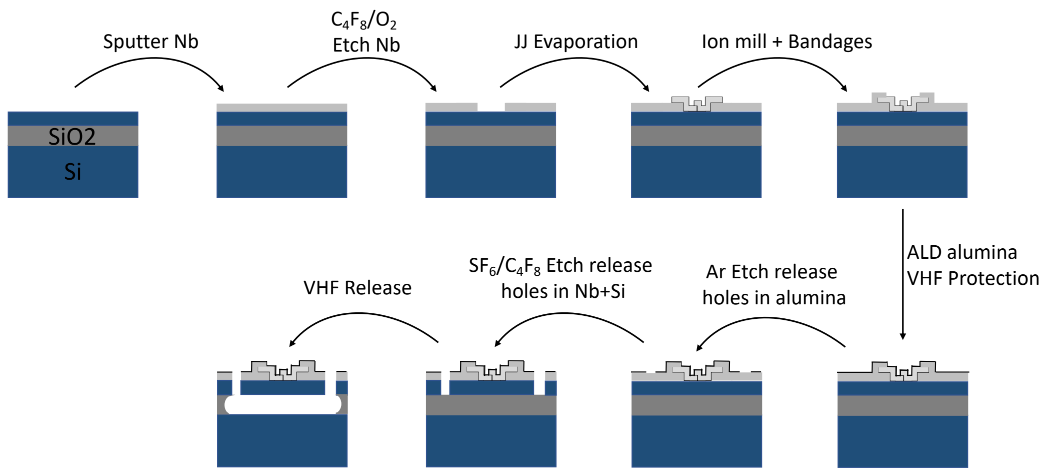

Figure 8.6: **Proposed fabrication process for Nb transmon qubits on SOI**

- IPA 5min sonication
- N_2 blow dry
- O_2 plasma ash at 150W, 12 sccm O_2 flow for 2min

2. Nb Sputter Deposition
    - 15s dip in 10:1 Buffered HF followed by 2x 10s DI H20 rinse—this step etches away the native silicon-oxide on the surface of the substrate and is done right before loading the chip in the sputterer for a clean oxide-free Nb-Si interface
    - Sputter 150 nm Nb at 3.9 mTorr process pressure and other parameters as listed in Table 8.1
3. ALD Deposition of Alumina Etch Mask
    - Deposit 10 nm alumina at 300°C
4. Spin/Bake
    - Pre-bake at 180°C for 3min
    - Spin ZEP 520a at 3000 rpm for 1min
    - Post-bake at 180°C for 3min
5. E-Beam Lithography
    - Beam current 50nA

- Fracturing resolution 20nm
- Dose 230 $\mu C/cm^2$

6. Development
   - ZED N50 for 2.5min
   - MIBK for 30s
   - N_2 blow dry
   - O_2 plasma ash at 150W, 12 sccm O_2 flow for 2 min
7. ICP-RIE Etching of Alumina Etch Mask
   - 6 min Ar ion etch of the alumina mask using parameters listed in Table 8.4. The etch rate is ~ 2nm/min, so we are over-etching by 1 min.
8. ICP-RIE Etching of Nb
   This step can be done right after the alumina etch without stripping of the ZEP 520a resist. The resist will just act as an additional mask on top of the alumina mask for this step.
   - 6-10 min C_4F_8/O_2 etch of Nb using parameters listed in Table 8.2. Use ellipsometry to determine etch stopping point. Aim to stop when ellipsometer shows 200 nm thick silicon device layer (20 nm over-etch into Si).
9. Etch Mask Removal
   - NMP at 150°C for 2hr
   - Acetone 5min sonication
   - IPA 5min sonication
   - N_2 blow dry
   - O_2 plasma ash at 150W, 12 sccm O_2 flow for 2min
   - 1min dip in 10:1 Buffered HF followed by 2x 10s DI H_20 rinse—the previous steps remove any surviving ZEP and then this 1min BHF step will remove the ALD alumina layer.

At this stage, we have used e-beam lithography, sputter deposition, and reactive ion etching to define our Nb circuit which forms layer 1.

The next layers are **Layer 2 (Josephson Junctions)** and **Layer 3 (Bandage Layer)**. The fabrication of these layers is identical to the process outlined in the previous chapter in section 7.3.

Layer 4: VHF release. In this layer, we will deposit a 15 nm thick ALD alumina layer for protection of the Nb surface from VHF. We will then pattern and etch an array of ~200 nm wide 'release holes' with ~4 μm spacing. These holes are punched through the alumina, Nb, and the Si device layers to allow anhydrous vapor HF access to the underlying buried oxide layer. Finally, we flow anhydrous HF in vapor phase to etch away the buried oxide and create a suspended Si membrane with the Nb circuit patterned on top.

1. Deposit 15 nm ALD Alumina at 300°C
2. Double-Spin/Bake
   - Pre-bake at 180°C for 3min
   - Spin ZEP 520a at 3000 rpm for 1min
   - Bake at 180°C for 3min
   - Spin ZEP 520a at 3000 rpm for 1min
   - Post-Bake at 180°C for 3min
3. E-Beam Lithography
   - Beam current 1nA
   - Fracturing resolution 2nm
   - Dose 300 $\mu C/cm^2$
4. Development
   - ZED N50 for 2.5min
   - MIBK for 30s
   - N_2 blow dry
   - O_2 plasma ash at 150W, 12 sccm O_2 flow for 2min
5. ICP-RIE Etching of Release Holes

- 8.5 min Ar ion etch of the 15 nm thick alumina layer using parameters listed in Table 8.4. The etch rate is ~ 2nm/min, so we are over-etching by 1 min.
- 8.5min SF_6/C_4F_8 etch of the Nb and Si device layers using parameters listed in Table 8.5. We try to over-etch by ~50% in this step as the goal is to make sure we have etched all the way into the buried oxide layer.

6. <u>VHF release</u>

Chapter 9

APPENDIX: DEVELOPMENT OF AN ETCH PROCESS FOR LITHIUM NIOBATE ON SILICON-ON-INSULATOR

In Chapter 6, we discussed the design of our piezo-optomechanical transducer device based on a lithium niobate (LN) on silicon-on-insulator (SOI) platform. As explained in Chapter 6, this choice of materials was motivated by a desire to optimize both the piezo-electric interaction g_{pe} and the optomechanical interaction g_{om}. However, this material platform poses some unique nano-fabrication challenges related to the etching of thin film lithium niobate without damaging the underlying silicon device layer of the SOI substrate [1]

Lithium niobate is a very chemically stable material, so it is quite challenging to etch. In the past, a few different processes have been used to etch lithium niobate mainly for application in nanophotonics. These range from mechanical processes like dicing [193, 194] and chemical-mechanical polishing (CMP) [195–197] to wet etching [198–204] and dry etching [205–215]. We are interested in etching lithium niobate piezo-acoustic cavities with sub 1μm dimensions. In the literature, mechanical processes for micro-machining LN tend to be limited to feature sizes on the order of ~ few μm which is too large for our purposes. For wet etching lithium niobate, the most common etchant used is a mix of hydrofluoric acid (HF) and nitric acid (HNO_3) [198–201]. Unfortunately, this mixture is also a silicon etchant [216], so it is also not suitable for our purposes. Undercutting below the mask is another common issue with wet-etching and makes it difficult to achieve tight dimension control for sub μm size features.

9.1 Dry Etch Process

Given the desired small dimensions of our LN piezo-acoustic cavities, we would like to develop a dry reactive ion etch (RIE) process which exhibits good anisotropy and allows tight dimension control. Due to its chemical stability however, there are not many gas chemistries that can etch LN. Fluorine based chemistries have been employed in the past to etch LN. However, this produces non-volatile lithium-fluoride (LiF) as a by-product which causes severe redeposition issues inhibiting

[1]For all of the etches described in this chapter, we use thin film X-cut or -Z-cut LN bonded to a SOI substrate with a 220 nm thick Si device layer. The bonding is carried out by NanoLN.

further etching [206]. In recent years, a purely physical etch based on Ar^+ ions has been employed quite successfully to etch LN [213–215] exhibiting fairly steep sidewalls and high anisotropy. Inspired by these results, we begin by developing an Ar^+ ion ICP-RIE etch process to pattern LN piezo-acoustic cavities on SOI. We utilize an Oxford Instruments Plasmalab 100 ICP-RIE 380 system for our etch. The parameters that we choose to vary are the chamber pressure, ICP power, and RF power. While the overall dependence of the etch on these three parameters is complex, we observe two trends: **1.** The sidewall angle of the etched LN is steeper at lower process pressures. **2.** For fixed ICP power, the etch rate of LN can be increased by increasing the RF power. After some exploration of the parameter space, we arrive at the etch parameters given in Table 9.1. The mask we use for the dry etch is a thin film chrome (Cr) mask which is patterned using e-beam lithography, e-beam evaporation, and metal liftoff. We use ~400nm thick layer of ZEP 520a e-beam resist for lithography. The evaporation is carried out in a CHA Mark-40 e-beam evaporator at a rate of 0.2nm/s. We find a 1:1 selectivity of LN to Cr for our chosen etch parameters. An LN piezo 'box' etched using this process is shown in Fig. 9.1. We are able to achieve a ~40 degree sidewall angle using this process. As can be seen from Fig. 9.1, there is fair amount of sidewall roughness in our piezo 'box'. The origin of this roughness is not clear, but seems to be influenced by our choice of masking material. Replacing chrome with PECVD deposited SiO_2 seems to greatly improve the sidewall roughness and sidewall angle. Other groups have reported fairly smooth and steep sidewalls using a hydrogen silsesquioxane (HSQ) mask for a similar Ar^+ ion etch [213, 214].

Parameter	**Value**
ICP Power	600 W
RF Power	150 W
Ar Flow	20 sccm
Temperature	21 C
Process Pressure	1.5 mTorr
Helium Backing Pressure	4 torr
LN Etch Rate	20 nm/min
Cr Etch Rate	20 nm/min
Si Etch Rate	13 nm/min

Table 9.1: LN dry etch parameters

Using this dry etch process, we fabricate a wavelength scale lithium niobate piezo-acoustic cavity as shown in Fig. 9.2a. However, since this dry etch relies on a

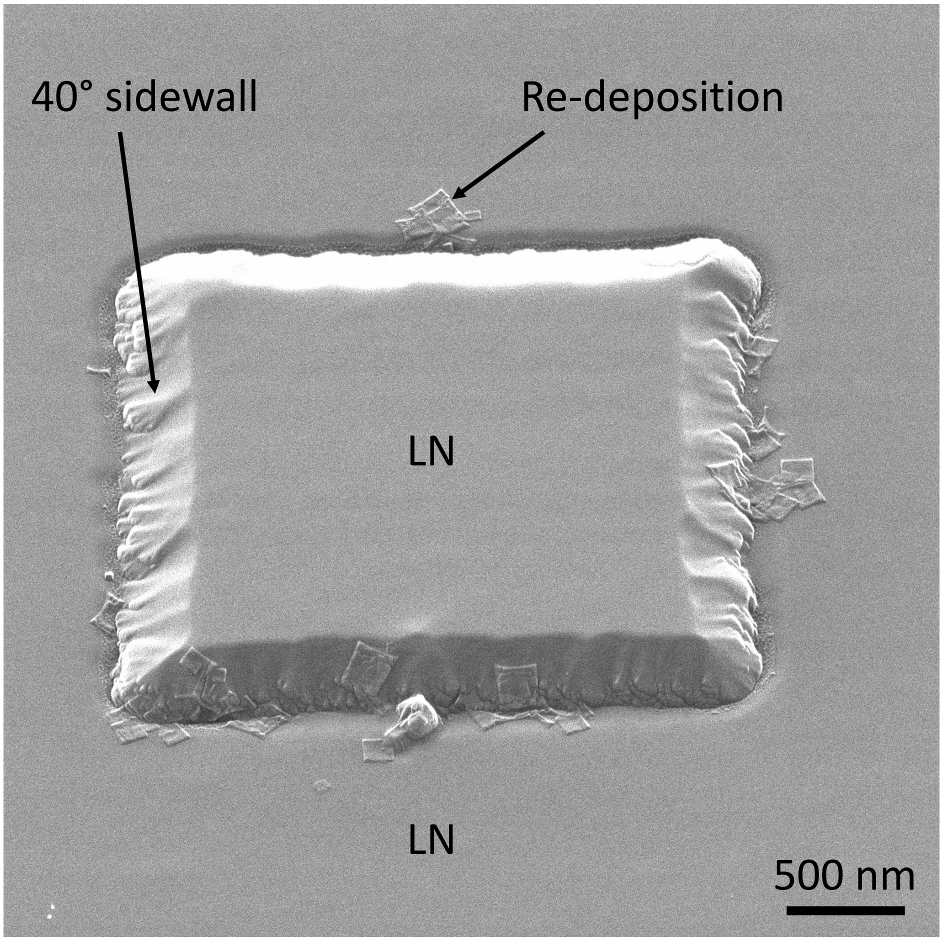

Figure 9.1: **LN piezo box etched using an Ar^{+} ion based ICP-RIE dry etch process.**

purely physical process where Ar^{+} ions bombard the surface of the LN to etch it, the etch is not selective between LN and silicon. As a result, the etch must be timed precisely to prevent over-etching into the underlying silicon device layer of our SOI substrate. Since our optimized etch uses fairly high power, it etches silicon at a high rate of ~13 nm/min and makes it difficult to prevent significant over-etching into the silicon. This over-etching damages the surface of the silicon and induces a high level of roughness in the silicon layer as seen in Fig. 9.2 b,c. We suspect that the cause of this roughness is micro-masking from redeposited LN during the etch process (Fig. 9.1). Further, the thin film LN as supplied by the vendor is not uniform in thickness. Even on a 1cmx1cm chip scale, there are thickness variations as high as ~40nm. As a result, etching away the LN layer where it is thickest will necessarily involve significant over-etching in parts where the LN layer is thinner creating unavoidable damage in the silicon layer. Recall from Chapter 6 that our optomechanical cavity is patterned in the silicon device layer. The quality factor of the optical mode is extremely sensitive to scattering from defects in the silicon and the large amount of roughness induced by our LN dry etch in the silicon will almost certainly degrade our optical quality factors significantly. Thus, while this Ar^+ ion dry etch has shown to be promising for etching nanophotonic devices in LN substrates, it is not compatible with our LN on SOI platform where our optomechanical device is patterned in silicon.

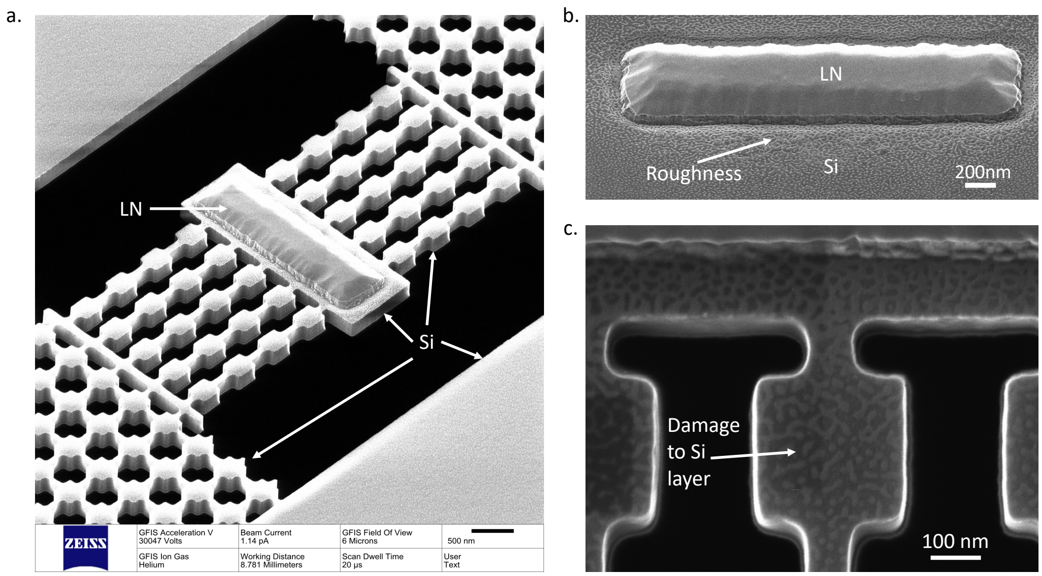

Figure 9.2: **Dry etched LN piezo-acoustic cavity showing Si damage. a.** LN piezo-acoustic cavity on SOI patterned via dry etching. **b.** and **c.** Zoom-ins showing damage to the Si device layer due to the physical nature of the dry etch.

9.2 Wet Etch Process

To prevent damage to the silicon (Si) device layer of our SOI substrate, it is important to develop an etch that is selective between LN and Si. To this end, we started investigating etchants that could etch LN without attacking Si. As mentioned earlier, the most commonly used wet etchant for LN is a mix of HF and HNO_3, but this etchant readily attacks Si. However [202, 203] showed that concentrated HF at elevated temperatures is able to etch -Z cut LN. HF does not etch Si and is commonly used to etch away native silicon oxide from the surface of Si wafers. However, there are significant safety concerns associated with heating HF to elevated temperatures. We decided to investigate if room temperature 48% concentrated HF could selectively etch -Z cut LN without attacking Si. The challenge with using concentrated HF as an etchant is to find a suitable etch mask since most materials are etched by HF. Gold (Au) is one of the few materials that is inert in HF. Since gold can be readily deposited using e-beam evaporation, we decided to use a gold mask for our HF etch. We again used e-beam lithography, e-beam evaporation, and metal liftoff to pattern our gold mask similar to the process used to pattern the chrome mask for dry etching. To improve the adhesion of gold to our LN thin film, we first evaporate a thin 'adhesion layer' (~5-10nm) of chrome (Cr) followed by 200nm of gold. Such a Cr/Au mask is commonly used in etching of glass using HF. One of the issues with a Cr/Au mask is the formation of defects or pinholes that allow the HF to penetrate through the masking layer. These defects are thought to originate upon cooling of the substrate post e-beam evaporation of the masking layer [217]. Since the surface of the gold tends to be hydrophilic, the HF can get sucked into these defects and penetrate through the mask to the underlying LN. To prevent this, we do our gold deposition in two steps. We first evaporate 100nm of gold and then pause the evaporation to let the substrate cool. After about 15-30 minutes of a 'cooldown period', we restart the evaporation and deposit the remaining 100nm of gold. In this manner, any defects generated in the first evaporation are covered up by the second evaporation making it harder for the HF to penetrate through the masking layer. In principle, breaking the evaporation into a larger number of steps would increase the robustness of the mask, but we find a two step evaporation to be sufficient.

Since our etchant (conc. HF) selectively etches the -Z crystal face of LN much faster than any other crystal face, it is possible to achieve a highly anisotropic etch. To test our Cr/Au mask and the anistropy of the etch, we try to etch simple LN 'boxes' as shown in Fig. 9.3a. It is clear from the figure that this etch is fairly anisotropic giving sidewall angles as high as ~50 degrees. Further, the sidewall roughness is much reduced compared to the dry etch. However, in Fig. 9.3a, we have not yet etched all the way through the LN to the Si device layer. We find that while the HF etches the -Z surface of LN quite well and does not attack Si, when the etch reaches the interface between the LN and the underlying Si, it causes 'delamination' of our LN boxes as shown in Fig. 9.3c. We suspect that there is some native oxide present at the interface between the LN and the Si which is rapidly attacked by the HF causing the LN box to 'peel off'.

9.3 Proposed Hybrid Etch Process

In the previous sections, we have seen the advantages and disadvantages of the dry and wet etch processes for etching LN. The dry etch has the advantage of being

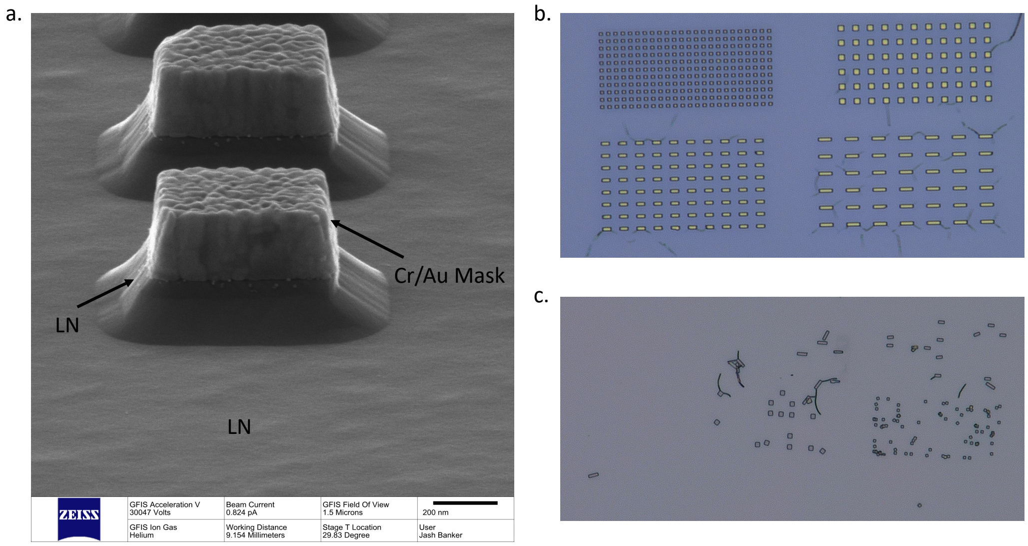

Figure 9.3: **Wet etched LN 'boxes'. a.** LN 'box' etched using 48% HF. Note that the etch has not progressed all the way to Si. There is a thin layer of LN left on the surface. **b.** Optical image of patterned LN boxes before etching to Si. **c.** Optical image of patterned LN boxes post etching to Si. Most of the boxes have 'peeled off' and can be seen displaced.

anisotropic and not attacking the interface between LN and Si. However it is not selective between LN and Si, and hence causes significant damage to the Si surface. The wet etch using 48% HF on the other hand can be anisotropic and selective between LN and Si however it rapidly attacks the LN-Si interface. Here we propose combining these two etches into a 'hybrid' etch process. This is a 3-step process. In the first step, we define a narrow 'trench' around where we want our LN box. This trench is etched most of the way using the wet etch described in Section 9.2, but we do not etch the trench all the way through to the Si layer. We propose leaving about 20 nm of LN in the trench. By etching the trench most of the way with a wet etch we are able to get smooth steep sidewalls as seen in Fig. 9.4. At the same time, stopping the wet etch before it reaches the Si prevents the HF from attacking the LN-Si interface. Next, we use the dry etch of Section 9.1 to etch through the last 20 nm of LN in the trench and overetch about 10-20 nm into the Si device layer. This will create some damage to the surface of the Si, but this damage region will be confined to the trench which can be made as narrow as $\sim$ 100 nm and is only limited by the accuracy of alignment during our e-beam lithography. The overetch into Si in the trench region exposes the LN-Si interface as shown in Fig. 9.4. Subsequently, we deposit a Cr/Au mask that not only covers the top of our LN 'box', but also fills the trench, and so protects the exposed LN-Si interface. Now we can use the wet etch to etch away the remaining LN everywhere else on the chip. Since the Cr/Au

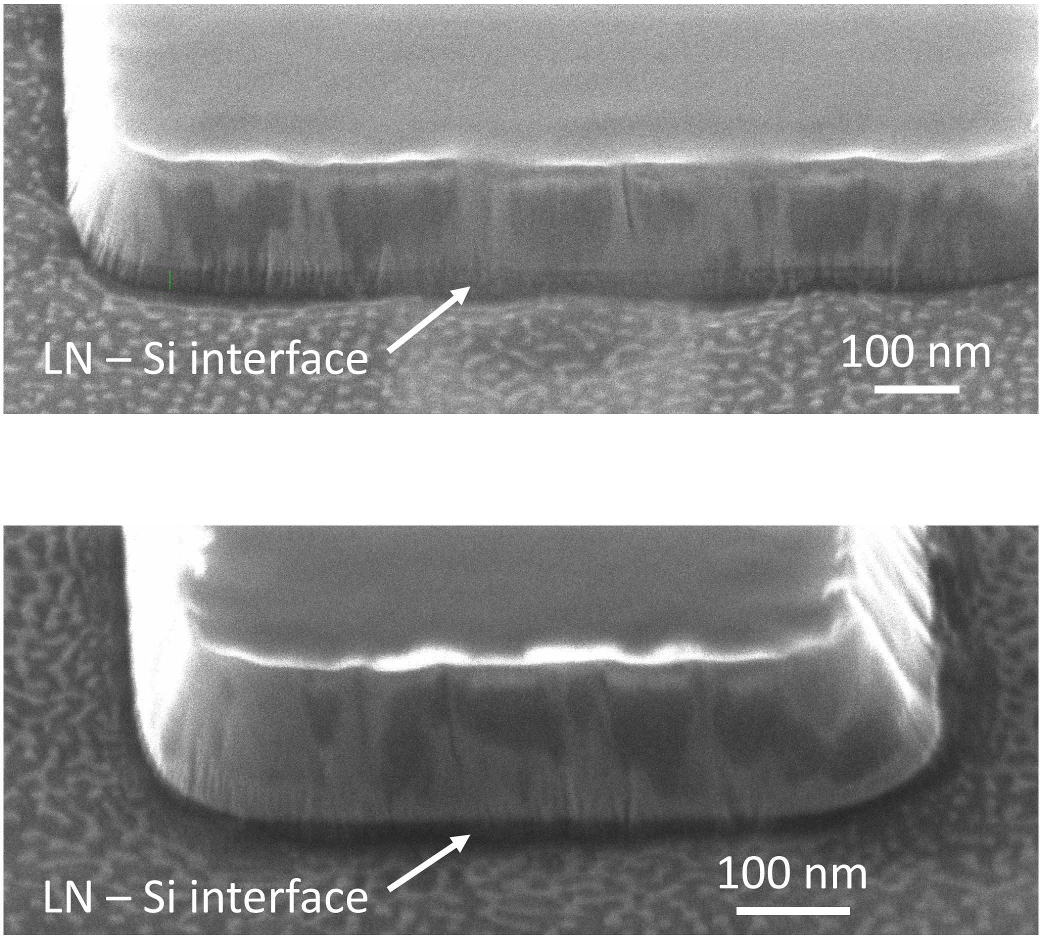

Figure 9.4: **LN piezo box etched using a combination of wet and dry etches.** Smooth sidewalls of a LN piezo 'box' etched using a wet etch most of the way followed by a dry etch to clear the last ~40 nm of LN and expose the LN-Si interface. Note that this particular sample did not have a trench defined, but by utilizing a trench the damage to the Si surface can be limited to the trench region.

mask is filling the trench, it covers the LN-Si interface near the LN 'box' and we expect that the box will not delaminate since the HF is unable to penetrate through the mask and attack the LN-Si interface. In this manner we can utilize a combination of the above developed etches to etch LN on SOI without creating a large damaged Si region. The damage is confined to the trench and thus will minimize the effect on the optical quality factors of the OMC patterned in the silicon. The schematic of our proposed 'hybrid' etch process is shown in Fig. 9.5 Suggested steps for our proposed hybrid etch process are detailed below. We assume that we are starting with 100 nm of -Z cut LN on SOI.

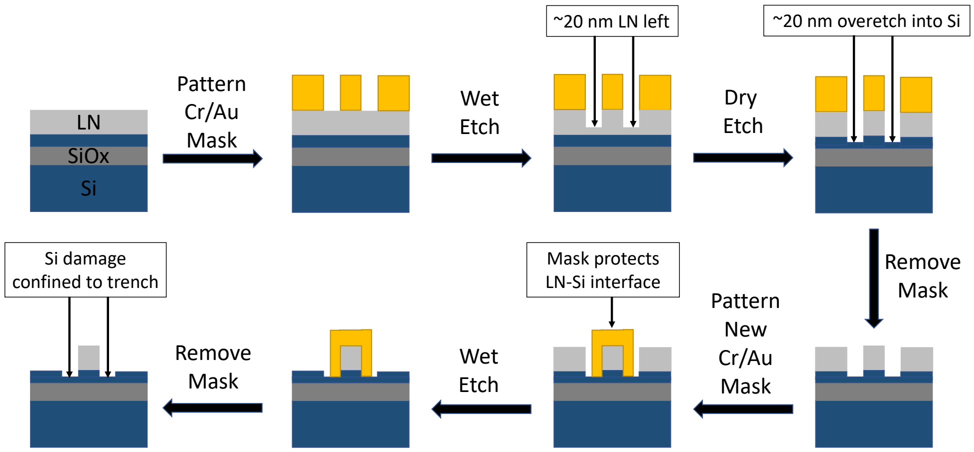

Figure 9.5: **Proposed Hybrid Etch Process for LN.**

Layer 1: Markers. Markers are used for alignment for subsequent e-beam lithography steps. In our group, we typically use 20μm × 20μm squares of ~150 nm thick e-beam evaporated niobium (Nb) as our markers.

1. Chip Cleaning

   - Acetone 5min sonication
   - IPA 5min sonication
   - N_2 blow dry
   - O_2 plasma ash at 150W, 12sccm O_2 flow for 2min
   - 15s dip in 10:1 Buffered HF (BHF) followed by 2x 10s DI H_20 rinse

2. Titanium Conductive Layer for E-beam Lithography

   Since LN is an insulating substrate, we need to deposit a conducting layer to prevent charging effects during electron-beam lithography. This can be achieved in a variety of ways. There are commercially available conductive polymers (such as AquaSave) which can be spun on top of e-beam resist and help disperse charge. An alternative is to lay down a thin layer of metal that will serve to conduct away charge. This metal layer can be above or below the resist. We decide to use a thin titanium (Ti) layer underneath the e-beam resist to reduce charging effects during e-beam lithography. This thin Ti layer can be easily removed by a short ~30s BHF dip.

   - Deposit ~5-10 nm of Ti using e-beam evaporation

3. Spin/Bake ZEP 520a
   - Pre-bake at 180°C for 3min
   - Spin ZEP 520a at 3000 rpm for 1 min
   - Post-bake at 180°C for 3min
4. E-Beam Lithography
   - Beam current 50nA
   - Fracturing resolution 20nm
   - Dose 230 $\mu C/cm^2$
5. Development
   - ZED N50 for 2.5min
   - MIBK for 30s
   - N_2 blow dry
   - O_2 plasma ash at 150W, 12sccm O_2 flow for 2min
6. E-beam Evaporation of Nb
   - 30s BHF dip to remove the Ti conducting layer where the markers will be deposited
   - Evaporate 150nm thick Nb at 0.4nm/s
7. Lift-off
   - NMP at 150°C for 2hr
   - Acetone 5min sonication
   - IPA 5min sonication
   - N_2 blow dry
   - O_2 plasma ash at 150W, 12sccm O_2 flow for 2min
   - 30s dip in 10:1 Buffered HF followed by 2x 10s DI H_20 rinse - this removes the remaining Ti conductive layer.

Layer 2: Trench This layer is to define the trench around where we want our LN ‘boxes’

1. Fresh Titanium Conductive Layer for E-beam Lithography
   - Deposit ~5-10 nm of Ti using e-beam evaporation
2. Spin/Bake ZEP 520a
   - Pre-bake at 180°C for 3min
   - Spin ZEP 520a at 3000 rpm for 1min
   - Post-bake at 180°C for 3min
3. E-Beam Lithography
   - Beam current 4nA (small features) and 50nA (large features)
   - Fracturing resolution 4nm (small features) and 20nm (large features)
   - Dose 230 $\mu C/cm^2$
4. Development
   - ZED N50 for 2.5min
   - MIBK for 30s
   - N2 blow dry
   - O_2 plasma ash at 150W, 12sccm O_2 flow for 2min
5. E-beam Evaporation of Cr/Au mask
   - 30s BHF dip to remove the Ti conducting layer where the mask will be deposited
   - Evaporate ~ 5-10 nm thick Cr
   - Evaporate 100 nm thick Au
   - 15-30 min cooldown period
   - Evaporate 100 nm thick Au
6. Lift-off
   - NMP at 150°C for 2hr
   - Acetone 5min sonication
   - IPA 5min sonication
   - N_2 blow dry

- O_2 plasma ash at 150W, 12sccm O_2 flow for 2min

7. Trench Wet Etch

   - 2min dip in 48% HF. Etch rate of -Z cut LN in 48% HF is ~ 40 nm/min so we are aiming to etch about 80 nm of LN. Followed by 2x 10s DI H_2O rinse and N_2 blow dry.

8. Trench Dry Etch

   - 2min dry etch using the parameters listed in Table 9.1. Etch rate of LN is 20 nm/min so a 2min etch would etch away the remaining 20 nm of LN and overetch about 15 nm into the Si device layer. We suggest using the same Cr/Au mask used in the wet etch for this short dry etch but we have not tested the selectivity of this mask for the dry etch process. Since it is a short 2min etch we assume the mask will survive the etch. If it does not a thicker mask might be required.

9. Strip Cr/Au mask

   - 3min in Gold Etch TFA (from Transene) at 30°C with 400 rpm stirring followed by 2x DI H_2O rinse and N_2 blow dry
   - 1min in Chrome Etch 1020AC (from Transene) at 40°C with 400 rpm stirring followed by 2x DI H_2O rinse and N_2 blow dry

Layer 3: Final Wet Etch. In this layer, we lay down a fresh Cr/Au mask that fills the trench defined in Layer 2 and protects the LN-Si interface. We then use a wet etch to remove the LN everywhere else on the chip.

1. Fresh Titanium Conductive Layer for E-beam Lithography

   - Deposit ~5-10 nm of Ti using e-beam evaporation

2. Spin/Bake ZEP 520a

   - Pre-bake at 180°C for 3min
   - Spin ZEP 520a at 3000 rpm for 1 min
   - Post-bake at 180°C for 3min

3. E-Beam Lithography

   In this step, we need to ensure that the write area covers not just the top of the LN ‘box’, but extends into the trench too. We suggest a pattern that extends about halfway into the trench area. Since we want this write to line up precisely with our previously defined trench, the alignment accuracy of the e-beam tool is essential. Typical misalignment on our e-beam lithography tool is ~ ± 50 nm. If we use a trench width > 100 nm, that should be sufficient to guard against ~ 50 nm level misalignment.

   - Beam current 4nA
   - Fracturing resolution 4nm
   - Dose 230 $\mu C/cm^2$

4. Development

   - ZED N50 for 2.5min
   - MIBK for 30s
   - N_2 blow dry
   - O_2 plasma ash at 150W, 12sccm O_2 flow for 2min

5. E-beam Evaporation of Cr/Au mask

   - 30s BHF dip to remove the Ti conducting layer where the mask will be deposited
   - Evaporate ~ 5-10 nm thick Cr
   - Evaporate 100 nm thick Au
   - 15-30 min cooldown period
   - Evaporate 100 nm thick Au

6. Lift-off

   - NMP at 150°C for 2hr
   - Acetone 5min sonication
   - IPA 5min sonication
   - N_2 blow dry
   - O_2 plasma ash at 150W, 12sccm O_2 flow for 2min

7. Final Wet Etch

    - 3min dip in 48% HF followed by 2x 10s DI H_2O rinse and N_2 blow dry. This should be enough to etch through the 100 nm thick LN film.

8. Strip Cr/Au mask

    - 3min in Gold Etch TFA (from Transene) at 30°C with 400 rpm stirring followed by 2x DI H_2O rinse and N_2 blow dry
    - 1 min in Chrome Etch 1020AC (from Transene) at 40°C with 400 rpm stirring followed by 2x DI H_2O rinse and N_2 blow dry.

BIBLIOGRAPHY

[1] J. D. Joannopoulos, S. G. Johnson, J. N. Winn, and R. D. Meade. *Photonic Crystals: Molding the Flow of Light (Second Edition)*. 2nd ed. Princeton University Press. ISBN: 0691124566.

[2] V. Weisskopf and E. Wigner. "Berechnung der naturlichen linienbreite auf grund der diracschen lichttheorie". In: *Zeitschrift für Physik* 63.1-2 (1930), pp. 54–73.

[3] J. F. Haase, P. J. Vetter, T. Unden, A. Smirne, J. Rosskopf, B. Naydenov, A. Stacey, F. Jelezko, M. B. Plenio, and S. F. Huelga. "Controllable non-Markovianity for a spin qubit in diamond". In: *Phys. Rev. Lett.* 121.6 (2018), p. 060401.

[4] U. Hoeppe, C. Wolff, J. Küchenmeister, J. Niegemann, M. Drescher, H. Benner, and K. Busch. "Direct observation of non-Markovian radiation dynamics in 3D bulk photonic crystals". In: *Phys. Rev. Lett.* 108.4 (2012), p. 043603.

[5] B.-H. Liu, L. Li, Y.-F. Huang, C.-F. Li, G.-C. Guo, E.-M. Laine, H.-P. Breuer, and J. Piilo. "Experimental control of the transition from Markovian to non-Markovian dynamics of open quantum systems". In: *Nat. Phys.* 7.12 (2011), p. 931.

[6] K. H. Madsen, S. Ates, T. Lund-Hansen, A. Löffler, S. Reitzenstein, A. Forchel, and P. Lodahl. "Observation of non-Markovian dynamics of a single quantum dot in a micropillar cavity". In: *Phys. Rev. Lett.* 106.23 (2011), p. 233601.

[7] H. Pichler, S. Choi, P. Zoller, and M. D. Lukin. "Universal photonic quantum computation via time-delayed feedback". In: *PNAS* 114.43 (2017), pp. 11362–11367.

[8] F. Arute, K. Arya, R. Babbush, D. Bacon, J. C. Bardin, R. Barends, R. Biswas, S. Boixo, F. G. S. L. Brandao, D. A. Buell, et al. "Quantum supremacy using a programmable superconducting processor". In: *Nature* 574.7779 (2019), pp. 505–510.

[9] N. J. Lambert, A. Rueda, F. Sedlmeir, and H. G. Schwefel. "Coherent conversion between microwave and optical photons—an overview of physical implementations". In: *Adv. Quantum Technol.* 3.1 (2020), p. 1900077.

[10] M. Mirhosseini, A. Sipahigil, M. Kalaee, and O. Painter. "Superconducting qubit to optical photon transduction". In: *Nature* 588.7839 (2020), pp. 599–603.

[11] A. Leo, G. Grimaldi, R. Citro, A. Nigro, S. Pace, and R. Huebener. "Quasiparticle scattering time in niobium superconducting films". In: *Phys. Rev. B* 84.1 (2011), p. 014536.

[12] M. Johnson. "Direct real time measurement of quasiparticle lifetimes in a superconductor". In: *Phys. Rev. Lett.* 67.3 (1991), p. 374.

[13] S. M. Girvin. "Circuit QED: superconducting qubits coupled to microwave photons". In: *Quantum Machines: Measurement and Control of Engineered Quantum Systems*. Ed. by M. Devoret, B. Huard, R. Schoelkopf, and L. F. Cugliandolo. Oxford, UK: Oxford University Press, 2011. Chap. 3, pp. 113–256.

[14] G. Wendin. "Quantum information processing with superconducting circuits: a review". In: *Rep. Prog. Phys.* 80.10 (2017), p. 106001.

[15] P. Krantz, M. Kjaergaard, F. Yan, T. P. Orlando, S. Gustavsson, and W. D. Oliver. "A quantum engineer's guide to superconducting qubits". In: *Appl. Phys. Rev.* 6.2 (2019), p. 021318.

[16] J. Koch, T. M. Yu, J. Gambetta, A. A. Houck, D. I. Schuster, J. Majer, A. Blais, M. H. Devoret, S. M. Girvin, and R. J. Schoelkopf. "Charge-insensitive qubit design derived from the Cooper pair box". In: *Phys. Rev. A* 76 (Oct. 2007), p. 042319.

[17] V. P. Bykov. "Spontaneous emission from a medium with a band spectrum". In: *Sov. J. Quantum Electron.* 4.7 (1975), p. 861.

[18] S. John and J. Wang. "Quantum electrodynamics near a photonic band gap: Photon bound states and dressed atoms". In: *Phys. Rev. Lett.* 64.20 (1990), p. 2418.

[19] S. John and J. Wang. "Quantum optics of localized light in a photonic band gap". In: *Phys. Rev. B* 43.16 (1991), p. 12772.

[20] E. Yablonovitch. "Inhibited spontaneous emission in solid-state physics and electronics". In: *Phys. Rev. Lett.* 58.20 (1987), p. 2059.

[21] S. John. "Strong localization of photons in certain disordered dielectric superlattices". In: *Phys. Rev. Lett.* 58.23 (1987), p. 2486.

[22] S. John and T. Quang. "Spontaneous emission near the edge of a photonic band gap". In: *Phys. Rev. A* 50.2 (1994), p. 1764.

[23] H. Shen, S. Xu, H. Cui, and X. Yi. "Non-Markovian dynamics of a system of two-level atoms coupled to a structured environment". In: *Phys. Rev. A* 99.3 (2019), p. 032101.

[24] A. González-Tudela and J. I. Cirac. "Markovian and non-Markovian dynamics of quantum emitters coupled to two-dimensional structured reservoirs". In: *Phys. Rev. A* 96.4 (2017), p. 043811.

[25] P. Lambropoulos, G. M. Nikolopoulos, T. R. Nielsen, and S. Bay. "Fundamental quantum optics in structured reservoirs". In: *Rep. Prog. Phys.* 63.4 (2000), p. 455.

[26] N. Vats and S. John. "Non-Markovian quantum fluctuations and superradiance near a photonic band edge". In: *Phys. Rev. A* 58.5 (1998), p. 4168.

[27] B. Bellomo, R. L. Franco, and G. Compagno. "Non-Markovian effects on the dynamics of entanglement". In: *Phys. Rev. Lett.* 99.16 (2007), p. 160502.

[28] B. Bellomo, R. L. Franco, S. Maniscalco, and G. Compagno. "Entanglement trapping in structured environments". In: *Phys. Rev. A* 78.6 (2008), p. 060302.

[29] C. Gonzalez-Ballestero, F. J. García-Vidal, and E. Moreno. "Non-Markovian effects in waveguide-mediated entanglement". In: *New J. Phys.* 15.7 (2013), p. 073015.

[30] S. F. Huelga, A. Rivas, and M. B. Plenio. "Non-Markovianity-assisted steady state entanglement". In: *Phys. Rev. Lett.* 108.16 (2012), p. 160402.

[31] J. Cheng, W.-Z. Zhang, L. Zhou, and W. Zhang. "Preservation macroscopic entanglement of optomechanical systems in non-Markovian environment". In: *Sci. Rep.* 6 (2016), p. 23678.

[32] D. M. Reich, N. Katz, and C. P. Koch. "Exploiting non-Markovianity for quantum control". In: *Sci. Rep.* 5 (2015), p. 12430.

[33] B. Bylicka, D. Chruściński, and S. Maniscalco. "Non-Markovianity and reservoir memory of quantum channels: a quantum information theory perspective". In: *Sci. Rep.* 4 (2014), p. 5720.

[34] D. T. H. Tan, K. Ikeda, R. Saperstein, B. Slutsky, and Y. Fainman. "Chip-scale dispersion engineering using chirped vertical gratings". In: *Opt. Lett.* 33.24 (2008), pp. 3013–3015.

[35] C. Caloz. "Metamaterial dispersion engineering concepts and applications". In: *Proc. IEEE* 99.10 (2011), pp. 1711–1719.

[36] A. Säynätjoki, M. Mulot, J. Ahopelto, and H. Lipsanen. "Dispersion engineering of photonic crystal waveguides with ring-shaped holes". In: *Opt. Express* 15.13 (2007), pp. 8323–8328.

[37] T. Tufarelli, M. S. Kim, and F. Ciccarello. "Non-Markovianity of a quantum emitter in front of a mirror". In: *Phys. Rev. A* 90.1 (2014), p. 012113.

[38] H. Pichler and P. Zoller. "Photonic circuits with time delays and quantum feedback". In: *Phys. Rev. Lett.* 116.9 (2016), p. 093601.

[39] I.-C. Hoi, A. Kockum, L. Tornberg, A. Pourkabirian, G. Johansson, P. Delsing, and C. Wilson. "Probing the quantum vacuum with an artificial atom in front of a mirror". In: *Nat. Phys.* 11.12 (2015), p. 1045.

[40] Y.-L. L. Fang, F. Ciccarello, and H. U. Baranger. "Non-Markovian dynamics of a qubit due to single-photon scattering in a waveguide". In: *New J. Phys.* 20.4 (2018), p. 043035.

[41] T. Tufarelli, F. Ciccarello, and M. Kim. "Dynamics of spontaneous emission in a single-end photonic waveguide". In: *Phys. Rev. A* 87.1 (2013), p. 013820.

[42] D. O. Krimer, M. Liertzer, S. Rotter, and H. E. Türeci. "Route from spontaneous decay to complex multimode dynamics in cavity QED". In: *Phys. Rev. A* 89.3 (2014), p. 033820.

[43] A. Carmele, J. Kabuss, F. Schulze, S. Reitzenstein, and A. Knorr. "Single photon delayed feedback: A way to stabilize intrinsic quantum cavity electrodynamics". In: *Phys. Rev. Lett.* 110.1 (2013), p. 013601.

[44] L. Guo, A. F. Kockum, F. Marquardt, and G. Johansson. "Oscillating bound states for a giant atom". In: *Phys. Rev. Research* 2.4 (2020), p. 043014.

[45] F. Dinc. "Diagrammatic approach for analytical non-Markovian time evolution: Fermi's two-atom problem and causality in waveguide quantum electrodynamics". In: *Phys. Rev. A* 102 (1 July 2020), p. 013727.

[46] G. Calajó, Y.-L. L. Fang, H. U. Baranger, F. Ciccarello, et al. "Exciting a bound state in the continuum through multiphoton scattering plus delayed quantum feedback". In: *Phys. Rev. Lett.* 122.7 (2019), p. 073601.

[47] S. Garmon, K. Noba, G. Ordonez, and D. Segal. "Non-markovian dynamics revealed at a bound state in the continuum". In: *Phys. Rev. A* 99.1 (2019), p. 010102.

[48] F. Dinc and A. M. Brańczyk. "Non-Markovian super-superradiance in a linear chain of up to 100 qubits". In: *Phys. Rev. Research* 1.3 (2019), p. 032042.

[49] K. Sinha, P. Meystre, E. A. Goldschmidt, F. K. Fatemi, S. L. Rolston, and P. Solano. "Non-Markovian collective emission from macroscopically separated emitters". In: *Phys. Rev. Lett.* 124.4 (2020), p. 043603.

[50] H. Zheng and H. U. Baranger. "Persistent quantum beats and long-distance entanglement from waveguide-mediated interactions". In: *Phys. Rev. Lett.* 110.11 (2013), p. 113601.

[51] A. Carmele, N. Nemet, V. Canela, and S. Parkins. "Pronounced non-Markovian features in multiply excited, multiple emitter waveguide QED: Retardation induced anomalous population trapping". In: *Phys. Rev. Research* 2.1 (2020), p. 013238.

[52] T. Ramos, B. Vermersch, P. Hauke, H. Pichler, and P. Zoller. "Non-Markovian dynamics in chiral quantum networks with spins and photons". In: *Phys. Rev. A* 93.6 (2016), p. 062104.

[53] R. J. Schoelkopf and S. M. Girvin. "Wiring up quantum systems". In: *Nature* 451 (Feb. 2008), pp. 664–669.

[54] M. H. Devoret and R. J. Schoelkopf. “Superconducting circuits for quantum information: An outlook”. In: *Science* 339 (6214 Mar. 2013), pp. 1169–1174.

[55] A. F. Van Loo, A. Fedorov, K. Lalumière, B. C. Sanders, A. Blais, and A. Wallraff. “Photon-mediated interactions between distant artificial atoms”. In: *Science* 342.6165 (2013), pp. 1494–1496.

[56] K. Lalumiere, B. C. Sanders, A. F. van Loo, A. Fedorov, A. Wallraff, and A. Blais. “Input-output theory for waveguide QED with an ensemble of inhomogeneous atoms”. In: *Phys. Rev. A* 88.4 (2013), p. 043806.

[57] E. Vetsch, D. Reitz, G. Sagué, R. Schmidt, S. Dawkins, and A. Rauschenbeutel. “Optical interface created by laser-cooled atoms trapped in the evanescent field surrounding an optical nanofiber”. In: *Phys. Rev. Lett.* 104.20 (2010), p. 203603.

[58] S.-P. Yu, J. Hood, J. Muniz, M. Martin, R. Norte, C.-L. Hung, S. M. Meenehan, J. D. Cohen, O. Painter, and H. Kimble. “Nanowire photonic crystal waveguides for single-atom trapping and strong light-matter interactions”. In: *Appl. Phys. Lett.* 104.11 (2014), p. 111103.

[59] A. Javadi, I. Söllner, M. Arcari, S. L. Hansen, L. Midolo, S. Mahmoodian, G. Kiršanskė, T. Pregnolato, E. Lee, J. Song, et al. “Single-photon non-linear optics with a quantum dot in a waveguide”. In: *Nat. Commun.* 6 (2015), p. 8655.

[60] M. K. Bhaskar, D. D. Sukachev, A. Sipahigil, R. E. Evans, M. J. Burek, C. T. Nguyen, L. J. Rogers, P. Siyushev, M. H. Metsch, H. Park, et al. “Quantum nonlinear optics with a germanium-vacancy color center in a nanoscale diamond waveguide”. In: *Phys. Rev. Lett.* 118.22 (2017), p. 223603.

[61] N. M. Sundaresan, R. Lundgren, G. Zhu, A. V. Gorshkov, and A. A. Houck. “Interacting qubit-photon bound states with superconducting circuits”. In: *Phys. Rev. X* 9.1 (2019), p. 011021.

[62] Y. Liu and A. A. Houck. “Quantum electrodynamics near a photonic bandgap”. In: *Nat. Phys.* 13.1 (2017), p. 48.

[63] G. Andersson, B. Suri, L. Guo, T. Aref, and P. Delsing. “Non-exponential decay of a giant artificial atom”. In: *Nat. Phys.* 15 (2019), pp. 1123–1127.

[64] M. Mirhosseini, E. Kim, V. S. Ferreira, M. Kalaee, A. Sipahigil, A. J. Keller, and O. Painter. “Superconducting metamaterials for waveguide quantum electrodynamics”. In: *Nat. Commun.* 9 (2018).

[65] M. Mirhosseini, E. Kim, X. Zhang, A. Sipahigil, P. B. Dieterle, A. J. Keller, A. Asenjo-Garcia, D. E. Chang, and O. Painter. “Cavity quantum electrodynamics with atom-like mirrors”. In: *Nature* 569.7758 (2019), p. 692.

[66] Y. Zhong, H.-S. Chang, K. Satzinger, M.-H. Chou, A. Bienfait, C. Conner, É. Dumur, J. Grebel, G. Peairs, R. Povey, et al. “Violating Bell’s inequality with remotely connected superconducting qubits”. In: *Nat. Phys.* (2019), p. 1.

[67] A. Bienfait, K. J. Satzinger, Y. Zhong, H.-S. Chang, M.-H. Chou, C. Conner, É. Dumur, J. Grebel, G. Peairs, R. Povey, et al. “Phonon-mediated quantum state transfer and remote qubit entanglement”. In: *Science* 364.6438 (2019), pp. 368–371.

[68] I.-C. Hoi, T. Palomaki, J. Lindkvist, G. Johansson, P. Delsing, and C. Wilson. “Generation of nonclassical microwave states using an artificial atom in 1D open space”. In: *Phys. Rev. Lett.* 108.26 (2012), p. 263601.

[69] C. Eichler, C. Lang, J. Fink, J. Govenius, S. Filipp, and A. Wallraff. “Observation of entanglement between itinerant microwave photons and a superconducting qubit”. In: *Phys. Rev. Lett.* 109.24 (2012), p. 240501.

[70] R. Barends, J. Kelly, A. Megrant, D. Sank, E. Jeffrey, Y. Chen, Y. Yin, B. Chiaro, J. Mutus, C. Neill, P. O’Malley, P. Roushan, J. Wenner, T. C. White, A. N. Cleland, and J. M. Martinis. “Coherent Josephson qubit suitable for scalable quantum integrated circuits”. In: *Phys. Rev. Lett.* 111 (Aug. 2013), p. 080502.

[71] C. Schön, E. Solano, F. Verstraete, J. I. Cirac, and M. M. Wolf. “Sequential generation of entangled multiqubit states”. In: *Phys. Rev. Lett.* 95.11 (2005), p. 110503.

[72] A. Russo, E. Barnes, and S. E. Economou. “Generation of arbitrary all-photonic graph states from quantum emitters”. In: *New J. Phys.* 21.5 (2019), p. 055002.

[73] S. Xu and S. Fan. “Generate tensor network state by sequential single-photon scattering in waveguide QED systems”. In: *APL Photonics* 3.11 (2018), p. 116102.

[74] A. Yariv, Y. Xu, R. K. Lee, and A. Scherer. “Coupled-resonator optical waveguide: A proposal and analysis”. In: *Opt. Lett.* 24.11 (1999), pp. 711–713.

[75] M. Notomi, E. Kuramochi, and T. Tanabe. “Large-scale arrays of ultrahigh-Q coupled nanocavities”. In: *Nat. Phot.* 2 (Nov. 2008), pp. 741–747.

[76] D. S. Wiersma, P. Bartolini, A. Lagendijk, and R. Righini. “Localization of light in a disordered medium”. In: *Nature* 390.6661 (1997), p. 671.

[77] D. M. Pozar. *Microwave engineering*. John Wiley & Sons, 2009.

[78] A. J. Keller, P. B. Dieterle, M. Fang, B. Berger, J. M. Fink, and O. Painter. “Al transmon qubits on silicon-on-insulator for quantum device integration”. In: *Appl. Phys. Lett.* 111.4 (2017), p. 042603.

[79] S. Shevchenko, S. Ashhab, and F. Nori. "Landau–Zener–Stückelberg interferometry". In: *Phys. Rep.* 492.1 (2010), pp. 1–30.

[80] E.-M. Laine, J. Piilo, and H.-P. Breuer. "Measure for the non-Markovianity of quantum processes". In: *Phys. Rev. A* 81.6 (2010), p. 062115.

[81] H.-P. Breuer. "Foundations and measures of quantum non-Markovianity". In: *J. Phys. B* 45.15 (2012), p. 154001.

[82] G. S. Agarwal. "Vacuum-field Rabi oscillations of atoms in a cavity". In: *J. Opt. Soc. Am. B* 2.3 (1985), pp. 480–485.

[83] Y. Wang, J. Minář, L. Sheridan, and V. Scarani. "Efficient excitation of a two-level atom by a single photon in a propagating mode". In: *Phys. Rev. A* 83.6 (2011), p. 063842.

[84] M. Stobińska, G. Alber, and G. Leuchs. "Perfect excitation of a matter qubit by a single photon in free space". In: *EPL* 86.1 (2009), p. 14007.

[85] J. Li, M. P. Silveri, K. S. Kumar, J.-M. Pirkkalainen, A. Vepsäläinen, W. C. Chien, J. Tuorila, M. A. Sillanpää, P. J. Hakonen, E. V. Thuneberg, et al. "Motional averaging in a superconducting qubit". In: *Nat. Commun.* 4 (2013), p. 1420.

[86] S. Barrett, K. Hammerer, S. Harrison, T. E. Northup, and T. J. Osborne. "Simulating quantum fields with cavity QED". In: *Phys. Rev. Lett.* 110.9 (2013), p. 090501.

[87] C. Eichler, J. Mlynek, J. Butscher, P. Kurpiers, K. Hammerer, T. J. Osborne, and A. Wallraff. "Exploring interacting quantum many-body systems by experimentally creating continuous matrix product states in superconducting circuits". In: *Phys. Rev. X* 5.4 (2015), p. 041044.

[88] C. Eichler, D. Bozyigit, C. Lang, L. Steffen, J. Fink, and A. Wallraff. "Experimental state tomography of itinerant single microwave photons". In: *Phys. Rev. Lett.* 106.22 (2011), p. 220503.

[89] S. Kono, K. Koshino, Y. Tabuchi, A. Noguchi, and Y. Nakamura. "Quantum non-demolition detection of an itinerant microwave photon". In: *Nat. Phys.* 14.6 (2018), pp. 546–549.

[90] J.-C. Besse, S. Gasparinetti, M. C. Collodo, T. Walter, P. Kurpiers, M. Pechal, C. Eichler, and A. Wallraff. "Single-shot quantum nondemolition detection of individual itinerant microwave photons". In: *Phys. Rev. X* 8.2 (2018), p. 021003.

[91] A. L. Grimsmo, B. Royer, J. M. Kreikebaum, Y. Ye, K. O'Brien, I. Siddiqi, and A. Blais. "Quantum metamaterial for nondestructive microwave photon counting". In: *arXiv preprint arXiv:2005.06483* (2020).

[92] A. Shearrow, G. Koolstra, S. J. Whiteley, N. Earnest, P. S. Barry, F. J. Heremans, D. D. Awschalom, E. Shirokoff, and D. I. Schuster. “Atomic layer deposition of titanium nitride for quantum circuits”. In: *Appl. Phys. Lett.* 113.21 (2018), p. 212601.

[93] R. Raussendorf, J. Harrington, and K. Goyal. “Topological fault-tolerance in cluster state quantum computation”. In: *New J. Phys.* 9.6 (2007), p. 199.

[94] I. Schwartz, D. Cogan, E. R. Schmidgall, Y. Don, L. Gantz, O. Kenneth, N. H. Lindner, and D. Gershoni. “Deterministic generation of a cluster state of entangled photons”. In: *Science* 354.6311 (2016), pp. 434–437.

[95] J.-C. Besse, K. Reuer, M. C. Collodo, A. Wulff, L. Wernli, A. Copetudo, D. Malz, P. Magnard, A. Akin, M. Gabureac, G. J. Norris, J. I. Cirac, A. Wallraff, and C. Eichler. “Realizing a deterministic source of multipartite-entangled photonic qubits”. In: *Nat. Commun.* 11.4877 (2020).

[96] J.-T. Shen and S. Fan. “Coherent single photon transport in a one-dimensional waveguide coupled with superconducting quantum bits”. In: *Phys. Rev. Lett.* 95.21 (2005), p. 213001.

[97] A. N. Korotkov. “Flying microwave qubits with nearly perfect transfer efficiency”. In: *Phys. Rev. B* 84.1 (2011), p. 014510.

[98] Y. Yin, Y. Chen, D. Sank, P. O’malley, T. White, R. Barends, J. Kelly, E. Lucero, M. Mariantoni, A. Megrant, et al. “Catch and release of microwave photon states”. In: *Phys. Rev. Lett.* 110.10 (2013), p. 107001.

[99] P. Forn-Diaz, C. W. Warren, C. W. S. Chang, A. M. Vadiraj, and C. M. Wilson. “On-demand microwave generator of shaped single photons”. In: *Phys. Rev. Appl.* 8.5 (2017), p. 054015.

[100] R. I. Killey, P. M. Watts, M. Glick, and P. Bayvel. “Electronic dispersion compensation by signal predistortion”. In: *2006 Optical Fiber Communication Conference and the National Fiber Optic Engineers Conference*. IEEE. 2006, 3–pp.

[101] S. Hughes. “Enhanced single-photon emission from quantum dots in photonic crystal waveguides and nanocavities”. In: *Opt. Lett.* 29.22 (2004), pp. 2659–2661.

[102] P. Lodahl, S. Mahmoodian, and S. Stobbe. “Interfacing single photons and single quantum dots with photonic nanostructures”. In: *Rev. Mod. Phys.* 87.2 (2015), p. 347.

[103] A. Kitaev. “Protected qubit based on a superconducting current mirror”. In: *arXiv preprint cond-mat/0609441* (2006).

[104] P. W. Shor. “Scheme for reducing decoherence in quantum computer memory”. In: *Phys. Rev. A* 52.4 (1995), R2493.

[105] A. P. M. Place, L. V. H. Rodgers, P. Mundada, B. M. Smitham, M. Fitzpatrick, Z. Leng, A. Premkumar, J. Bryon, S. Sussman, G. Cheng, et al. "New material platform for superconducting transmon qubits with coherence times exceeding 0.3 milliseconds". In: *arXiv preprint arXiv:2003.00024* (2020).

[106] S. Krinner, S. Storz, P. Kurpiers, P. Magnard, J. Heinsoo, R. Keller, J. Luetolf, C. Eichler, and A. Wallraff. "Engineering cryogenic setups for 100-qubit scale superconducting circuit systems". In: *EPJ Quantum Technol.* 6.1 (2019), p. 2.

[107] J.-H. Yeh, J. LeFebvre, S. Premaratne, F. Wellstood, and B. Palmer. "Microwave attenuators for use with quantum devices below 100 mK". In: *J. Appl. Phys.* 121.22 (2017), p. 224501.

[108] C. Macklin, K. O'Brien, D. Hover, M. E. Schwartz, V. Bolkhovsky, X. Zhang, W. D. Oliver, and I. Siddiqi. "A near–quantum-limited Josephson traveling-wave parametric amplifier". In: *Science* 350.6258 (Oct. 2015), pp. 307–310.

[109] H. Gersen, T. J. Karle, R. J. P. Engelen, W. Bogaerts, J. P. Korterik, N. F. Van Hulst, T. F. Krauss, and L. Kuipers. "Direct observation of Bloch harmonics and negative phase velocity in photonic crystal waveguides". In: *Phys. Rev. Lett.* 94.12 (2005), p. 123901.

[110] Y. Wang, Y. Zhang, L. He, F. Liu, H. Li, and H. Chen. "Direct observation of negative phase velocity and positive group velocity in time domain for composite right/left-handed transmission lines". In: *J. Appl. Phys.* 100.11 (2006), p. 113503.

[111] J. Woodley and M. Mojahedi. "Backward wave propagation in left-handed media with isotropic and anisotropic permittivity tensors". In: *J Opt Soc Am B* 23.11 (2006), pp. 2377–2382.

[112] G. Calajó, F. Ciccarello, D. Chang, and P. Rabl. "Atom-field dressed states in slow-light waveguide QED". In: *Phys. Rev. A* 93.3 (2016), p. 033833.

[113] F. Lombardo, F. Ciccarello, and G. M. Palma. "Photon localization versus population trapping in a coupled-cavity array". In: *Phys. Rev. A* 89.5 (2014), p. 053826.

[114] Y. Wang, H. T. Su, F. Huang, and M. J. Lancaster. "Wide-band superconducting coplanar delay lines". In: *IEEE Trans Microw Theory Tech* 53.7 (2005), pp. 2348–2354.

[115] M. Sumetsky and B. J. Eggleton. "Modeling and optimization of complex photonic resonant cavity circuits". In: *Opt. Express* 11.4 (2003), pp. 381–391.

[116] S. B. Cohn. "Direct-coupled-resonator filters". In: *Proceedings of the IRE* 45.2 (1957), pp. 187–196.

[117] In: *Sonnet, Sonnet Suites, Version 16.52* ().

[118] J. Gao. "The physics of superconducting microwave resonators". PhD thesis. California Institute of Technology, 2008.

[119] D. L. Underwood, W. E. Shanks, J. Koch, and A. A. Houck. "Low-disorder microwave cavity lattices for quantum simulation with photons". In: *Phys. Rev. A* 86.2 (2012), p. 023837.

[120] H. T. Dung and K. Ujihara. "Analytic solution for retardation in two-atom systems". In: *Phys. Rev. A* 59.3 (1999), p. 2524.

[121] B. T. Gard, K. Jacobs, R. McDermott, and M. Saffman. "Microwave-to-optical frequency conversion using a cesium atom coupled to a superconducting resonator". In: *Phys. Rev. A* 96.1 (2017), p. 013833.

[122] J. Han, T. Vogt, C. Gross, D. Jaksch, M. Kiffner, and W. Li. "Coherent microwave-to-optical conversion via six-wave mixing in Rydberg atoms". In: *Phys. Rev. Lett.* 120.9 (2018), p. 093201.

[123] T. Vogt, C. Gross, J. Han, S. B. Pal, M. Lam, M. Kiffner, and W. Li. "Efficient microwave-to-optical conversion using Rydberg atoms". In: *Phys. Rev. A* 99.2 (2019), p. 023832.

[124] L. A. Williamson, Y.-H. Chen, and J. J. Longdell. "Magneto-optic modulator with unit quantum efficiency". In: *Phys. Rev. Lett.* 113.20 (2014), p. 203601.

[125] X. Fernandez-Gonzalvo, Y.-H. Chen, C. Yin, S. Rogge, and J. J. Longdell. "Coherent frequency up-conversion of microwaves to the optical telecommunications band in an Er: YSO crystal". In: *Phys. Rev. A* 92.6 (2015), p. 062313.

[126] X. Fernandez-Gonzalvo, S. P. Horvath, Y.-H. Chen, and J. J. Longdell. "Cavity-enhanced Raman heterodyne spectroscopy in Er^{3+}: Y_2SiO_5 for microwave to optical signal conversion". In: *Phys. Rev. A* 100.3 (2019), p. 033807.

[127] J. G. Bartholomew, J. Rochman, T. Xie, J. M. Kindem, A. Ruskuc, I. Craiciu, M. Lei, and A. Faraon. "On-chip coherent microwave-to-optical transduction mediated by ytterbium in YVO_4". In: *Nat. Commun.* 11.1 (2020), pp. 1–6.

[128] C. Javerzac-Galy, K. Plekhanov, N. R. Bernier, L. D. Toth, A. K. Feofanov, and T. J. Kippenberg. "On-chip microwave-to-optical quantum coherent converter based on a superconducting resonator coupled to an electro-optic microresonator". In: *Phys. Rev. A* 94.5 (2016), p. 053815.

[129] M. Soltani, M. Zhang, C. Ryan, G. J. Ribeill, C. Wang, and M. Loncar. "Efficient quantum microwave-to-optical conversion using electro-optic nanophotonic coupled resonators". In: *Phys. Rev. A* 96.4 (2017), p. 043808.

[130] A. Rueda, W. Hease, S. Barzanjeh, and J. M. Fink. “Electro-optic entanglement source for microwave to telecom quantum state transfer”. In: *npj Quantum Inf.* 5.1 (2019), pp. 1–11.

[131] A. Rueda, F. Sedlmeir, M. C. Collodo, U. Vogl, B. Stiller, G. Schunk, D. V. Strekalov, C. Marquardt, J. M. Fink, O. Painter, et al. “Efficient microwave to optical photon conversion: an electro-optical realization”. In: *Optica* 3.6 (2016), pp. 597–604.

[132] L. Fan, C.-L. Zou, R. Cheng, X. Guo, X. Han, Z. Gong, S. Wang, and H. X. Tang. “Superconducting cavity electro-optics: a platform for coherent photon conversion between superconducting and photonic circuits”. In: *Sci. Adv.* 4.8 (2018), eaar4994.

[133] W. Fu, M. Xu, X. Liu, C.-L. Zou, C. Zhong, X. Han, M. Shen, Y. Xu, R. Cheng, S. Wang, et al. “Cavity electro-optic circuit for microwave-to-optical conversion in the quantum ground state”. In: *Phys. Rev. A* 103.5 (2021), p. 053504.

[134] J. Holzgrafe, N. Sinclair, D. Zhu, A. Shams-Ansari, M. Colangelo, Y. Hu, M. Zhang, K. K. Berggren, and M. Lončar. “Cavity electro-optics in thin-film lithium niobate for efficient microwave-to-optical transduction”. In: *Optica* 7.12 (2020), pp. 1714–1720.

[135] T. P. McKenna, J. D. Witmer, R. N. Patel, W. Jiang, R. Van Laer, P. Arrangoiz-Arriola, E. A. Wollack, J. F. Herrmann, and A. H. Safavi-Naeini. “Cryogenic microwave-to-optical conversion using a triply resonant lithium-niobate-on-sapphire transducer”. In: *Optica* 7.12 (2020), pp. 1737–1745.

[136] A. H. Safavi-Naeini and O. Painter. “Proposal for an optomechanical traveling wave phonon–photon translator”. In: *New J. Phys.* 13.1 (2011), p. 013017.

[137] K. Stannigel, P. Rabl, A. S. Sørensen, P. Zoller, and M. D. Lukin. “Optomechanical transducers for long-distance quantum communication”. In: *Phys. Rev. Lett.* 105.22 (2010), p. 220501.

[138] S. Barzanjeh, M. Abdi, G. J. Milburn, P. Tombesi, and D. Vitali. “Reversible optical-to-microwave quantum interface”. In: *Phys. Rev. Lett.* 109.13 (2012), p. 130503.

[139] T. Bagci, A. Simonsen, S. Schmid, L. G. Villanueva, E. Zeuthen, J. Appel, J. M. Taylor, A. Sørensen, K. Usami, A. Schliesser, et al. “Optical detection of radio waves through a nanomechanical transducer”. In: *Nature* 507.7490 (2014), pp. 81–85.

[140] R. W. Andrews, R. W. Peterson, T. P. Purdy, K. Cicak, R. W. Simmonds, C. A. Regal, and K. W. Lehnert. “Bidirectional and efficient conversion between microwave and optical light”. In: *Nat. Phys.* 10.4 (2014), pp. 321–326.

[141] A. P. Higginbotham, P. S. Burns, M. D. Urmey, R. W. Peterson, N. S. Kampel, B. M. Brubaker, G. Smith, K. W. Lehnert, and C. A. Regal. "Harnessing electro-optic correlations in an efficient mechanical converter". In: *Nat. Phys.* 14.10 (2018), pp. 1038–1042.

[142] J. Bochmann, A. Vainsencher, D. D. Awschalom, and A. N. Cleland. "Nanomechanical coupling between microwave and optical photons". In: *Nat. Phys.* 9.11 (2013), pp. 712–716.

[143] K. C. Balram, M. I. Davanço, J. D. Song, and K. Srinivasan. "Coherent coupling between radiofrequency, optical and acoustic waves in piezo-optomechanical circuits". In: *Nat. Photonics* 10.5 (2016), pp. 346–352.

[144] M. Forsch, R. Stockill, A. Wallucks, I. Marinković, C. Gärtner, R. A. Norte, F. van Otten, A. Fiore, K. Srinivasan, and S. Gröblacher. "Microwave-to-optics conversion using a mechanical oscillator in its quantum ground state". In: *Nat. Phys.* 16.1 (2020), pp. 69–74.

[145] W. Jiang, C. J. Sarabalis, Y. D. Dahmani, R. N. Patel, F. M. Mayor, T. P. McKenna, R. Van Laer, and A. H. Safavi-Naeini. "Efficient bidirectional piezo-optomechanical transduction between microwave and optical frequency". In: *Nat. Commun.* 11.1 (2020), pp. 1–7.

[146] W. Jiang, R. N. Patel, F. M. Mayor, T. P. McKenna, P. Arrangoiz-Arriola, C. J. Sarabalis, J. D. Witmer, R. Van Laer, and A. H. Safavi-Naeini. "Lithium niobate piezo-optomechanical crystals". In: *Optica* 6.7 (2019), pp. 845–853.

[147] A. Vainsencher, K. J. Satzinger, G. A. Peairs, and A. N. Cleland. "Bi-directional conversion between microwave and optical frequencies in a piezoelectric optomechanical device". In: *Appl. Phys. Lett.* 109.3 (2016), p. 033107.

[148] L. Shao, M. Yu, S. Maity, N. Sinclair, L. Zheng, C. Chia, A. Shams-Ansari, C. Wang, M. Zhang, K. Lai, et al. "Microwave-to-optical conversion using lithium niobate thin-film acoustic resonators". In: *Optica* 6.12 (2019), pp. 1498–1505.

[149] X. Han, W. Fu, C. Zhong, C.-L. Zou, Y. Xu, A. Al Sayem, M. Xu, S. Wang, R. Cheng, L. Jiang, et al. "Cavity piezo-mechanics for superconducting-nanophotonic quantum interface". In: *Nat. Commun.* 11.1 (2020), pp. 1–8.

[150] M. Aspelmeyer, T. J. Kippenberg, and F. Marquardt. "Cavity optomechanics". In: *Rev. Mod. Phys.* 86.4 (2014), p. 1391.

[151] T. J. Kippenberg and K. J. Vahala. "Cavity opto-mechanics". In: *Opt. Express* 15.25 (2007), pp. 17172–17205.

[152] J. Chan, A. H. Safavi-Naeini, J. T. Hill, S. Meenehan, and O. Painter. "Optimized optomechanical crystal cavity with acoustic radiation shield". In: *Appl. Phys. Lett.* 101.8 (2012), p. 081115.

[153] A. H. Safavi-Naeini and O. Painter. “Optomechanical crystal devices”. In: *Cavity Optomechanics*. Springer, 2014, pp. 195–231.

[154] S. M. Meenehan, J. D. Cohen, S. Gröblacher, J. T. Hill, A. H. Safavi-Naeini, M. Aspelmeyer, and O. Painter. “Silicon optomechanical crystal resonator at millikelvin temperatures”. In: *Phys. Rev. A* 90.1 (2014), p. 011803.

[155] J. D. Cohen, S. M. Meenehan, G. S. MacCabe, S. Gröblacher, A. H. Safavi-Naeini, F. Marsili, M. D. Shaw, and O. Painter. “Phonon counting and intensity interferometry of a nanomechanical resonator”. In: *Nature* 520.7548 (2015), pp. 522–525.

[156] S. M. Meenehan, J. D. Cohen, G. S. MacCabe, F. Marsili, M. D. Shaw, and O. Painter. “Pulsed excitation dynamics of an optomechanical crystal resonator near its quantum ground state of motion”. In: *Phys. Rev. X* 5.4 (2015), p. 041002.

[157] K. W. Murch, K. L. Moore, S. Gupta, and D. M. Stamper-Kurn. “Observation of quantum-measurement backaction with an ultracold atomic gas”. In: *Nat. Phys.* 4.7 (2008), pp. 561–564.

[158] F. Brennecke, S. Ritter, T. Donner, and T. Esslinger. “Cavity optomechanics with a Bose-Einstein condensate”. In: *Science* 322.5899 (2008), pp. 235–238.

[159] O. Arcizet, P.-F. Cohadon, T. Briant, M. Pinard, and A. Heidmann. “Radiation-pressure cooling and optomechanical instability of a micromirror”. In: *Nature* 444.7115 (2006), pp. 71–74.

[160] I. Favero, C. Metzger, S. Camerer, D. König, H. Lorenz, J. P. Kotthaus, and K. Karrai. “Optical cooling of a micromirror of wavelength size”. In: *Appl. Phys. Lett.* 90.10 (2007), p. 104101.

[161] S. Gigan, H. R. Böhm, M. Paternostro, F. Blaser, G. Langer, J. B. Hertzberg, K. C. Schwab, D. Bäuerle, M. Aspelmeyer, and A. Zeilinger. “Self-cooling of a micromirror by radiation pressure”. In: *Nature* 444.7115 (2006), pp. 67–70.

[162] G. S. MacCabe, H. Ren, J. Luo, J. D. Cohen, H. Zhou, A. Sipahigil, M. Mirhosseini, and O. Painter. “Nano-acoustic resonator with ultralong phonon lifetime”. In: *Science* 370.6518 (2020), pp. 840–843.

[163] J.-i. Kushibiki, I. Takanaga, M. Arakawa, and T. Sannomiya. “Accurate measurements of the acoustical physical constants of $LiNbO_3$ and $LiTaO_3$ single crystals”. In: *IEEE Trans. Ultrason. Ferroelectr. Freq. Control* 46.5 (1999), pp. 1315–1323.

[164] D. K. Biegelsen. “Frequency dependence of the photoelastic coefficients of silicon”. In: *Phys. Rev. B* 12.6 (1975), p. 2427.

[165] B. J. Frey, D. B. Leviton, and T. J. Madison. "Temperature-dependent refractive index of silicon and germanium". In: *Optomechanical Technologies for Astronomy*. Vol. 6273. International Society for Optics and Photonics. 2006, 62732J.

[166] A. Nersisyan, S. Poletto, N. Alidoust, R. Manenti, R. Renzas, C.-V. Bui, K. Vu, T. Whyland, Y. Mohan, E. A. Sete, et al. "Manufacturing low dissipation superconducting quantum processors". In: *2019 IEEE International Electron Devices Meeting (IEDM)*. IEEE. 2019, pp. 31–1.

[167] J. M. Gambetta, C. E. Murray, Y.-K.-K. Fung, D. T. McClure, O. Dial, W. Shanks, J. W. Sleight, and M. Steffen. "Investigating surface loss effects in superconducting transmon qubits". In: *IEEE Trans. Appl. Supercond.* 27.1 (2016), pp. 1–5.

[168] N. Samkharadze, A. Bruno, P. Scarlino, G. Zheng, D. P. DiVincenzo, L. DiCarlo, and L. M. K. Vandersypen. "High-kinetic-inductance superconducting nanowire resonators for circuit QED in a magnetic field". In: *Phys. Rev. Appl.* 5.4 (2016), p. 044004.

[169] M. Lee. "Dielectric constant and loss tangent in LiNbO 3 crystals from 90 to 147 GHz". In: *Appl. Phys. Lett.* 79.9 (2001), pp. 1342–1344.

[170] J. A. Nelder and R. Mead. "A simplex method for function minimization". In: *Comput. J.* 7.4 (1965), pp. 308–313.

[171] J. C. Lagarias, J. A. Reeds, M. H. Wright, and P. E. Wright. "Convergence properties of the Nelder–Mead simplex method in low dimensions". In: *SIAM J. Optim.* 9.1 (1998), pp. 112–147.

[172] D. K. Biegelsen. "Photoelastic tensor of silicon and the volume dependence of the average gap". In: *Phys. Rev. Lett.* 32.21 (1974), p. 1196.

[173] S. G. Johnson, M. Ibanescu, M. A. Skorobogatiy, O. Weisberg, J. Joannopoulos, and Y. Fink. "Perturbation theory for Maxwell's equations with shifting material boundaries". In: *Phys. Rev. E* 65.6 (2002), p. 066611.

[174] J. Chan. "Laser cooling of an optomechanical crystal resonator to its quantum ground state of motion". PhD thesis. California Institute of Technology, 2012.

[175] E. A. Wollack, A. Y. Cleland, P. Arrangoiz-Arriola, T. P. McKenna, R. G. Gruenke, R. N. Patel, W. Jiang, C. J. Sarabalis, and A. H. Safavi-Naeini. "Loss channels affecting lithium niobate phononic crystal resonators at cryogenic temperature". In: *Appl. Phys. Lett.* 118.12 (2021), p. 123501.

[176] A. Stesmans. "Passivation of P_{b0} and P_{b1} interface defects in thermal (100) Si/SiO_2 with molecular hydrogen". In: *Appl. Phys. Lett.* 68.15 (1996), pp. 2076–2078.

[177] M. Borselli, T. J. Johnson, and O. Painter. "Measuring the role of surface chemistry in silicon microphotonics". In: *Appl. Phys. Lett.* 88.13 (2006), p. 131114.

[178] H. Ren, M. H. Matheny, G. S. MacCabe, J. Luo, H. Pfeifer, M. Mirhosseini, and O. Painter. "Two-dimensional optomechanical crystal cavity with high quantum cooperativity". In: *Nat. Commun.* 11.1 (2020), pp. 1–10.

[179] J. M. Martinis, M. Ansmann, and J. Aumentado. "Energy decay in superconducting Josephson-junction qubits from nonequilibrium quasiparticle excitations". In: *Phys. Rev. Lett.* 103.9 (2009), p. 097002.

[180] S. B. Kaplan, C. C. Chi, D. N. Langenberg, J.-J. Chang, S. Jafarey, and D. J. Scalapino. "Quasiparticle and phonon lifetimes in superconductors". In: *Phys. Rev. B* 14.11 (1976), p. 4854.

[181] C. Wang, Y. Y. Gao, I. M. Pop, U. Vool, C. Axline, T. Brecht, R. W. Heeres, L. Frunzio, M. H. Devoret, G. Catelani, et al. "Measurement and control of quasiparticle dynamics in a superconducting qubit". In: *Nat. Commun.* 5.1 (2014), pp. 1–7.

[182] R. Barends, J. J. A. Baselmans, S. J. C. Yates, J. R. Gao, J. N. Hovenier, and T. M. Klapwijk. "Quasiparticle relaxation in optically excited high-Q superconducting resonators". In: *Phys. Rev. Lett.* 100.25 (2008), p. 257002.

[183] R. B. Laibowitz and A. F. Mayadas. "Josephson junctions with Nb/Al composite electrodes". In: *Appl. Phys. Lett.* 20.7 (1972), pp. 254–256.

[184] E. Klokholm and B. S. Berry. "Intrinsic stress in evaporated metal films". In: *J. Electrochem. Soc.* 115.8 (1968), p. 823.

[185] M. Murakami and T. Yogi. "Strain in evaporated Nb thin films". In: *J. Appl. Phys.* 57.2 (1985), pp. 211–215.

[186] C. T. Wu. "Intrinsic stress of magnetron-sputtered niobium films". In: *Thin Solid Films* 64.1 (1979), pp. 103–110.

[187] G. G. Stoney. "The tension of metallic films deposited by electrolysis". In: *Proc. R. Soc. Lond. A* 82.553 (1909), pp. 172–175.

[188] M. Zecchino and T. Cunningham. "Thin film stress measurement using dektak stylus profilers". In: *Veeco Instruments Inc* (2004).

[189] J. C. Owens. "Creating quantum topological materials with 3D microwave photons". PhD thesis. The University of Chicago, 2019.

[190] M. V. Göppl. "Engineering quantum electronic chips: realization and characterization of circuit quantum electrodynamics systems". PhD thesis. ETH Zurich, 2009.

[191] B. G. Christensen, C. D. Wilen, A. Opremcak, J. Nelson, F. Schlenker, C. H. Zimonick, L. Faoro, L. B. Ioffe, Y. J. Rosen, J. L. DuBois, et al. “Anomalous charge noise in superconducting qubits”. In: *Phys. Rev. B* 100.14 (2019), p. 140503.

[192] M. D. Henry. “ICP etching of silicon for micro and nanoscale devices”. PhD thesis. California Institute of Technology, 2010.

[193] M. F. Volk, S. Suntsov, C. E. Rüter, and D. Kip. “Low loss ridge waveguides in lithium niobate thin films by optical grade diamond blade dicing”. In: *Opt. Express* 24.2 (2016), pp. 1386–1391.

[194] N. Courjal, B. Guichardaz, G. Ulliac, J.-Y. Rauch, B. Sadani, H.-H. Lu, and M.-P. Bernal. “High aspect ratio lithium niobate ridge waveguides fabricated by optical grade dicing”. In: *J. Phys. D: Appl. Phys.* 44.30 (2011), p. 305101.

[195] R. Wu, J. Lin, M. Wang, Z. Fang, W. Chu, J. Zhang, J. Zhou, and Y. Cheng. “Fabrication of a multifunctional photonic integrated chip on lithium niobate on insulator using femtosecond laser-assisted chemomechanical polish”. In: *Opt. Lett.* 44.19 (2019), pp. 4698–4701.

[196] M. Wang, R. Wu, J. Lin, J. Zhang, Z. Fang, Z. Chai, and Y. Cheng. “Chemo-mechanical polish lithography: A pathway to low loss large-scale photonic integration on lithium niobate on insulator”. In: *Quantum Eng.* 1.1 (2019), e9.

[197] J.-x. Zhou, R.-h. Gao, J. Lin, M. Wang, W. Chu, W.-b. Li, D.-f. Yin, L. Deng, Z.-w. Fang, J.-h. Zhang, et al. “Electro-optically switchable optical true delay lines of meter-scale lengths fabricated on lithium niobate on insulator using photolithography assisted chemo-mechanical etching”. In: *Chin. Phys. Lett* 37.8 (2020), p. 084201.

[198] K. Nassau, H. J. Levinstein, and G. M. Loiacono. “The domain structure and etching of ferroelectric lithium niobate”. In: *Appl. Phys. Lett.* 6.11 (1965), pp. 228–229.

[199] F. Laurell, J. Webjorn, G. Arvidsson, and J. Holmberg. “Wet etching of proton-exchanged lithium niobate-a novel processing technique”. In: *J. Lightwave Technol.* 10.11 (1992), pp. 1606–1609.

[200] H. Hu, R. Ricken, W. Sohler, and R. Wehrspohn. “Lithium niobate ridge waveguides fabricated by wet etching”. In: *IEEE Photonics Technol. Lett.* 19.6 (2007), pp. 417–419.

[201] Y. Li, T. Lan, D. Yang, M. Xiang, J. Dai, C. Li, and Z. Wang. “Research of selective etching in LiNbO3 using proton-exchanged wet etching technique”. In: *Mater. Res. Express* 7.5 (2020), p. 056202.

[202] A. B. Randles, M. Esashi, and S. Tanaka. “Etch rate dependence on crystal orientation of lithium niobate”. In: *IEEE Trans. Ultrason. Ferroelectr. Freq. Control* 57.11 (2010), pp. 2372–2380.

[203] C. L. Sones, S. Mailis, W. S. Brocklesby, R. W. Eason, and J. R. Owen. “Differential etch rates in z-cut LiNbO 3 for variable HF/HNO 3 concentrations”. In: *J. Mater. Chem.* 12.2 (2002), pp. 295–298.

[204] R. Geiss, J. Brandt, H. Hartung, A. Tünnermann, T. Pertsch, E.-B. Kley, and F. Schrempel. “Photonic microstructures in lithium niobate by potassium hydroxide-assisted ion beam-enhanced etching”. In: *J. Vac. Sci. Technol. B* 33.1 (2015), p. 010601.

[205] H. Hu, A. P. Milenin, R. B. Wehrspohn, H. Hermann, and W. Sohler. “Plasma etching of proton-exchanged lithium niobate”. In: *J. Vac. Sci. Technol. A* 24.4 (2006), pp. 1012–1015.

[206] H. Nagata, N. Mitsugi, K. Shima, M. Tamai, and E. M. Haga. “Growth of crystalline LiF on CF4 plasma etched LiNbO3 substrates”. In: *J. Cryst. Growth* 187.3-4 (1998), pp. 573–576.

[207] Z. Ren, P. J. Heard, J. M. Marshall, P. A. Thomas, and S. Yu. “Etching characteristics of LiNbO 3 in reactive ion etching and inductively coupled plasma”. In: *J. Appl. Phys.* 103.3 (2008), p. 034109.

[208] D. Jun, J. Wei, C. Eng Png, S. Guangyuan, J. Son, H. Yang, and A. J. Danner. “Deep anisotropic LiNbO3 etching with SF6/Ar inductively coupled plasmas”. In: *J. Vac. Sci. Technol. B* 30.1 (2012), p. 011208.

[209] W.-S. Tan, G. W. Fang, G. Pillai, C.-C. Chen, C.-Y. Chen, C.-H. Chin, and S.-S. Li. “Fabrication and characterization of lithium-niobate thin film MEMS piezoelectric resonators”. In: *2016 IEEE 11th Annual International Conference on Nano/Micro Engineered and Molecular Systems (NEMS)*. IEEE. 2016, pp. 516–519.

[210] G. Si, A. J. Danner, S. L. Teo, E. J. Teo, J. Teng, and A. A. Bettiol. “Photonic crystal structures with ultrahigh aspect ratio in lithium niobate fabricated by focused ion beam milling”. In: *J. Vac. Sci. Technol. B* 29.2 (2011), p. 021205.

[211] F. Lacour, N. Courjal, M.-P. Bernal, A. Sabac, C. Bainier, and M. Spajer. “Nanostructuring lithium niobate substrates by focused ion beam milling”. In: *Opt. Mater.* 27.8 (2005), pp. 1421–1425.

[212] P. Arrangoiz-Arriola, E. A. Wollack, M. Pechal, J. D. Witmer, J. T. Hill, and A. H. Safavi-Naeini. “Coupling a superconducting quantum circuit to a phononic crystal defect cavity”. In: *Phys. Rev. X* 8.3 (2018), p. 031007.

[213] C. Wang, M. Zhang, B. Stern, M. Lipson, and M. Lončar. “Nanophotonic lithium niobate electro-optic modulators”. In: *Opt. Express* 26.2 (2018), pp. 1547–1555.

[214] M. Zhang, C. Wang, R. Cheng, A. Shams-Ansari, and M. Lončar. “Monolithic ultra-high-Q lithium niobate microring resonator”. In: *Optica* 4.12 (2017), pp. 1536–1537.

[215] G. Ulliac, V. Calero, A. Ndao, F. I. Baida, and M.-P. Bernal. "Argon plasma inductively coupled plasma reactive ion etching study for smooth sidewall thin film lithium niobate waveguide application". In: *Opt. Mater.* 53 (2016), pp. 1–5.

[216] H. Robbins and B. Schwartz. "Chemical Etching of Silicon". In: *J. Electrochem. Soc.* 106.6 (1959), p. 505.

[217] C. Iliescu, F. E. H. Tay, and J. Miao. "Strategies in deep wet etching of Pyrex glass". In: *Sens. Actuators, A* 133.2 (2007), pp. 395–400.